

Aalborg Universitet



Small-Signal Stability Analysis and Control of Grid-forming Type IV Wind Turbines

Liu, Shiyi

DOI (link to publication from Publisher):
[10.54337/aau749586194](https://doi.org/10.54337/aau749586194)

Publication date:
2024

Document Version
Publisher's PDF, also known as Version of record

[Link to publication from Aalborg University](#)

Citation for published version (APA):

Liu, S. (2024). *Small-Signal Stability Analysis and Control of Grid-forming Type IV Wind Turbines*. Aalborg University Open Publishing. <https://doi.org/10.54337/aau749586194>

General rights

Copyright and moral rights for the publications made accessible in the public portal are retained by the authors and/or other copyright owners and it is a condition of accessing publications that users recognise and abide by the legal requirements associated with these rights.

- Users may download and print one copy of any publication from the public portal for the purpose of private study or research.
- You may not further distribute the material or use it for any profit-making activity or commercial gain
- You may freely distribute the URL identifying the publication in the public portal -

Take down policy

If you believe that this document breaches copyright please contact us at vbn@aub.aau.dk providing details, and we will remove access to the work immediately and investigate your claim.

**SMALL-SIGNAL STABILITY ANALYSIS
AND CONTROL OF GRID-FORMING TYPE
IV WIND TURBINES**

**BY
SHIYI LIU**

PhD Thesis 2024



AALBORG UNIVERSITY
DENMARK

Small-Signal Stability Analysis and Control of Grid-forming Type IV Wind Turbines

Ph.D. Dissertation
Shiyi Liu

Submitted: June 2024

Main Supervisor: Professor Xiongfei Wang
Aalborg University
KTH Royal Institute of Technology

Co-supervisors: Assistant Professor Heng Wu
Aalborg University
Dr. Jos van der Burgt
DNV

Assessment: Associate Professor Yajuan Guan (Chair)
Aalborg University, Denmark
Professor Oriol Gomis-Bellmunt
Technical University of Catalonia, Spain
Professor Fei Gao
University of Technology of Bel-fort-Montbeliard, France

PhD Series: Faculty of Engineering and Science, Aalborg University

Department: AAU Energy

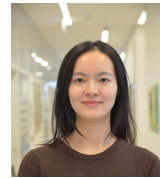
ISSN: 2446-1636
ISBN: 978-87-94563-81-9

Published by:
Aalborg University Open Publishing
Kroghstræde 1-3
DK – 9220 Aalborg Øst
aauopen@aau.dk

© Copyright: Shiyi Liu. Author has obtained the right to include the published and accepted articles in the thesis, with a condition that they are cited and/or copyright/credits are placed prominently in the references.

Curriculum Vitae

Shiyi Liu



Shiyi received her Master's Degree in Electrical Engineering and Bachelor's Degree in Electrical Engineering and Automation from North China Electric Power University, in the year 2018 and 2015 respectively. Since 2021, she has been an Early Stage Researcher within the Marie Skłodowska-Curie ITN project "WinGrid" at the DNV. She is also working toward the Ph.D. degree in electrical engineering under the supervision of Prof. Xiongfei Wang from Aalborg University, Aalborg, Denmark. She was a Guest Researcher in the L2EP laboratory at Ecole Centrale de Lille (France) from October 2022 to December 2022. Her research interests include modeling, control, and stability analysis of grid-forming wind turbines.

Curriculum Vitae

Abstract

Operating the Type-IV wind turbine (WT) with grid-forming (GFM) control, henceforth referred to as GFM-WT, emerges as an attractive solution for integrating large-scale wind energies into power systems. However, the application of GFM control may introduce different electromagnetic and electromechanical dynamics from those with traditional grid-following control, thereby imposing new challenges on the small-signal stability of wind turbine systems. To tackle this challenge, this PhD project develops comprehensive small-signal models for GFM-WTs various control structures, based on which, stability analysis is carried out to provide insights into the parametric impact on the electromagnetic and electromechanical dynamics of GFM-WT. Finally, recommendations for controller tuning are given to stabilize GFM-WTs.

The dc-link voltage control (DVC) of GFM-WTs can be implemented either in the Grid-Side Converter (GSC), referred to as GFM-GWT, or in the Machine-Side Converter (MSC), referred to as GFM-MWT. This PhD thesis starts with the investigation of the electromagnetic dynamics of GFM-MWT excluding the mechanical dynamics of the WT, which is referred to as GFM-MPMSG hereafter. By comparing the dc output impedance of the MSC and the dc-link capacitor, it is found that the dynamics of MSC have a negligible impact on the ac dynamics of GFM-MPMSG, and thus, can be ignored when analyzing the stability of GFM-MPMSG when connected to the ac grid.

Following the electromagnetic dynamics analysis, the PhD thesis delves into the analysis of electromechanical dynamics of GFM-MWT by incorporating the small-signal models of the mechanical parts of the WT. The reduced-order small-signal model of GFM-MWT is developed and analyzed to characterize the impact of GFM control on torsional dynamics during grid-phase change events. Based on the reduced-order model, the complex torque coefficients method is further adopted to analytically derive the simplified expressions of natural frequencies, damped frequencies, and damping ratios of torsional modes. It is revealed that a significant negative impact is introduced by the GFM-MWT on the torsional dynamics mode, thereby posing a higher risk of torsional vibrations.

The above analysis is further extended to GFM-GWT and GFM-MWT with

Abstract

varying DVC structures. It is demonstrated that the GFM-GWT configuration contributes to positive damping, whereas the GFM-MWT configuration exhibits a negative damping effect, depending on the specific DVC architecture implemented within the MSC. Additionally, a sensitivity analysis employing the partial derivative algorithm, based on the feedforward neural network, is performed to reveal the parametric impacts of electrical and mechanical system constants and controller gains, thereby offering insights for controller tuning to dampen the torsional vibrations.

Resumé

Integrationen af GFM-styring med Type IV-vindmøller, fremover benævnt som GFM-WT, fremstår som en banebrydende strategi i kraftsystemer domineret af effektelektronik. Dette skifte kræver en grundig undersøgelse af GFM-WTs elektriske og elektromekaniske virkemåder, for at forebygge mulige stabilitetsproblemer. For at adressere de potentielle problemer fokuserer denne ph.d.-afhandling på small-signal modeling, dynamic behavior analysis og evaluering af styringsstrategier for GFM-WTs.

I modsætning til traditionelle grid-following Type IV-vindmøller (GFL-WTs) har GFM-WTs tydelige placeringer for dc-link spændingskontrol (DVC) — enten i Grid-Side Converter (GFM-GWT) eller i Machine-Side Converter (GFM-MWT). Da konverterstyringen af GFM-MWT adskiller sig fra den generelle styring af GFL-WT, forudsætter et studie af GFM-MWTs en omfattende udforskning af vekselstrømsdynamikken på net-siden af dens small-signal stability analysis. For at adressere denne mangel, introducerer og evaluerer denne afhandling en ækvivalent udgangsimpedansmodel for både MSC og GFM-GSC. Det indikeres, at MSC's indflydelse på vekselstrøms impedansmodellen af GFM-MWTs er begrænset. Fundet understreger vigtigheden af GFM-GSC dynamikken i interaktionen mellem GFM-MWTs og elnettet.

Derudover dykker afhandlingen ned i de elektromekaniske dynamikker af GFM-MWTs, et kritisk aspekt af deres operationelle virkemåder, ved at tage højde for vindmøllens mekaniske dele. Først udvikles og analyseres den reduced-order small-signal model af GFM-MWTs for at demonstrere effekten af GFM-styring på torsional dynamics under ændringer i netfasen. Baseret på de reduced-order modeller udvides undersøgelsen til anvendelse af den complex torque coefficients method, som hjælper med at opnå forenklede udtryk for naturlige frekvenser, dæmpede frekvenser og dæmpningsforhold for torsional modes. Det konstateres, at GFM-MWT introducerer en betydelig negativ indvirkning på torsional mode'en.

Yderligere analyse undersøger de differentielle påvirkninger af GFM-MWT- og GFM-GWT-konfigurationer på torsional dynamics og fremhæver, at mens GFM-GWT introducerer positiv dæmpning, pålægger GFM-MWT en negativ dæmpningseffekt på grund af DVC inden for MSC. Derudover

Resumé

gennemføres en følsomhedsanalyse ved brug af den partial derivative algorithm, baseret på træningen af feedforward neural network, for at vurdere de parametriske påvirkninger af elektriske og mekaniske systemkonstanter og styringsgevinster. Resultaterne indikerer, at konverterstyringen har en begrænset indvirkning på den dæmpede frekvens i både GFM-GWT- og GFM-MWT-konfigurationer. Desuden undersøges tre bredt anvendte DVC-strategier inden for MSC for GFM-MWTs, hver karakteriseret ved distinkte implikationer på Systemets output. Analyse af torsional modes via den complex torque coefficients method giver analytisk indsigt i påvirkningerne af disse DVC-strategier på torsional dynamics, hvilket skaber forståelse for DVC's påvirkninger, hvilket kan anvendes til at forbedre stabiliteten af GFM-MWTs.

Acknowledgements

Firstly, I am deeply grateful to my supervisor, Prof. Xiongfei Wang, and my manager, Mr. Theo Bosma, for the opportunity to be a Marie Curie Early Stage Researcher. Their belief in my abilities and continuous support have been crucial to my progress. I especially thank Prof. Wang for his invaluable guidance and rigorous discussions that have greatly influenced my work. In addition, I am grateful for teaching me the ins and outs of doing research and how to always strive for perfection.

I also extend my thanks to my co-supervisor, Asst. Prof. Heng Wu, for his exceptional mentorship and patient guidance in writing and presenting scholarly work. His feedback has significantly sharpened my analytical skills.

Additionally, I am grateful to Prof. Xavier Guillaud for his insightful guidance during my study abroad.

I acknowledge the financial support from the WinGrid consortium and value the interactions with all its members. My colleagues at Aalborg University and DNV, along with my co-authors Dr. Liang Zhao, Dr. Artur Avazov, Dr. Razvan Gabriel Cirstea, Dr. Ganesh Sauba, Dr. Ravi Singh, and Dr. Jos van der Burgt, have provided a friendly work environment and constructive feedback.

Lastly, I thank my family, boyfriend, and friends for their endless positivity, patience, and support. I am fortunate to be surrounded by such supportive individuals.

Acknowledgements

Lists of Abbreviations, Figures and Tables

List of Abbreviations

WT Wind Turbine

SCIG Squirrel-cage Induction Generator

WRIG Wound-rotor Induction Generator

DFIG Doubly-fed Induction Generator

PMSG Permanent Magnet Synchronous Generator

B2B Back-to-Back

RoCoF Rate-of-Change of Frequency

GFM Grid-forming

GFL Grid-following

SCR Short Circuit Ratio

ENTSO-E European Network of Transmission System Operators for Electricity

GSC Grid-side Converter

GFM-WT Grid-forming Type-IV Wind Turbine

MSC Machine-side Converter

DVC dc-link Voltage Control

MPPT Maximum Power Point Tracking

List of Abbreviations

- GFM-GWT** GFM-WT where GSC controls the dc-link voltage
- GFM-MWT** GFM-WT where MSC controls the dc-link voltage
- GFL-WT** Grid-following Type-IV Wind Turbine
- GFM-GPMSG** GFM-GWT excluding mechanical dynamics
- GFM-MPMSG** GFM-MWT excluding mechanical dynamics
- SDOF** Single-Degree-of-Freedom
- PI** Proportional-Integral
- FNN** Feedforward Neural Networks
- PDA** Partial Derivative Algorithm
- PCC** Point of Common Coupling
- APC** Active Power Control
- Q-V** Reactive Power-voltage
- HPF** High-pass Filter
- RPC** Reactive Power Control
- GFM-GSC** Grid-forming control Grid-side Converter
- PRBS** Pseudo-random Binary Sequence
- ReLU** Rectified Linear Unit
- MAPE** Mean Absolute Percentage Error

List of Figures

1.1	Wind turbine installation capacities from 2020 to 2023 for Denmark, Germany, France, and the Netherlands	4
1.2	Technology evolution of wind turbine from Type I to Type IV from Vestas	5
1.3	The overall configuration for (a) GFM-GWT (b) GFM-MWT	6
1.4	Multi time-scales dynamics in the wind turbines.	7
1.5	Three different DVCs within the MSC for the GFM-MWT	8
1.6	Thesis structure and corresponding publications.	13
1.7	Experiment Setup for GFM-MPMSGs.	15
2.1	Structural depiction of the GFM-MWT	18
2.2	Structural depiction of the GFM-MPMSG	19
2.3	MSC control structure	19
2.4	GSC control structure	20
2.5	Controller dq frame and system dq frame.	22
2.6	Block diagram and small-signal model of the GFM-GSC with ac capacitors.	24
2.7	Block diagram and small-signal model of a GFM-GSC without ac capacitors.	25
2.8	Bode plot of the APC with different ac shunt capacitors, $L_e = 0.5$ p.u., SCR=1.5, without active damping.	26
2.9	Bode plots of the APC and equivalent APC with different capacitors, $L_e = 0.5$ p.u., SCR=1.5, without active damping.	27
2.10	Equivalent impedance model of open-loop MSC.	28
2.11	Small-signal representation of the closed-loop MSC.	28
2.12	Bode plot comparison of C_{dc} , Z_{dc} , and Z_{dcnew}	29
2.13	Equivalent ac impedance model of GFM-MPMSG.	30
2.14	Response of \hat{i}_{gq} to a 0.01 p.u. step disturbance in v_{gb} for GFM-GSC and GFM-MPMSG using parameters sets A and B, compared with the equivalent impedance model.	31
2.15	Experimental responses to a 0.1 p.u. step disturbance in v_{gd} : (a) GFM-GSC only. (b) GFM-MPMSG system with parameter set A*. (c) GFM-MPMSG system with parameter set B*.	32
2.16	Experimental responses to PRBS disturbance at the PCC: (a) GFM-GSC only. (b) GFM-MPMSG system with parameter set A*. (c) GFM-MPMSG system with parameter set B*.	32
3.1	Structural depiction of the GFM-MWT	36
3.2	The control structure of MSC within the GFM-MWT	36
3.3	The control structure of GSC within the GFM-MWT	37

List of Figures

3.4	Block diagram of the MSC inner control loop and generator model in the dq frame.	38
3.5	Reduced-order small-signal model of MSC.	39
3.6	Small-signal model of the GSC	40
3.7	Electromechanical small-signal model of the turbine	43
3.8	Electromechanical small-signal model of the GFM-WT system	43
3.9	W_s and W_d of the GFM-MWT and $-W_{MR}$	47
3.10	Damped frequency and damping ratio for the 2-mass drive train, turbine, and the GFM-MWT	47
3.11	Damped frequency and damping ratio of the GFM-MWT under varying SCR	48
3.12	Damped frequency and damping ratio of the GFM-MWT under varying C_{dc} when SCR=3	50
3.13	Damped frequency and damping ratio of the GFM-MWT under varying H when SCR=3	50
3.14	Damped frequency and damping ratio of the GFM-MWT under varying K_p when SCR=3	50
3.15	Comparison of simulation results and small-signal models for disturbance response of ω_r with 2° step disturbance adding to θ_g under steady state.	51
3.16	Disturbance response of ω_r for the GFM-MWT with 2° step disturbance adding to θ_g under varied control and system parameters. (a) Changing SCR. (b) Changing C_{dc} . (c) Changing control parameter H . (d) Changing control parameter K_p	51
4.1	The GFM-GWT configuration.	57
4.2	Control block diagram of MSC for the GFM-GWT.	58
4.3	Control block diagram of GSC for the GFM-GWT.	58
4.4	Small-signal models of (a) The GFM-GWT. (b) The GFM-MWT.	59
4.5	Comparison of simulation results and small-signal models for disturbance response of ω_r following a 2° step disturbance to θ_g under steady conditions. (a) GFM-GWT. (b) GFM-MWT.	61
4.6	Comparison of simulation results and small-signal models for disturbance response of ω_r following a 0.4 m/s step disturbance to v_w under steady conditions. (a) GFM-GWT. (b) GFM-MWT.	62
4.7	Feedforward Neural Network (FNN)	63
4.8	Sensitivity analysis of the inputs of the GFM-GWT on (a) damping ratio (b) damped frequency.	64
4.9	Sensitivity analysis of the inputs of the GFM-MWT on (a) damping ratio (b) damped frequency.	65
4.10	Three different MSC control structures for the GFM-MWT	66
4.11	Reduced-order small-signal model of (a) Type a MSC. (b) Type b MSC. (c) Type c MSC.	68

List of Figures

4.12	Feedback loop from $\hat{\omega}_r$ to \hat{T}_{gen} for the GFM-MWT under different DVCs. (a) Type <i>a</i> GFM-MWT. (b) Type <i>b</i> GFM-MWT. (c) Type <i>c</i> GFM-MWT.	69
4.13	Torsional coefficients $W_s(s)$ and $W_d(s)$ for Type <i>a</i> , <i>b</i> , and <i>c</i> GFM-MWT configurations.	70
4.14	Damped frequency and damping ratio for the 2-mass drive train, turbine, and type <i>a</i> , <i>b</i> , and <i>c</i> GFM-MWTs	70
4.15	Damped frequency and damping ratio of type <i>a</i> , <i>b</i> and <i>c</i> GFM-MWTs under varying SCR	71
4.16	Damped frequency and damping ratio of type <i>a</i> , <i>b</i> and <i>c</i> GFM-MWTs under varying C_{dc} when SCR=3	71
4.17	Damped frequency and damping ratio of type <i>a</i> , <i>b</i> and <i>c</i> GFM-MWTs under varying H when SCR=3	72
4.18	Damped frequency and damping ratio under varying K_p when SCR=3	72
4.19	Damped frequency and damping ratio of type <i>a</i> , <i>b</i> and <i>c</i> GFM-MWTs under varying operating point v_w when SCR=3	73
4.20	Comparison of nonlinear time-domain simulation results and small-signal models for disturbance response of ω_r with 2° step disturbance adding to θ_g under steady state. (a) Type <i>a</i> GFM-MWT. (b) Type <i>b</i> GFM-MWT. (c) Type <i>c</i> GFM-MWT.	74
4.21	Disturbance response of ω_r for the type <i>a</i> , <i>b</i> and <i>c</i> GFM-WT with 2° step disturbance adding to θ_g under varied control and system parameters. (a)-(c) Changing SCR. (d)-(f) Changing C_{dc} . (g)-(i) Changing control parameter H . (j)-(l) Changing control parameter K_p . (m)-(o) Changing operating wind speed v_w	75

List of Tables

1.1	Parameters used in the experiment	15
2.1	Parameters used in the simulation for the GFM-MPMSG	29
2.2	Control parameters used in the experiment for the GFM-MPMSG	32
3.1	Parameters of the GFM-MWT system [3]	49
4.1	Inputs and outputs of FNN	62

Contents

Curriculum Vitae	iii
Abstract	v
Resumé	vii
Acknowledgements	ix
Lists of Abbreviations, Figures and Tables	xi
List of Abbreviations	xi
List of Figures	xiii
List of Tables	xvi
Thesis Details	xxi
I Thesis Summary	1
1 Introduction	3
1.1 Background and Motivation	3
1.2 State of the Art and Challenges	5
1.2.1 Impedance-based electromagnetic dynamics analysis . .	6
1.2.2 Reduced-order model-based electromechanical dynam- ics analysis	8
1.3 Research Objectives and Limitations	10
1.3.1 Research Questions	10
1.3.2 Research Objectives	11
1.3.3 Project Limitations	11
1.4 Thesis Outline	12
1.5 List of Publications	13
1.6 Experimental Setup Utilized in This Thesis	14

2	Electromagnetic Dynamic Interactions between the GFM-MPMSG and AC Grid	17
2.1	Introduction	17
2.2	System Description	18
2.3	Impedance Modeling	22
2.3.1	Grid-side Converters	22
2.3.2	Machine-side Converters	27
2.3.3	GFM-MPMSG	30
2.4	Model validation	30
2.4.1	Simulation Results	30
2.4.2	Experimental Results	31
2.5	Summary	33
3	Modelling and analysis of torsional vibrations in GFM-MWTs	35
3.1	Background	35
3.2	System Description	36
3.3	Small-signal modeling of electromechanical dynamics of GFM-MWTs	38
3.3.1	Small-signal modeling of the MSC	38
3.3.2	Small-signal modeling of the GSC	40
3.3.3	Small-signal modeling of wind turbine mechanics	40
3.3.4	Small-signal modeling of GFM-MWT system	42
3.4	Torsional Modal Analysis	44
3.4.1	The 2-mass drive train	44
3.4.2	The wind turbine	44
3.4.3	Complex torque coefficients method-based torsional modal analysis of GFM-MWT	45
3.5	Eigenvalue and complex torque coefficients method-based torsional modal analysis	47
3.6	Simulation results	51
3.7	Summary	52
4	Impacts of different control strategies on electromechanical dynamics of GFM-WTs	55
4.1	Background	55
4.2	Comparative analysis of the GFM-GWT and GFM-MWT on torsional dynamics	56
4.2.1	Reduced-order small-signal model of the GFM-GWT	57
4.2.2	Torsional modal analysis of GFM-GWT	59
4.2.3	Validation through Nonlinear Time-Domain Simulations	60
4.3	Sensitivity analysis	61
4.3.1	Feedforward Neural Networks for torsional dynamics analysis	62

Contents

4.3.2	Partial derivative algorithm	64
4.4	The impact of dc-link voltage control on torsional vibrations within GFM-MWT	65
4.4.1	System description	65
4.4.2	Reduced-order small-signal modeling of the MSC under different DVCs	67
4.4.3	Torsional modal analysis of the GFM-MWTs with differ- ent DVCs	69
4.4.4	Analysis of influence factors	71
4.4.5	Validation through Nonlinear Time-Domain Simulations	72
4.5	Summary	74
5	Conclusion and future work	77
5.1	Conclusions	77
5.2	Future Work	78
	References	79

Contents

Thesis Details

Thesis Title:	Small-Signal Stability Analysis and Control of Grid-forming Type IV Wind Turbines
PhD Student:	Shiyi Liu Aalborg University DNV
PhD Supervisor:	Prof. Xiongfei Wang Aalborg University KTH Royal Institute of Technology
PhD Co-supervisor:	Asst. Prof. Heng Wu Aalborg University Dr. Jos van der Burgt DNV

The main body of the thesis consists of the following papers.

- [C1] **Shiyi Liu**, Heng Wu, Xiongfei Wang, Theo Bosma, Jos van der Burgt, Ganesh Sauba, Ravi Singh, "*Active damping of power control for grid-forming inverters in lc resonant grids*," in 2022 IEEE Energy Conversion Congress and Exposition (ECCE), pp. 1-6, 2022.
- [J1] **Shiyi Liu**, Heng Wu, Xiongfei Wang, Theo Bosma, Ganesh Sauba, "*Stability Analysis and Active Damping Design for Grid-Forming Converters in LC Resonant Grids*," in IEEE Open Journal of the Industrial Electronics Society, doi: 10.1109/OJIES.2024.3366290.
- [C2] **Shiyi Liu**, Heng Wu, Liang Zhao, Xiongfei Wang, Theo Bosma, Jos van der Burgt, Ganesh Sauba, "*Impact of Machine-Side Converter Dynamics on AC Impedance of Grid-Forming PMSG Wind Turbines*," in 2023 IEEE Applied Power Electronics Conference and Exposition (APEC), pp. 1339-1344, 2023.
- [C3] **Shiyi Liu**, Heng Wu, Xiongfei Wang, Artur Avazov, Xavier Guillaud, Theo Bosma, Ganesh Sauba, "*Torsional vibration analysis of grid-forming PMSG wind turbine*," in 22nd Wind and Solar Integration Workshop (WIW 2023), 2023.

- [J2] **Shiyi Liu**, Heng Wu, Xiongfei Wang, Theo Bosma, "*Impact of DC-Link Voltage Control on Torsional Vibrations in Grid-Forming PMSG Wind Turbines*," accepted by IEEE Trans. Energy Conversion, 2024.
- [J3] **Shiyi Liu**, Razvan Gabriel Cirstea, Heng Wu, Xiongfei Wang, Theo Bosma, "*Comparative Analysis of the Influence of Converters Control Strategies on Torsional Dynamics in Grid-Forming Wind Turbines*," under review in IEEE Trans. Sustainable Energy.

This thesis has been submitted for assessment in partial fulfillment of the Ph.D. degree. The thesis is based on the submitted or published scientific papers listed above. Parts of the content of the papers in the main body of the thesis are used directly or indirectly in the extended summary part of the thesis. As part of the assessment, co-author statements have been made available to the assessment committee and are also available at the Faculty. The permission for using the published and accepted articles in the thesis have been obtained from the corresponding publishers with the condition that they are cited and copyrights are placed prominently in the references. In reference to IEEE copyrighted material, which is used with permission in this thesis, the IEEE does not endorse any of Aalborg University's products or services. Internal or personal use of this material is permitted. If interested in reprinting/republishing IEEE copyrighted material for advertising or promotional purposes or for creating new collective works for resale or redistribution, please go to http://www.ieee.org/publications_standards/publications/rights/rights_link.html to learn how to obtain a License from RightsLink.

Part I

Thesis Summary

Chapter 1

Introduction

1.1 Background and Motivation

Europe is experiencing a significant transition towards renewable energy sources, particularly wind power, to mitigate climate change and reduce dependency on fossil fuels. This transition is evidenced by the growing capacities of wind installations in countries like Denmark, Germany, France, and the Netherlands, as illustrated in Fig. 1.1 [1]. The European Commission has set an ambitious target to achieve 450 GW of wind energy capacity by 2050, which would meet about 30% of Europe's forecasted electricity needs [2]. At present, the installed wind turbines (WTs) can be categorized into four main types based on their technological configuration [3]:

- Type I - Fixed-speed WTs: Utilizes a Squirrel-cage Induction Generator (SCIG), with rotor speed defined by the grid frequency.
- Type II - Adjustable-speed WTs: Employs a Wound-rotor Induction Generator (WRIG) that allows for approximately 10% speed variation through rotor resistance adjustments.
- Type III - Variable-speed WTs: Incorporates a Doubly-fed Induction Generator (DFIG), partially controlled by a Back-to-Back (B2B) converter.
- Type IV - Variable-speed WTs: Features a Permanent Magnet Synchronous Generator (PMSG), fully controlled by a B2B converter.

Recent industry reports, as depicted in Fig. 1.2 [4], indicate a noticeable shift towards the adoption of the more modern Type-III and Type-IV WTs, with Type-IV WTs becoming increasingly favored in new projects due to its enhanced efficiency, grid compatibility, and direct-drive functionality [5].

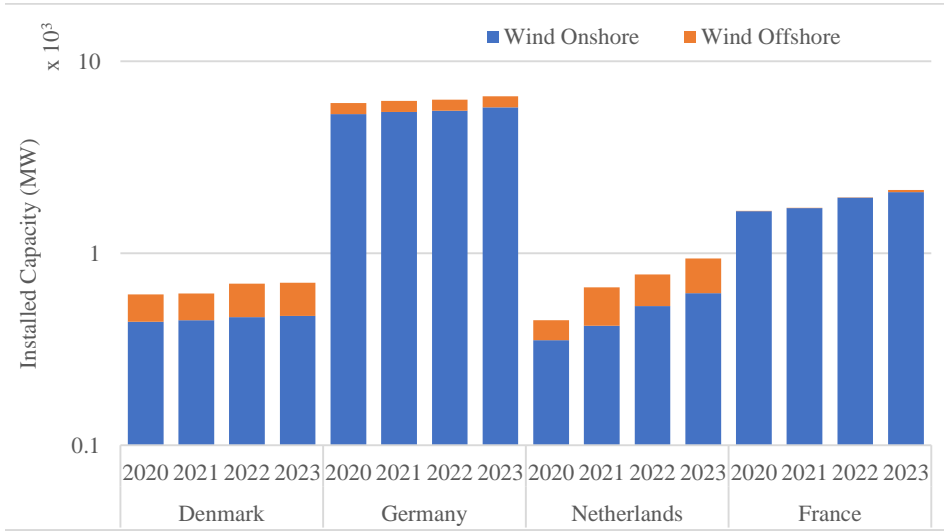


Figure 1.1: Wind turbine installation capacities from 2020 to 2023 for Denmark, Germany, France, and the Netherlands

With Type-IV WTs interfaced to the grid via power converters, the progressive integration of wind power technologies is leading to a transition from traditional synchronous generators to a power-electronic-dominated grid [6]. Despite the control flexibility and rapid response advantages that power converters provide, their widespread use introduces new challenges, such as reduced system inertia, higher Rate-of-Change of Frequency (RoCoF), diminished short-circuit capabilities, and complex interactions between converter controls and grid dynamics [3,7,8].

Addressing these issues, Grid-forming (GFM) converters have been recognized as an attractive solution for effectively integrating large-scale converter-based renewable energy sources into power systems [9]. Unlike traditional controlled converters, i.e., Grid-following (GFL) converters, GFM converters ensure grid stability under low Short Circuit Ratio (SCR) by acting as voltage sources [10,11] and providing extra inertia to the grid [12]. The European Network of Transmission System Operators for Electricity (ENTSO-E) emphasizes the significance of GFM control in its 2020-2030 roadmap, particularly for converters in transmission systems [13]. Consequently, the applications of GFM control in the Grid-side Converter (GSC) of the type-IV WTs, referred to as Grid-forming Type-IV Wind Turbine (GFM-WT) hereafter, have attracted considerable academic interest [4,14,15].

Existing studies have reported that the dc-link voltage of the GFM-WT can be regulated by either the GSC or the Machine-side Converter (MSC) [15]. For the case where GSC controls the dc-link voltage [16,17], abbreviated as

1.2. State of the Art and Challenges

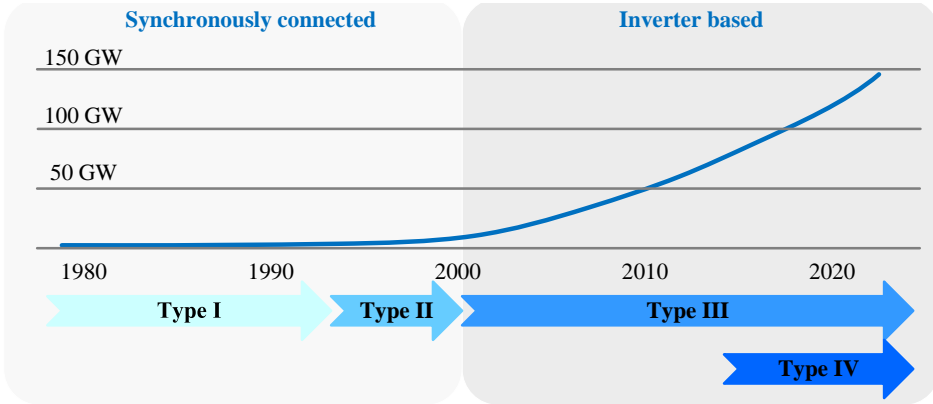


Figure 1.2: Technology evolution of wind turbine from Type I to Type IV from Vestas

GFM-GWT, as shown in Fig. 1.3 (a), the dc-link Voltage Control (DVC) is cascaded with the power-angle control, while the Maximum Power Point Tracking (MPPT) control is implemented with the MSC [18]. Due to the proven and mature MSC control, the control structure of the GFM-GWT emerges as an attractive solution [14]. The second approach, as introduced in [12, 19], abbreviated as GFM-MWT, as demonstrated in Fig. 1.3 (b), utilizes the MSC to control the dc-link voltage through the torque regulation, while the GFM control is implemented in the GSC. This structure is particularly advantageous for achieving the island operation or black start of the WT, as the dc-link voltage can be regulated independently by the MSC when the WT is disconnected from the grid [20].

Nevertheless, many existing works that analyze the dynamics of GFM-WTs solely focus on the dynamics of the GFM control itself [14], whereas the dynamics of the MSC, drive train, and turbine control are often oversimplified. Such simplifications, although reasonable for traditional GFL-controlled WT (GFL-WT) [21, 22], necessitate a more thorough for GFM-WTs. It has been found that the application of GFM-WTs poses several technical challenges, especially the potential torsional vibrations in GFM-MWTs caused by WT-grid interactions [23, 24]. This Ph.D. thesis aims to fill this gap by developing a complete analytical model of GFM-WT by incorporating both mechanical and MSC dynamics, based on which, its small-signal stability is thoroughly investigated.

1.2 State of the Art and Challenges

As documented in [25], electromagnetic and electromechanical dynamics are critical in analyzing the dynamic behavior of modern power systems. Figure

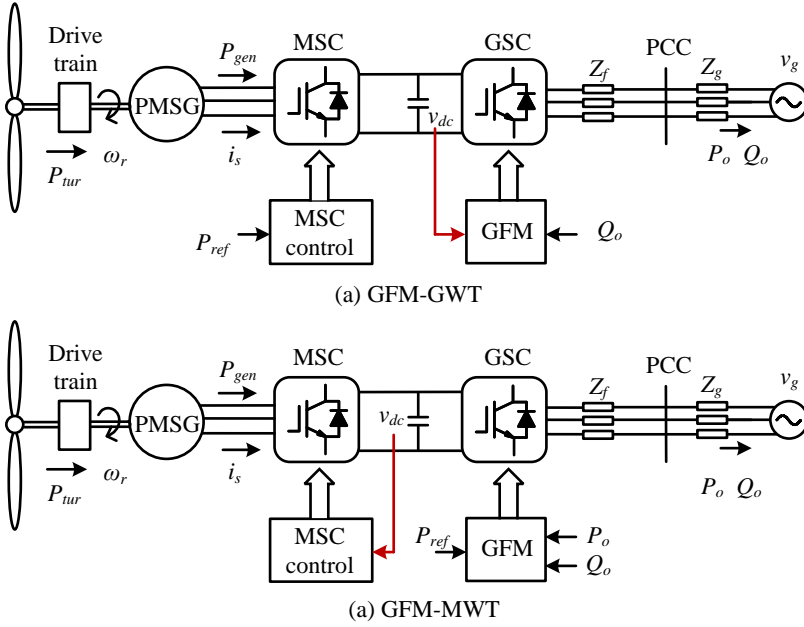


Figure 1.3: The overall configuration for (a) GFM-GWT (b) GFM-MWT

1.4 illustrates the time scales for electromagnetic and electromechanical dynamics in wind power systems [25, 26]. Electromagnetic dynamics primarily focus on the behavior of electromagnetic fields within the WT system, especially in components like the power converters. On the other hand, electromechanical dynamics focus on the interactions between mechanical components, i.e., the drive train, gearbox, and generator, and the electrical system, including the control mechanisms of power electronics.

Therefore, the analytical frameworks of this thesis for small-signal stability and control of GFM-WTs are divided into two main aspects: (a) impedance-based electromagnetic dynamics analysis, and (b) reduced-order model-based electromechanical dynamics analysis.

1.2.1 Impedance-based electromagnetic dynamics analysis

The integration of GFM-WTs into the power grid introduces complex challenges, including maintaining electromagnetic small-signal stability [27, 28]. To investigate the small-signal stability of WTs, the impedance-based analysis method has been developed and widely utilized [6, 29]. In impedance-based analysis, the WT is modeled as an equivalent ac impedance model, and stability is assessed using the impedance criterion [30]. As highlighted in [28]

1.2. State of the Art and Challenges

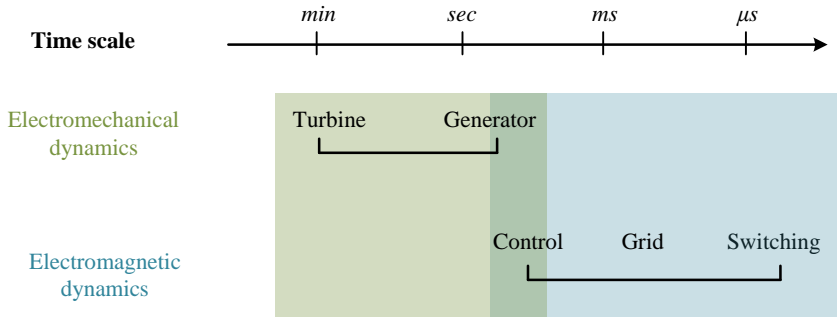


Figure 1.4: Multi time-scales dynamics in the wind turbines.

and [31], the impedance-based analysis method offers robust frameworks for stability analysis.

For traditional GFL-WTs, when the GSC controls the dc-link voltage, previous research [21, 27, 32] has shown that the dynamics of the MSC and generator may be overlooked when analyzing its interaction with the power grid due to the low bandwidth of the DVC [33]. Consequently, the dc-link capacitance is often modeled as an ideal dc voltage source during the impedance-based analysis.

When DVC is integrated within the MSC [34, 35], comparative research [36] indicates that MSC characteristics may affect dc-link dynamics and system impedance [34, 35], which reveals that oversimplifying the MSC as a constant dc voltage source might lead to inaccurate stability predictions [21, 27, 32].

However, studies like [34, 36] solely focus on the GFL-WT configuration. For GFM-WTs, it is essential to revisit the impact of the MSC and generator dynamics on grid interactions. In the case of GFM-GWTs, where the GSC controls the dc-link voltage, the dynamics of the MSC can also be overlooked due to the small DVC bandwidth of the MSC [16]. As for GFM-MWTs, where the DVC is placed in MSC, it is crucial to reassess how the electromagnetic dynamics of the MSC and generator might affect grid interaction dynamics in the small-signal stability analysis.

Given the focus on electromagnetic dynamics in GFM-MWTs, this analysis initially disregards mechanical dynamics due to their slower response rates by assuming a constant rotor speed. For clarity, throughout this discussion, GFM-MWTs, excluding mechanical dynamics, are referred to as GFM-MPMSGs.

Thus, the research gap in the impedance-based electromagnetic dynamics analysis of GFM-MPMSGs is summarized as follows:

- The impacts of the MSC and generator on the equivalent ac impedance model of GFM-MPMSGs dynamic remains unexplored. Hence, it is

not clear whether the dynamics of MSC and generator should be considered or can be ignored when analyzing the interactions between GFM-MPMSGs and the power grid.

1.2.2 Reduced-order model-based electromechanical dynamics analysis

GFM-WTs are recognized for facilitating island operation, enhancing grid stability under low SCR conditions, and contributing additional inertia to the grid [14]. Existing studies have reported that there are two typical configurations for GFM-WTs: GFM-GWT and GFM-MWT [15]. The mature MSC control of the GFM-GWT offers a robust solution [14, 16, 17], while the GFM-MWT configuration excels in island operations or black starts, allowing independent regulation of dc-link voltage by the MSC when disconnected from the grid [19, 20]. Moreover, there are three widely used strategies for implementing DVC within the MSC for GFM-MWTs. The first strategy involves the usage of the output of the Proportional-Integral (PI) controller within DVC as the reference for generator torque (T_{genref}), which then informs the inner loop control of the MSC. This approach is widely discussed due to its simplicity [37–39]. A second method, described in [40], utilizes the output of the PI controller as the reference for generator power, introducing generator rotor speed to calculate T_{genref} . This technique aids in aligning reference and actual generator power during small-signal analysis [41]. The third approach incorporates a feedforward term from the output power into the DVC for rapid dc-link voltage regulation [3].

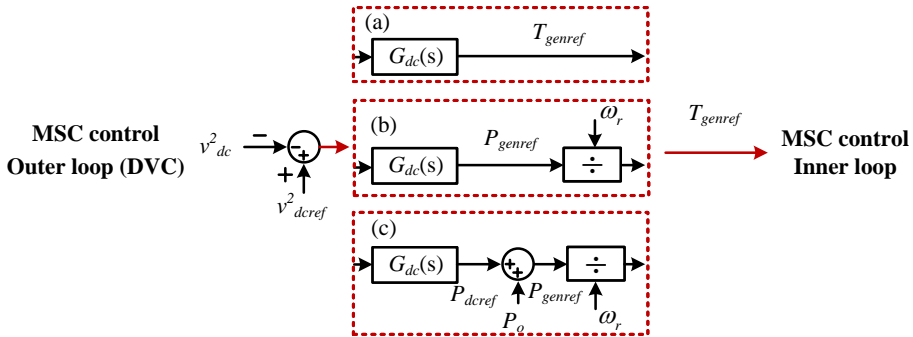


Figure 1.5: Three different DVCs within the MSC for the GFM-MWT

While many studies focus on analyzing the electromagnetic dynamics of GFM converter control, the mechanical dynamics of the turbine and drivetrain are often neglected [42–44]. However, the electromechanical dynamics of

GFM-WTs, particularly torsional vibrations caused by grid-side dynamics, while minimal in GFL-WTs, can significantly affect the lifespan of WTs and induce power oscillations that might compromise grid stability in GFM-WT applications, especially for GFM-MWTs [12, 23, 45].

Earlier investigations, primarily through time-domain simulations, highlighted that torsional vibrations in GFM-WTs arise from control adjustments that link grid dynamics directly to the electromagnetic torque of the generator [46]. While these initial findings provide a foundational understanding, they rely heavily on simulation results and focus predominantly on damping methods [3]. Subsequent research develops an electromechanical small-signal model to explore how GFM control parameters affect torsional dynamics in GFM-MWTs [39]. However, these studies remain largely numerical and omit the MSC dynamics, linearizing the MSC to a unity gain [39, 47]. Further work incorporates the MSC control structure into small-signal models, demonstrating numerically how adjustments in GFM control parameters could affect damping ratios of torsional modes [41, 45]. Yet, these studies still rely heavily on numerical simulations providing limited insights on the parametric impact and root causes of torsional vibrations of GFM-MWTs [48]. Thus, a more refined analytical approach is required to clarify the interplay between converter controls and electromechanical dynamics in GFM-WTs, particularly for torsional vibrations.

Moreover, past studies have predominantly focused on the GFM-MWT configuration, paying less attention to the potential impacts of converter controls, including the GFM-GWT configuration and GFM-MWTs with different DVCs, on electromechanical dynamics of WTs [12, 47], thus leaving the effects of control setups on torsional dynamics largely unexplored.

On the other hand, a detailed sensitivity analysis is crucial for comparing the effects of converter controls on the torsional dynamics of GFM-WTs [49]. Earlier research conducts sensitivity analyses against specific parameters like SCR and dc-link capacitors using small-signal models at fixed operation points [39, 45]. Later works expand this approach to include a wider range of system and GFM control parameters for GFM-MWTs [48, 50]. Nonetheless, these studies typically explored the independent impact of those parameters, without considering the interplay between parameter variations. As mentioned in [51], the Partial Derivative Algorithm (PDA) based on Feedforward Neural Networks (FNN) can be used for simultaneously assessing multiple system parameters and offering a comprehensive overview of their collective impacts. Therefore, the FNN-based PDA can be introduced as a promising methodology for analyzing the influences of varying system parameters on torsional modes of GFM-WTs under different converter controls [52].

Furthermore, the research gaps in the reduced-order model-based electromechanical dynamics analysis of GFM-WTs can be delineated as follows:

- Existing research mainly relies on extensive numerical simulations to assess the impact of GFM control on torsional dynamics. This necessitates the need for direct analytical methods to derive torsional modes, providing clear analytical insights.
- There is a notable gap in understanding how converter control strategies affect the torsional dynamics within GFM-WT systems. This gap calls for a comparative analysis through the development of reduced-order small-signal models under different GFM-WT configurations.
- The effects of various system parameters on the torsional behavior of GFM-WTs remain unclear. The FNN-based PDA emerges as a promising approach to address this issue. This method allows for the simultaneous assessment of the impact that multiple and variable system parameters have on torsional modes, offering a more holistic view of system dynamics.

1.3 Research Objectives and Limitations

1.3.1 Research Questions

The main objective of this Ph.D. study is to advance the understanding of the small-signal stability of GFM-WTs, with a particular focus on the development of small-signal models for analyzing electromagnetic/electromechanical dynamics under different converter controls. The overall objective of this Ph.D. study is condensed into the following research question:

What is the impact of various converter control strategies on the small-signal stability of grid-forming permanent magnet synchronous generator wind turbines?

Based on the overall research query, several sub-questions are formulated:

- How can ac impedance model be developed to accurately analyze the electromagnetic small-signal stability of GFM-MPMSGs?
- How to include mechanical dynamics, specifically torsional dynamics, for the electromechanical small-signal stability analysis of GFM-WTs?
- What influence does GFM-MWT control introduce on the torsional dynamics of WTs?
- How do varying converter control strategies affect the torsional dynamics of GFM-WTs and what are the impacts on their small-signal stability?
- How do control and system parameters affect the torsional dynamics of GFM-WTs?

1.3.2 Research Objectives

Aligned with the research questions outlined, this thesis sets forth the following objectives:

- **Impedance modeling and electromagnetic dynamics analysis for grid-connected GFM-MPMSGs:** This objective involves the development of a small-signal model for GFM-MPMSGs by considering the electromagnetic dynamics only, based on which, the dynamics impact of MSC and generator on the ac equivalent impedance of GFM-MPMSGs will be characterized. By analyzing the ac equivalent impedance, we aim to shed light on the small-signal stability of GFM-MPMSG systems when integrated into the grid.
- **Small-signal modeling and analysis of torsional vibrations in GFM-MWTs:** The goal here is to develop small-signal models that focus on electromechanical dynamics, including the two-mass drive train system and aerodynamics of the turbine, as well as turbine controls like MPPT and pitch angle control. Based on the developed small-signal models, the complex torque coefficients method is utilized to derive the torsional modes of GFM-MWTs. This will facilitate an in-depth analysis of torsional vibrations within GFM-MWTs and assess how GFM controls influence torsional dynamics.
- **Exploration of control strategy impacts on torsional dynamics:** By establishing specific small-signal models for different control strategies, including GFM-GWT configuration and GFM-MWT with different DVCs, this objective aims to assess how different control strategies would affect torsional dynamics of WTs. Using the complex torque coefficients method to calculate torsional modes will highlight the distinct effects of each control approach.
- **Assessment of the impact of varying system parameters on torsional dynamics:** Introducing an FNN-based PDA method, this objective seeks to quantify the simultaneous impact of various system parameters on the torsional dynamics of GFM-WTs under different control strategies. This sensitivity analysis will consider all relevant system and control parameters, offering a holistic view of their effects on the torsional modes of GFM-WTs.

1.3.3 Project Limitations

In addressing the complexities inherent in wind turbine systems, this study necessarily employs certain assumptions and simplifications to manage the scope of analysis. The following limitations of this thesis are highlighted:

- The mechanical dynamics of wind turbines are principally represented by a 2-mass drive train model equipped with aerodynamics equations, excluding detailed models for blades and towers.
- The focus within electromechanical dynamics is predominantly on torsional dynamics, given their critical impact on system stability.
- This research is confined to the study of Type-IV WTs, which employ gearless PMSGs.
- The grid voltage is assumed to be purely sinusoidal at the fundamental frequency for this study, excluding the potential influence of harmonic distortions present from the grid side.
- This work is focused on small-signal stability, with large-signal disturbances (e.g., grid fault) not being within the scope of this investigation.
- The role of auxiliary devices within the power system, i.e. energy storage systems, is not considered in this thesis.

1.4 Thesis Outline

This thesis is structured to reflect the progression and outcomes of the research conducted within this Ph.D. project, correlating closely with the published articles. It is divided into two principal parts: the **Report** and the **Publications**. Figure 1.6 delineates the structure of the thesis, illustrating the linkages between individual chapters and associated publications.

The report is systematically arranged into six primary chapters:

Chapter 1 establishes the foundation by outlining the research background, objectives, and hypotheses that support the thesis.

Chapter 2 is dedicated to obtaining the ac electromagnetic impedance model for the GFM-MPMSG, starting with the development of a small-signal model for the GFM-controlled GSC, followed by building the dc-side impedance model of the MSC, including the generator. The analysis of dc impedance model of the MSC and generator reveals its negligible effect on the ac interactions between the GFM-MPMSG and the grid, suggesting that the dynamics of the GSC are crucial when analyzing the middle-frequency stability of GFM-MPMSG connecting to the ac grid.

Chapter 3 expands the analysis of Chapter 2 to include mechanical dynamics to study electromechanical dynamics within the GFM-MWT. Through the development of a reduced-order small-signal model and application of the complex torque coefficients method, this chapter derives and examines the expressions of natural frequency and damping ratio of torsional modes,

Small-signal stability analysis and control of grid-forming Type IV wind turbines

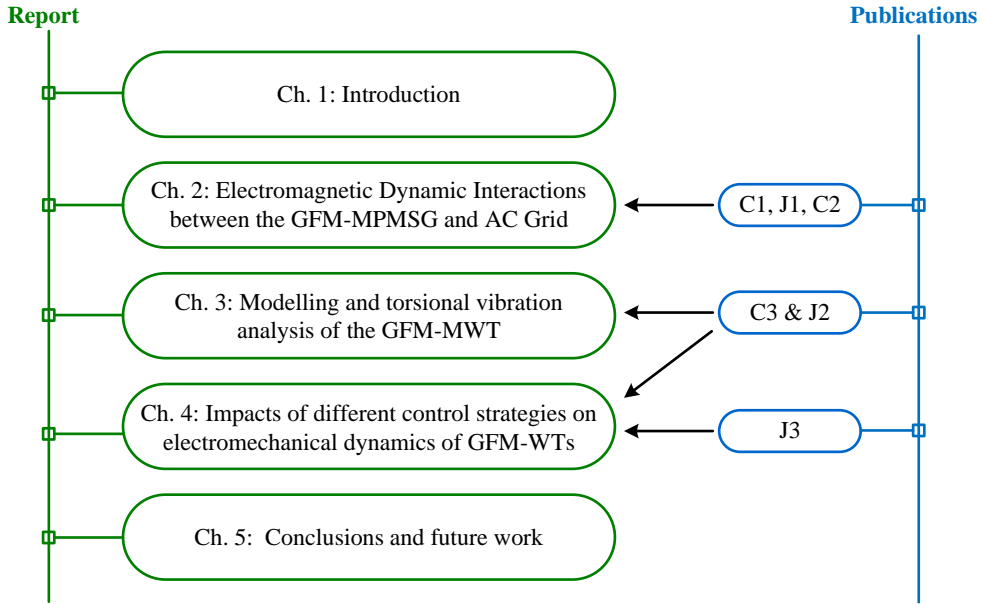


Figure 1.6: Thesis structure and corresponding publications.

uncovering the introduction of negative damping effects in the GFM-MWT configuration.

Chapter 4 investigates the impact of various converter control strategies on the electromechanical dynamics of GFM-WTs. By developing reduced-order small-signal models for GFM-WTs under different converter controls and employing the complex torque coefficients method, this chapter derives the torsional modes with varying converter controls. Furthermore, the application of an FNN-based PDA method elucidates the distinct impacts of system parameters on the torsional dynamics across different control strategies.

Finally, **Chapter 5** summarizes the principal contributions of this Ph.D. study and proposes future research directions and applications of GFM-WT technologies.

1.5 List of Publications

The outcomes of this project are published in the following publications, some of which are selected in the thesis for assessment.

Journal Papers

- [J1] **Shiyi Liu**, Heng Wu, Xiongfei Wang, Theo Bosma, Ganesh Sauba, "*Stability Analysis and Active Damping Design for Grid-Forming Converters in LC Resonant Grids*," in IEEE Open Journal of the Industrial Electronics Society, vol. 5, pp. 143-154, 2024.
- [J2] **Shiyi Liu**, Heng Wu, Theo Bosma, Xiongfei Wang, "*Impact of DC-Link Voltage Control on Torsional Vibrations in Grid-Forming PMSG Wind Turbines*," in IEEE Trans. Energy Conversion (early access), 2024.
- [J3] **Shiyi Liu**, Razvan Gabriel Cirstea, Heng Wu, Theo Bosma, Xiongfei Wang, "*Comparative Analysis of the Influence of Converters Control Strategies on Torsional Dynamics in Grid-Forming Wind Turbines*," under review in IEEE Trans. Sustainable Energy, 2024.

Conference Papers

- [C1] **Shiyi Liu**, Heng Wu, Xiongfei Wang, Theo Bosma, Jos van der Burgt, Ganesh Sauba, Ravi Singh, "*Active damping of power control for grid-forming inverters in lc resonant grids*," in 2022 IEEE Energy Conversion Congress and Exposition (ECCE), pp. 1-6, 2022.
- [C2] **Shiyi Liu**, Heng Wu, Liang Zhao, Xiongfei Wang, Theo Bosma, Jos van der Burgt, Ganesh Sauba, "*Impact of Machine-Side Converter Dynamics on AC Impedance of Grid-Forming PMSG Wind Turbines*," in 2023 IEEE Applied Power Electronics Conference and Exposition (APEC), pp. 1339-1344, 2023.
- [C3] **Shiyi Liu**, Heng Wu, Xiongfei Wang, Artur Avazov, Xavier Guillaud, Theo Bosma, Ganesh Sauba, "*Torsional vibration analysis of grid-forming PMSG wind turbine*," in 22nd Wind and Solar Integration Workshop (WIW 2023), 2023.

1.6 Experimental Setup Utilized in This Thesis

The thesis presents experimental findings using a simplified model of a GFM-MPMSG, as illustrated in Fig. 1.7. The model includes the following subsystems:

- Grid-side Subsystem: This includes the grid simulator and the grid inductor.
- Converter-side Subsystem: It consists of a back-to-back converter, L-C filters, and a dc-link capacitor.

1.6. Experimental Setup Utilized in This Thesis

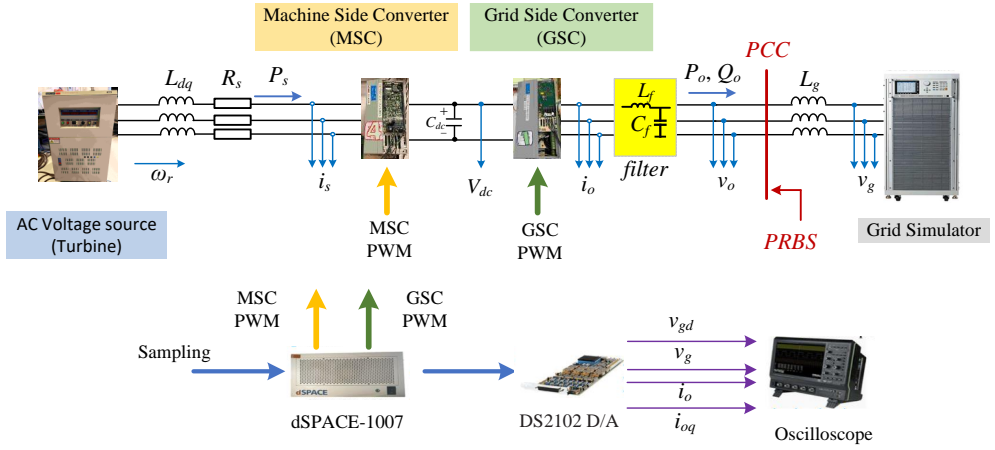


Figure 1.7: Experiment Setup for GFM-MPMSGs.

- **Simplified Generator Subsystem:** It is represented by an ac voltage source connected with a stator inductor and its parasitic resistance.
- **Control System:** The control algorithms are implemented using a dSPACE system, specifically the DS1007 dSPACE platform and DS2101 D\A board output board.

Table 1.1: Parameters used in the experiment

Parameters	Values
Stator inductor L_{dq} (mH)	0.7552
Parasitic resistance R_s (Ω)	0.05
Magnetic flux ψ_m (Wb)	0.42
Grid frequency (Hz)	50
dc-link capacitor C_{dc} (F)	$1.45e^{-3}$
Rated wind speed V_w (m/s)	12
dc-link voltage V_{dc} (V)	600
Rated power P_{ref} (W)	1500
Grid voltage $V_{g_{p-g}rms}$ (V)	110

In addition, the control commands for the dSPACE system are generated via a computer, and the resulting output waveforms are captured using an oscilloscope. The magnitude and frequency of the equivalent generator voltage are computed based on the chosen operational point, the basic parameters are listed in Table 1.1, while the detailed parameters for each experimental case are elaborated in the respective chapters.

Chapter 1. Introduction

Chapter 2

Electromagnetic Dynamic Interactions between the GFM-MPMSG and AC Grid

2.1 Introduction

With the increased penetration of type-IV WTs into power systems, dynamic interactions between WTs and ac power grids have become increasingly significant. A number of issues with stabilizing WT-grid interactions under small disturbances have recently been reported [27]. Therefore, it is important to develop an accurate small-signal model of the type-IV WT.

For traditional GFL-WT, previous analyses [21,27] have indicated that the MSC and generator can often be disregarded when analyzing its interaction with the power grid due to the low bandwidth of the DVC [33]. Consequently, the dc-link capacitance is often modeled as an ideal dc voltage source in the small-signal analysis of dynamic interactions between GFL-WTs and the grid.

However, studies in [34,36] solely focus on the GFL-WTs. For GFM-WTs, it is essential to revisit the impact of the MSC and generator electromagnetic dynamics on WT-grid interactions due to the different internal control dynamics of the MSC and GSC. In the case of GFM-GPMSGs, the dynamics of the MSC can also be overlooked due to the low bandwidth of DVC with the MSC [15,16]. As for GFM-MPMSGs, the impacts of the MSC and the PMSG on the grid-side dynamics of GFM-MPMSGs remain unexplored [43]. Therefore, it is crucial to reassess how the electromagnetic dynamics of the MSC and the PMSG affect grid interactions of GFM-MPMSGs under small disturbances.

This chapter aims to bridge this gap by developing an ac equivalent impedance model for GFM-MPMSGs, concentrating on its electromagnetic

dynamics at the grid side. Beginning with a small-signal model of the Grid-forming control Grid-side Converter (GFM-GSC), the analysis extends to constructing a small-signal model for the MSC, from which, the dc output impedance of the MSC is derived. Our findings indicate that the influence of MSC dynamics on the ac equivalent impedance of GFM-MPMSGs is minimal, primarily due to the magnitude of dc output impedance being below 0 dB. This result underscores the predominant role of GFM converter dynamics in the interactions between GFM-MPMSGs and the grid. To support the theoretical findings, the chapter concludes with nonlinear time-domain simulations and experimental tests. By offering a detailed methodological exploration and experimental validation, this work contributes to the ongoing development of GFM-WTs.

2.2 System Description

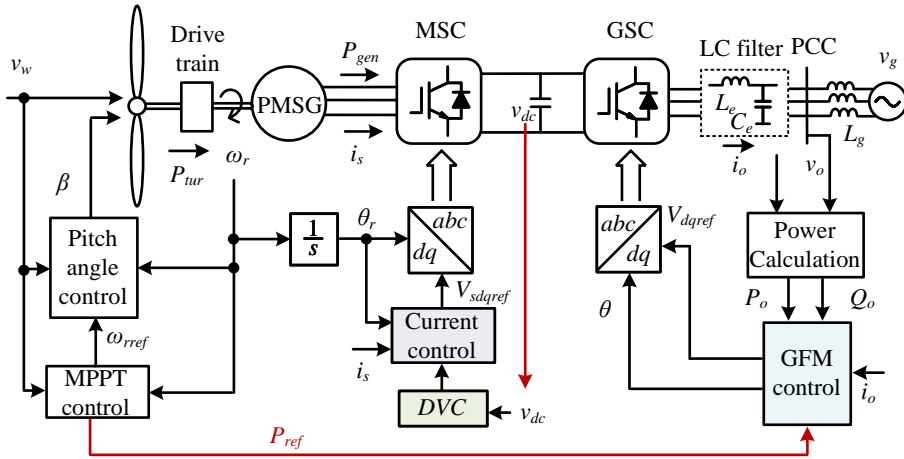


Figure 2.1: Structural depiction of the GFM-MWT

The GFM-MWT system, as introduced by the recent research [53, 54], is presented as shown in Fig. 2.1 where the PMSG is connected to the Point of Common Coupling (PCC) via a B2B converter. This B2B converter configuration is composed of an MSC, a GSC, and a dc-link capacitor (C_{dc}), which facilitates the energy conversion. The wind turbine model includes three-phase blades connected to the rotor, a two-mass drive train, and a generator, equipped with pitch angle control and MPPT [55]. This control strategy uses wind velocity (v_w) and rotor angular velocity (ω_r) to optimize the reference power (P_{ref}) for the GSC, thus maximizing energy capture from varying wind conditions. The generator output power is denoted as P_{gen} .

2.2. System Description

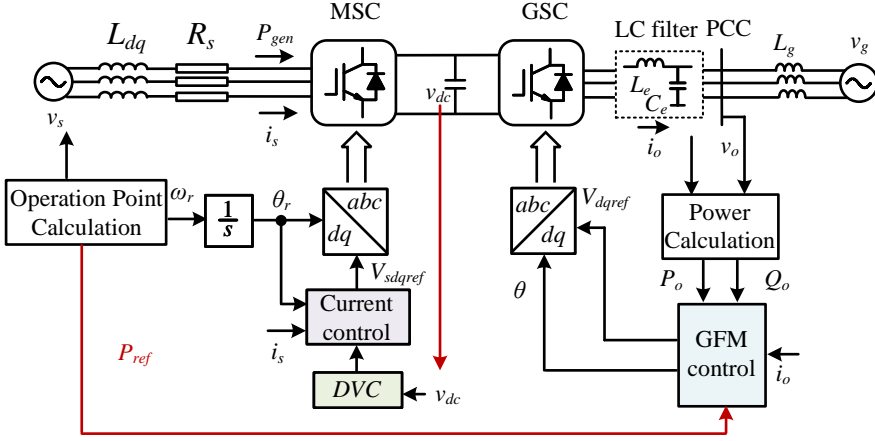


Figure 2.2: Structural depiction of the GFM-MPMSG

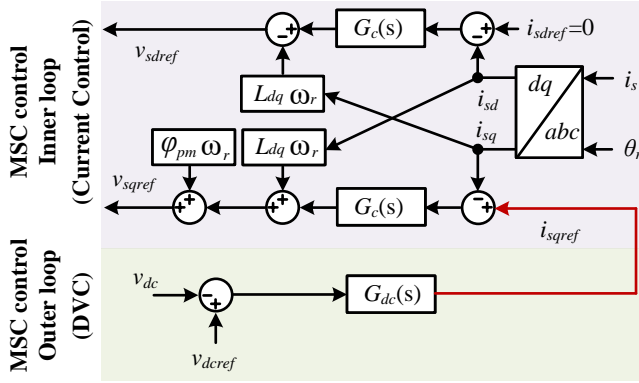


Figure 2.3: MSC control structure

Given the focus of this chapter on electromagnetic dynamics, the mechanical aspects of wind turbines, such as the drive train and turbine control, can be ignored, which is justified by the relatively slow dynamics of these mechanical components [56]. The electromagnetic dynamics are mathematically described in the d/q -axis of the synchronous reference frame [43], aiding analysis of the grid interactions of GFM-MPMSG, defined as

$$\begin{bmatrix} u_{sd} \\ u_{sq} \end{bmatrix} = \{(R_s + sL_{dq})\mathbf{I} + \omega_r L_{dq}\mathbf{J}\} \begin{bmatrix} -i_{sd} \\ -i_{sq} \end{bmatrix} + \begin{bmatrix} 0 \\ \omega_r \psi_{pm} \end{bmatrix} \quad (2.1)$$

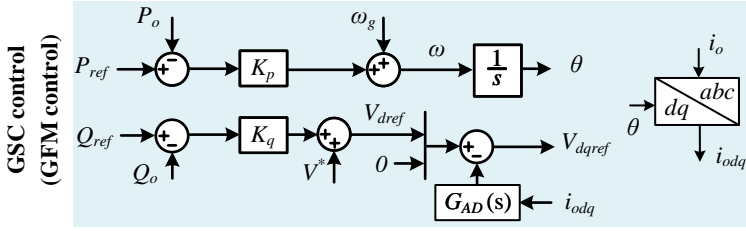


Figure 2.4: GSC control structure

where

$$\mathbf{I} = \begin{bmatrix} 1 & 0 \\ 0 & 1 \end{bmatrix} \quad (2.2)$$

$$\mathbf{J} = \begin{bmatrix} 0 & -1 \\ 1 & 0 \end{bmatrix} \quad (2.3)$$

$$i_{sq} = \frac{1}{1.5\psi_{pm}} T_{gen} \quad (2.4)$$

$$T_{gen} = \frac{P_{gen}}{\omega_r} \quad (2.5)$$

R_s signifies the stator resistance and L_{dq} is the inductor of the stator, characterizing the electromagnetic properties of the generator. The constant magnetic flux produced by the permanent magnets of the generator is denoted by ψ_{pm} , a crucial factor in defining the efficiency. The stator current and voltage in the d and q axis, denoted as i_{sd} , i_{sq} , u_{sd} , and u_{sq} separately, are essential for describing the power conversion dynamics and can be calculated by T_{gen} , the generator torque, derived from operational point calculations, linking mechanical power generation to electrical output.

The simplified electromagnetic model of the GFM-MWT, represented as the GFM-MPMSG, is shown in Fig. 2.2 for the impedance-based analysis. By substituting the turbine with a three-phase voltage source connected through R_s and L_{dq} , the model focuses on the small-signal dynamics that determines the response of the system to electromagnetic disturbances of the grid.

As shown in Fig. 2.2, the output active power, reactive power, the voltage of the converter bridge, and the voltage of the PCC are represented by P_o , Q_o , v_{inv} , and v_o , respectively. The inductance current, denoted as i_o , flows through inductance L_e , and i_g is the grid current. The grid impedance and shunt ac capacitor are represented by L_g and C_e , respectively, with C_e resulting from shunt capacitor branches for reactive power compensation or from capacitive loads inherent in the system.

The detailed control strategies of the MSC and GSC are outlined in Fig. 2.3 and Fig. 2.4, respectively. For the MSC, a DVC is employed within its outer

2.2. System Description

loop to regulate the dc-link voltage v_{dc} , accompanied by an inner-loop current control that processes feedback from the i_s , as emphasized in green in Fig. 2.3. The DVC aims to control the dc-link voltage, defined by

$$i_{sqref} = G_{dc}(s)(v_{dcref} - v_{dc}) \quad (2.6)$$

where $G_{dc}(s)$ is a function of proportional k_{pdc} and integral k_{idc} gains over the Laplace variable s .

The current control loop generates modulation signals v_{sdref} and v_{sqref} based on the reference current i_{sqref} , described by

$$\begin{aligned} v_{sdref} &= G_c(s)(i_{sdref} - i_{sd}) - \omega_r L_{dq} i_{sq} \\ v_{sqref} &= G_c(s)(i_{sqref} - i_{sq}) + \omega_r L_{dq} i_{sd} + \omega_r \psi_{pm} \end{aligned} \quad (2.7)$$

where

$$\begin{aligned} i_{sqref} &= \frac{1}{1.5\psi_{pm}} T_{genref} \\ G_c(s) &= k_{cP} + \frac{k_{cI}}{s} \end{aligned} \quad (2.8)$$

The GSC control scheme, aiming to synchronize with the power grid via Active Power Control (APC), is illustrated in Fig. 2.4, expressed as,

$$\theta = \frac{1}{s} [\omega_g + K_p (P_{ref} - P_o)] \quad (2.9)$$

where θ is the reference angle and P_{ref} is the reference power, with ω_g and K_p signifying the fundamental frequency of the grid and the active power-frequency droop coefficient, respectively.

Reactive Power Control (RPC) adopts a Reactive Power-voltage (Q-V) droop strategy for voltage magnitude regulation:

$$V_{ref} = V^* + K_q (Q_{ref} - Q_o) \quad (2.10)$$

where the reference of reactive power and the voltage magnitude are denoted by Q_{ref} and V_{ref} , and $V_{ref} = V_{dref}$ as V_{qref} is set to be zero. The nominal voltage magnitude is represented by V^* , while K_q denotes the Q-V droop coefficient. Besides, the GSC control system employs active damping, facilitated by a High-pass Filter (HPF), to mitigate the fundamental-frequency resonance within the APC loop, enhancing system stability [57].

Lastly, the instantaneous active and reactive power dynamics can be calculated by [10]:

$$\begin{bmatrix} P_o \\ Q_o \end{bmatrix} = \frac{3}{2} \begin{bmatrix} \mathbf{v}_{odq}^T \mathbf{i}_{odq} \\ \mathbf{v}_{odq}^T \mathbf{j}_{odq} \end{bmatrix} \quad (2.11)$$

2.3 Impedance Modeling

In developing the impedance model of the GFM-MPMSG system, a generic state variable is represented by x , with its steady-state value denoted as X_0 and small-signal deviations indicated by \hat{x} . For clarity in vector representation, real vectors are showcased in bold italics, such as $\text{test}x_{dq} = [x_d \ x_q]^\top$.

2.3.1 Grid-side Converters

The formulation of a small-signal model for the GFM-GSC is based on the establishment of dual-rotating dq reference frames: one synchronized with the grid voltage phase angle, referred to as the system- dq frame, and the other aligned with the angle generated from the APC, known as the controller- dq frame. For ease of distinction, variables associated with the system- dq frame carry a superscript s , while those related to the controller- dq frame bear a superscript c , as presented in Fig. 2.5.

The phase angle difference between the controller dq frame and the system dq frame is represented as δ , where $\delta = \theta - \theta_g$, with θ_g set to zero for reference. δ facilitates the transformation of state variables from the controller dq frame (\mathbf{x}_{dq}^c) to the system-aligned dq frame (\mathbf{x}_{dq}^s), following the transformation equation:

$$\mathbf{x}_{dq}^c = \begin{bmatrix} \cos\delta & \sin\delta \\ -\sin\delta & \cos\delta \end{bmatrix} \mathbf{x}_{dq}^s \quad (2.12)$$

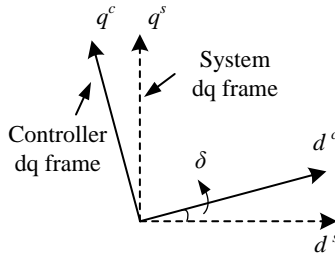


Figure 2.5: Controller dq frame and system dq frame.

Rewriting state variables with their corresponding steady-state values and small-signal perturbations, i.e., $x = X_0 + \hat{x}$, the small-signal representation of the relationship between \mathbf{x}_{dq}^s and \mathbf{x}_{dq}^c can be expressed as

$$\hat{\mathbf{x}}_{dq}^c = \begin{bmatrix} \cos\delta_0 & \sin\delta_0 \\ -\sin\delta_0 & \cos\delta_0 \end{bmatrix} \hat{\mathbf{x}}_{dq}^s - \underbrace{\delta}_{\mathbf{G}_{s0}} \begin{bmatrix} \cos\delta_0 & \sin\delta_0 \\ -\sin\delta_0 & \cos\delta_0 \end{bmatrix} \begin{bmatrix} -X_{q0}^s \\ X_{d0}^s \end{bmatrix} \quad (2.13)$$

2.3. Impedance Modeling

Then the small-signal model of the output active and reactive power can be formulated as follows

$$\begin{bmatrix} \hat{P}_o \\ \hat{Q}_o \end{bmatrix} = \frac{3}{2} \left(\underbrace{\begin{bmatrix} \mathbf{I}_{odq0}^T \\ -\mathbf{I}_{odq0}^T \mathbf{J} \end{bmatrix}}_{\mathbf{I}_{o0}} \hat{\mathbf{v}}_{odq}^s + \underbrace{\begin{bmatrix} \mathbf{V}_{odq0}^T \\ \mathbf{V}_{odq0}^T \mathbf{J} \end{bmatrix}}_{\mathbf{V}_{o0}} \hat{\mathbf{i}}_{odq}^s \right) \quad (2.14)$$

According to Fig. 2.4, $\hat{\mathbf{v}}_{invdq}^c$ can be expressed as

$$\hat{\mathbf{v}}_{invdq}^c = \hat{\mathbf{v}}_{invdqref}^c - \mathbf{G}_{AD}(s) \hat{\mathbf{i}}_{odq}^c \quad (2.15)$$

where $\mathbf{G}_{AD}(s)$ represents the transfer function matrix of the active damping, which is expressed as

$$\mathbf{G}_{AD}(s) = \begin{bmatrix} G_{AD}(s) & 0 \\ 0 & G_{AD}(s) \end{bmatrix} \quad (2.16)$$

By substituting (2.13), the small-signal representation of (2.15) in system dq frame can be obtained as

$$\hat{\mathbf{v}}_{invdq}^s = \underbrace{\begin{bmatrix} -V_{invq0} - \frac{sk_v}{s+\omega_v} I_{oq0} & \cos\delta_0 \\ V_{invd0} + \frac{sk_v}{s+\omega_v} I_{od0} & \sin\delta_0 \end{bmatrix}}_{\mathbf{G}_T} \begin{bmatrix} \hat{\delta} \\ \hat{V} \end{bmatrix} - \mathbf{G}_{AD}(s) \hat{\mathbf{i}}_{odq}^s \quad (2.17)$$

Under the assumption that the three-phase system is symmetrical and $\hat{\mathbf{v}}_{gdq}^s = 0$, by applying Kirchhoff's voltage law and Laplace transformation [58], the circuit dynamics can be expressed as,

$$\begin{aligned} \hat{\mathbf{v}}_{invdq}^s &= \hat{\mathbf{v}}_{odq}^s + \mathbf{Z}_e(s) \hat{\mathbf{i}}_{odq}^s \\ \hat{\mathbf{i}}_{odq}^s &= \hat{\mathbf{i}}_{gdq}^s + \mathbf{Y}_c(s) \hat{\mathbf{v}}_{odq}^s \\ \hat{\mathbf{v}}_{odq}^s &= \mathbf{Z}_g(s) \hat{\mathbf{i}}_{gdq}^s \end{aligned} \quad (2.18)$$

where

$$\begin{aligned} \mathbf{Z}_e(s) &= \begin{bmatrix} sL_e + R_e & -L_e\omega_g \\ L_e\omega_g & sL_e + R_e \end{bmatrix} \\ \mathbf{Y}_c(s) &= \begin{bmatrix} sC_e & -C_e\omega_g \\ C_e\omega_g & sC_e \end{bmatrix} \\ \mathbf{Z}_g(s) &= \begin{bmatrix} sL_g + R_g & -L_g\omega_g \\ L_g\omega_g & sL_g + R_g \end{bmatrix} \end{aligned} \quad (2.19)$$

R_e and R_g represent the parasitic resistance of the LC filter and the grid, which are much smaller than the inductance ($R_g \ll L_g$ and $R_e \ll L_e$) [59].

According to (2.14) and (2.18), we can obtain the transfer function matrix from $[\hat{\delta} \ \hat{V}]^T$ to $[\hat{P} \ \hat{Q}]^T$, as given in in (2.20), and its corresponding block diagram is illustrated in the blue part in Fig. 2.6.

$$\begin{aligned} \begin{bmatrix} \hat{P} \\ \hat{Q} \end{bmatrix} &= 1.5\{\mathbf{I}_{o0} + \mathbf{V}_{o0}[\mathbf{Y}_c(s) + \mathbf{Z}_g^{-1}(s)]\} \\ &\cdot \underbrace{\{\mathbf{I} + [\mathbf{Z}_e(s) + \mathbf{G}_{AD}(s)][\mathbf{Y}_c(s) + \mathbf{Z}_g^{-1}(s)]\}^{-1} \mathbf{G}_T(s)}_{\begin{bmatrix} G_{\delta P} & G_{VP} \\ G_{\delta Q} & G_{VQ} \end{bmatrix}} \begin{bmatrix} \hat{\delta} \\ \hat{V} \end{bmatrix} \end{aligned} \quad (2.20)$$

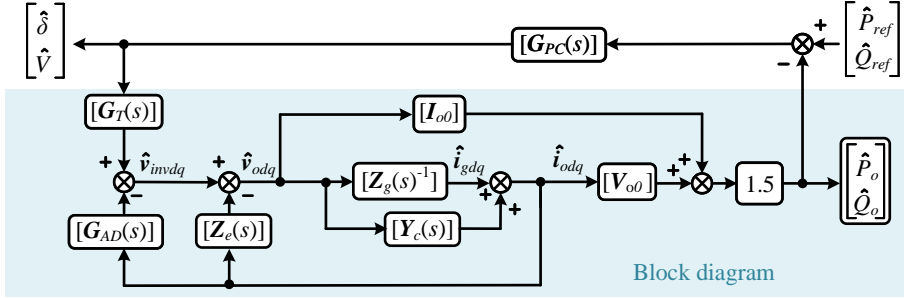


Figure 2.6: Block diagram and small-signal model of the GFM-GSC with ac capacitors.

Substituting (2.20) into (2.9), and (2.10), we can obtain the small-signal model of the GFM-GSC, as demonstrated in Fig. 2.6, where

$$\mathbf{G}_{PC}(s) = \begin{bmatrix} \frac{K_p}{s} & 0 \\ 0 & K_q \end{bmatrix} \quad (2.21)$$

Therefore, the loop gain of APC and RPC loops of the GFM-GSC can be expressed as,

$$\begin{bmatrix} T_{\delta P} & T_{VP} \\ T_{\delta Q} & T_{VQ} \end{bmatrix} = \begin{bmatrix} G_{\delta P} & G_{VP} \\ G_{\delta Q} & G_{VQ} \end{bmatrix} \mathbf{G}_{PC}(s) \quad (2.22)$$

If the shunt ac capacitors are not included, the block diagram and small-signal model of the GFM-GSC will be Fig. 2.7, where the transfer functions of

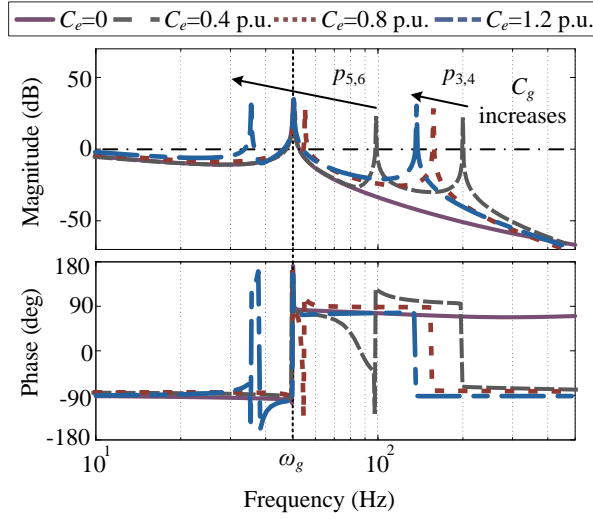


Figure 2.8: Bode plot of the APC with different ac shunt capacitors, $L_e = 0.5$ p.u., $SCR=1.5$, without active damping.

is given by,

$$T_{c\delta P} = (G_{\delta P} + G_{coupled}) \frac{K_p}{s} \quad (2.26)$$

where

$$G_{coupled} = G_{\delta Q} \frac{-K_q}{1 + K_q G_{VQ}} G_{VP} \quad (2.27)$$

Without active damping ($k_v = 0$), the bode plots of the equivalent APC with different C_e can be obtained by solving (2.26), as illustrated in Fig. 2.9.

While the magnitudes and frequencies of some resonant peaks are slightly altered by taking P/Q coupling into account in the equivalent APC loop gain, the fact that the presence of shunt ac capacitors introduces two additional resonant peaks remains unchanged.

Therefore, if shunt ac capacitors are present, to ensure the stable operation of GFM-GSC, it is important to select ω_v by taking all resonant peaks into account [43]. Especially in the scenario of the value of $\sqrt{\frac{L_e + L_g}{L_e L_g C_e}}$ is close to $2\omega_g$, the angular frequency of the complex poles $p_{5,6}$ can become very close to or even lower than ω_g . In such case, selecting $\omega_v < \omega_g$ can not effectively dampen the resonant peak [9]. More details can be found in [9,43].

2.3. Impedance Modeling

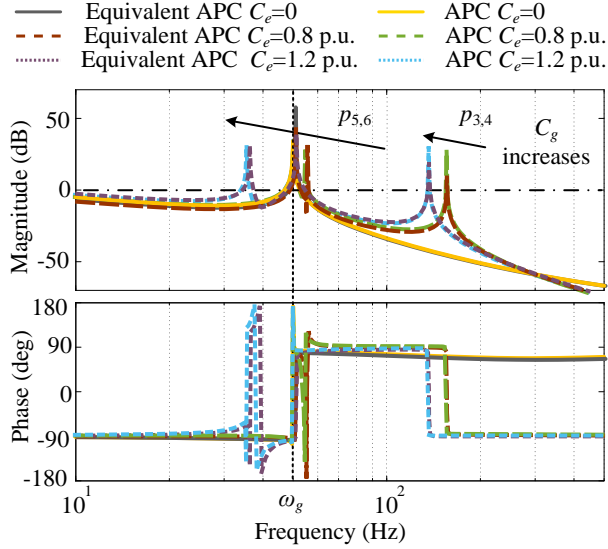


Figure 2.9: Bode plots of the APC and equivalent APC with different capacitors, $L_e = 0.5$ p.u., SCR=1.5, without active damping.

2.3.2 Machine-side Converters

By combining (2.1) and (2.7), coefficients of the inner loop of the MSC can be simplified as,

$$\begin{aligned} k_{cp} &= \omega_c L_{dq} \\ k_{ci} &= \omega_c R_s \end{aligned} \quad (2.28)$$

where ω_c is the cut-off frequency of the open loop transfer function.

Based on the electromagnetic dynamics of the generator and MSC [43], the small-signal transfer function of the open-loop MSC can be given by,

$$\begin{bmatrix} \hat{v}_{dc} \\ -\hat{i}_{sd} \\ -\hat{i}_{sq} \end{bmatrix} = \begin{bmatrix} Z_{dc} & T_{sid} & T_{siq} & G_{cid} & G_{ciq} \\ G_{isd} & -Y_{sdd} & -Y_{sqd} & G_{csdd} & G_{csqd} \\ G_{isq} & -Y_{sdq} & -Y_{sqq} & G_{csdq} & G_{csqq} \end{bmatrix} \cdot \begin{bmatrix} -\hat{i}_{dc} \\ \hat{v}_{sd} \\ \hat{v}_{sq} \\ \hat{v}_{sdref} \\ \hat{v}_{sqref} \end{bmatrix} \quad (2.29)$$

where Z_{dc} is the open-loop dc input impedance, expressed as

$$Z_{dc} = \left\{ \frac{3}{2} (V_{sqref0}^2 + V_{sdref0}^2) \frac{L_{dq} + R_s}{(L_{dq} + R_s)^2 + L_{dq}^2 \omega_{r0}^2} + sC_{dc} \right\}^{-1} \quad (2.30)$$

The equivalent circuit of the open-loop MSC is shown in Fig. 2.10.

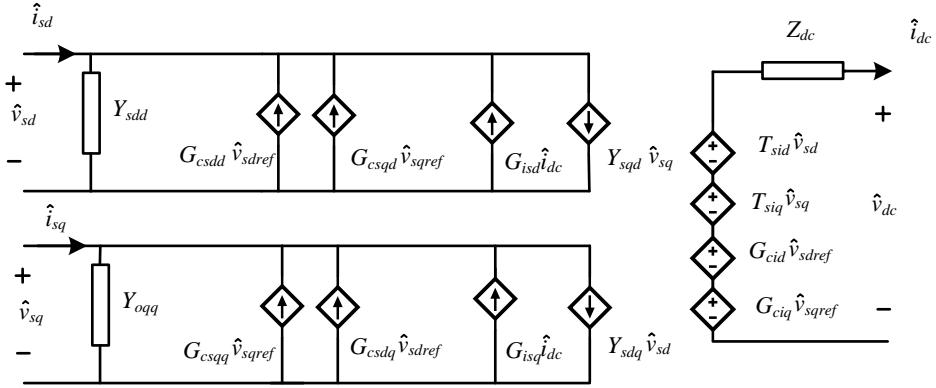


Figure 2.10: Equivalent impedance model of open-loop MSC.

For obtaining the closed-loop dc impedance of the MSC, by including the inner and outer loop controls of the MSC, the small-signal representation of the MSC is demonstrated as in Fig. 2.11, assuming there is no perturbation from the voltage inputs.

According to Fig. 2.11, we can derive the dc equivalent impedance of the closed-loop MSC, formulated as,

$$\begin{aligned}
 Z_{dcnew} = & \left\{ sC_{dc} + \frac{2P_{s0}L_{dq}^2\omega_c(k_{up} + \frac{k_{ui}}{s})(s^2 + sV_{dc0}\omega_c + \omega_c^2)}{2L_{dq}V_{sqref0}V_{dc0}(V_{dc0}^2\omega_c^2 + s^2 + 2sV_{dc0}\omega_c + \omega_r^2)} \right. \\
 & + [3L_{dq}V_{sqref0}V_{dc0}^2\omega_c(k_{up} + \frac{k_{ui}}{s}) - 2L_{dq}P_{s0}\omega_c + 3V_{sqref0}^2V_{dc0}] \quad (2.31) \\
 & \left. \cdot \frac{(sV_{sqref0} + V_{sqref0}V_{dc0}\omega_c + V_{sdref0}\omega_{r0})}{2L_{dq}V_{sqref0}V_{dc0}(V_{dc0}^2\omega_c^2 + s^2 + 2sV_{dc0}\omega_c + \omega_r^2)} \right\}^{-1}
 \end{aligned}$$

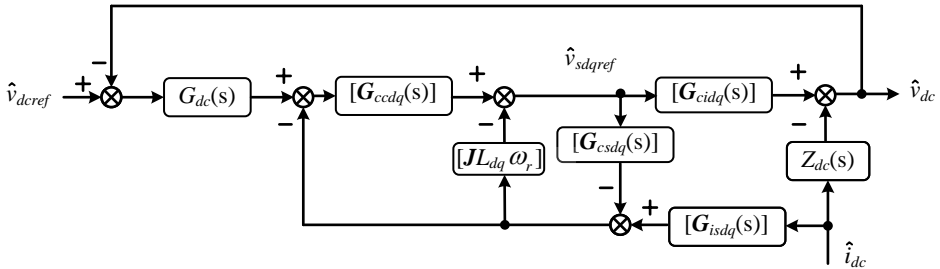


Figure 2.11: Small-signal representation of the closed-loop MSC.

To explore the characteristic of dc equivalent impedance for the MSC, based

2.3. Impedance Modeling

Table 2.1: Parameters used in the simulation for the GFM-MPMSG

Parameters	Set A	Set B
L_{dq} (p.u.)	0.513	0.513
R_s (p.u.)	0.027	0.027
C_{dc} (F)	$100e^{-3}$	$100e^{-3}$
V_w (m/s)	12	12
k_{dcp} (p.u.)	1	0.65
k_{dci} (p.u.)	100	20
w_c (rad/s)	1500	800
w_r (rad/s)	376.991	376.991
V_{dc} (V)	1150	1150
V_{gp-rms} (V)	400	400

on (2.30) and (2.31), the bode plots of Z_{dcnew} , Z_{dc} , and C_{dc} are demonstrated in Fig. 2.12, where two sets of parameters are used for comparison, given by Table. 2.1.

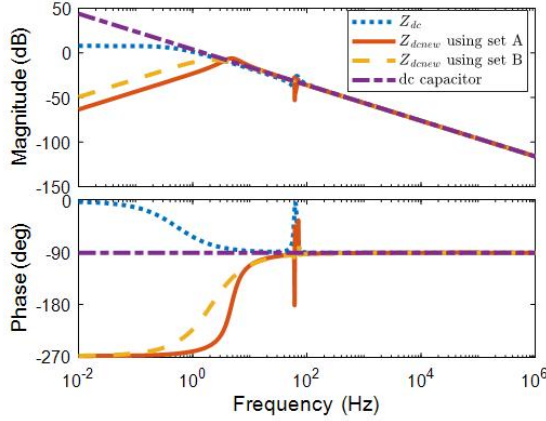


Figure 2.12: Bode plot comparison of C_{dc} , Z_{dc} , and Z_{dcnew} .

Fig. 2.12 reveals that both Z_{dc} and Z_{dcnew} are primarily influenced by C_{dc} at higher frequencies. However, at frequencies below 50 Hz, Z_{dc} behaves similarly to a resistive element, due to the generator impedance. While MSC control introduces an inductive behavior, as illustrated by the orange dashed line and red solid line in Fig. 2.12 through different control parameter sets, effectively reducing the dc impedance to below 0 dB.

Since the value of Z_{dcnew} is lower than 0 dB, it can be concluded that the dc output impedance of the MSC can be considered negligible in the

analysis of dynamic interactions between the GFM-MPMSG and the grid [61]. This finding simplifies the stability analysis, allows to merely consider the small-signal dynamics of the GFM-GSCs without significant loss of accuracy.

2.3.3 GFM-MPMSG

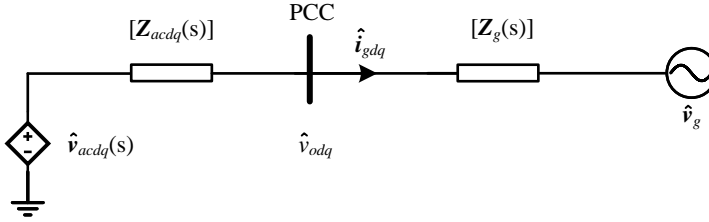


Figure 2.13: Equivalent ac impedance model of GFM-MPMSG.

Based on Section. 2.3.1 and 2.3.2, the equivalent impedance model of the GFM-MPMSG system can be obtained, as illustrated in Fig. 2.13, where the ac impedance of the GFM-MPMSG is given by

$$\mathbf{Z}_{acdq}(s) = \begin{bmatrix} Z_{acdd}(s) & Z_{acqd}(s) \\ Z_{acdq}(s) & Z_{acqq}(s) \end{bmatrix} \quad (2.32)$$

As the dc impedance model of the MSC can be neglected, when shunt ac capacitors are included, according to Fig. 2.6, $\mathbf{Z}_{acdq}(s)$ can be expressed as,

$$\mathbf{Z}_{acdq}(s) = [\mathbf{I} + \mathbf{G}_T(s)\mathbf{G}_{PC}(s)1.5(\mathbf{V}_{o0}\mathbf{Y}_c(s) + \mathbf{I}_{o0}) + \mathbf{Z}_e(s)\mathbf{Y}_c(s)]^{-1} \cdot [\mathbf{G}_T(s)\mathbf{G}_{PC}(s)1.5\mathbf{V}_{o0} + \mathbf{Z}_e(s) + \mathbf{G}_{AD}(s)] \quad (2.33)$$

If there is no shunt ac capacitor included in the system, as illustrated in Fig. 2.7, the expression of ac equivalent impedance for the GFM-MPMSG will be changed to

$$\mathbf{Z}_{acdq}(s) = [\mathbf{I} + \mathbf{G}_T(s)\mathbf{G}_{PC}(s)1.5\mathbf{I}_{o0}]^{-1} \cdot [\mathbf{G}_T(s)\mathbf{G}_{PC}(s)1.5\mathbf{V}_{o0} + \mathbf{Z}_e(s) + \mathbf{G}_{AD}(s)] \quad (2.34)$$

2.4 Model validation

2.4.1 Simulation Results

To verify the ac equivalent impedance model developed for the GFM-MPMSG system, nonlinear time-domain simulations are performed using MATLAB/Simulink along with the PLECS blockset. These simulations are based on the system

2.4. Model validation

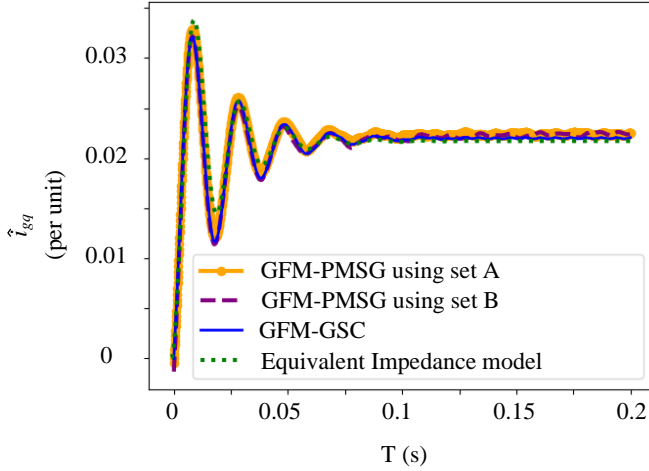


Figure 2.14: Response of \hat{i}_{gq} to a 0.01 p.u. step disturbance in v_{gb} for GFM-GSC and GFM-MPMSG using parameters sets A and B, compared with the equivalent impedance model.

configuration depicted in Fig. 2.2. Parameter sets A and B, detailed in Table 2.1, are used for these simulations. The analysis focused on comparing the simulated current responses, i_{gq} , against the theoretical impedance model predictions following the application of a step disturbance in v_{gb} .

The simulation results, illustrated in Fig. 2.14, reveal that the introduction of a 0.01 p.u. step disturbance to v_{gb} yields identical disturbance responses for i_{gq} across both GFM-GSC and GFM-MPMSG, no matter which parameter set is used. Notably, the error between the disturbance responses derived from the impedance model of GFM-MPMSG and those from the nonlinear simulations did not exceed 0.001 p.u., verifying the accuracy of the equivalent impedance model.

Moreover, this finding also implies that the MSC dynamics have limited influence on the overall ac impedance profile of GFM-MPMSGs, thereby reinforcing the accuracy of the equivalent impedance model of GFM-MPMSGs in capturing the essential electromagnetic dynamics of the system under study.

2.4.2 Experimental Results

To corroborate the theoretical insights and simulation findings, experiments are conducted using a simplified GFM-MPMSG wind turbine configuration as depicted in Fig. 1.7 where the parameters from Table 1.1 and 2.2 are used.

Table 2.2: Control parameters used in the experiment for the GFM-MPMSG

Parameters	k_{dcp} (p.u.)	k_{dci} (p.u.)	w_c (rad/s)
Set A*	1	100	1500
Set B*	0.65	20	800

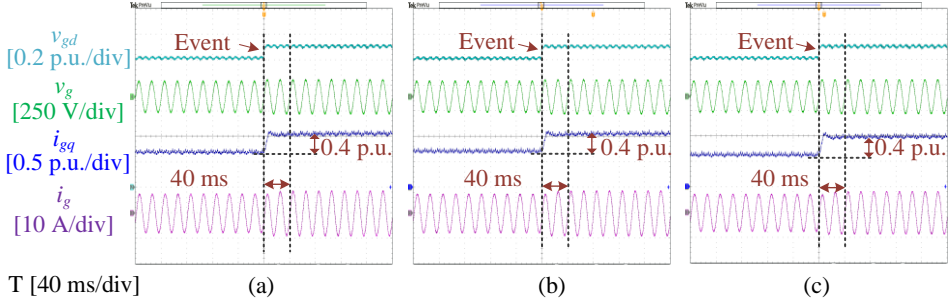


Figure 2.15: Experimental responses to a 0.1 p.u. step disturbance in v_{gd} : (a) GFM-GSC only. (b) GFM-MPMSG system with parameter set A*. (c) GFM-MPMSG system with parameter set B*.

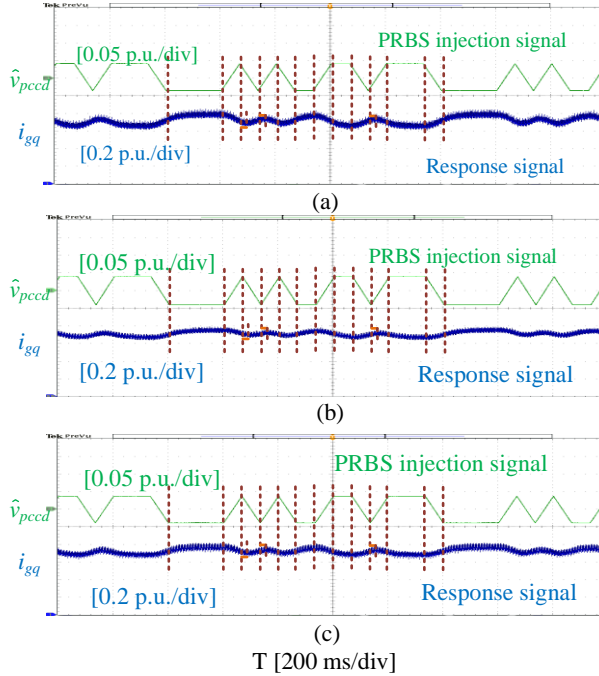


Figure 2.16: Experimental responses to PRBS disturbance at the PCC: (a) GFM-GSC only. (b) GFM-MPMSG system with parameter set A*. (c) GFM-MPMSG system with parameter set B*.

2.5. Summary

Initially, a 0.1 p.u. step disturbance is introduced to v_{gd} to evaluate the response of the system, as illustrated in Fig. 2.15. The responses of i_{gq} for the GFM-GSC and the GFM-MPMSG system under parameter sets A* and B* have consistent behavior across different configurations. This finding aligns with the simulation observations, concluding that the influence of MSC dynamics on the ac impedance of GFM-MPMSG is limited.

To further validate the negligible impact of MSC dynamics at low frequencies, a Pseudo-random Binary Sequence (PRBS) excitation signal ranging from 1-15Hz was applied to v_{pccd} at the PCC under steady conditions.

As illustrated in Fig. 2.16, the results demonstrate that the time delays between the excitation signal and the peak response across all test scenarios are the same, indicating that the presence of the MSC does not significantly alter the system's response to disturbances. Hence, these experimental findings, presented in Fig. 2.15 and 2.16 confirm the theoretical and simulation-based conclusion.

2.5 Summary

In this chapter, we develop and elucidate the equivalent ac impedance model of the GFM-MPMSG system. The impedance model is used for understanding the electromagnetic dynamics of GFM-MPMSGs, with a particular focus on their integration with the grid under small disturbances. The key contributions are summarized as follows:

1. The impedance model of the MSC and generator is developed and analyzed. It is found that the dc output impedance of the MSC has a negligible impact on the dc dynamics. Consequently, this insight leads to the conclusion that the impact of the MSC and PMSG on the ac dynamics of the GFM-MPMSG is limited, thereby simplifying the small-signal modeling and stability analysis.
2. The equivalent ac impedance model of the GFM-MPMSG system is developed. The accuracy of this impedance model is corroborated through simulation and experimental results.

Chapter 2. Electromagnetic Dynamic Interactions between the GFM-MPMSG and AC Grid

Chapter 3

Modelling and analysis of torsional vibrations in GFM-MWTs

3.1 Background

The previous chapter developed the small-signal model of GFM-MPMSG, focusing primarily on their electrical dynamics while ignoring mechanical dynamics. However, earlier investigations into such GFM-MWTs have observed the occurrence of torsional vibrations triggered by grid-side dynamics [45]. These vibrations pose significant risks, potentially impairing the lifetime and reliability of mechanical components of turbines and even inducing low-frequency oscillations that destabilize the grid [23,62].

In this chapter, our objective is to delve into the torsional dynamics analysis of GFM-MWTs. We develop the small-signal model of the GFM-MWTs, incorporating a two-mass drivetrain and wind turbine control system. This model serves as an important basis for examining the impact of GFM control on the electromechanical dynamics of GFM-MWTs.

Moving beyond the reliance on numerical simulations and analyses that were implemented in previous studies [39,46,63], this chapter introduces the application of the complex torque coefficients method [64]. This approach can help us to derive analytical expressions for the damping ratio, natural frequency, and damped frequency of torsional modes within the GFM-MWTs. Through this analysis, we seek to reveal the direct influence of GFM control on the damping ratio of torsional modes. Moreover, the impact of various system parameters—including the SCR, C_{dc} , wind speed, and specific GFM control parameters—on the torsional dynamics of GFM-MWTs are also demonstrated.

Our findings point to a critical insight: the GFM control strategy employed in GFM-MWTs has an adverse impact on the damping ratio of their torsional modes, thereby impairing system stability. The accuracy of the analytical conclusion is validated through comparisons with nonlinear time-domain simulations.

3.2 System Description

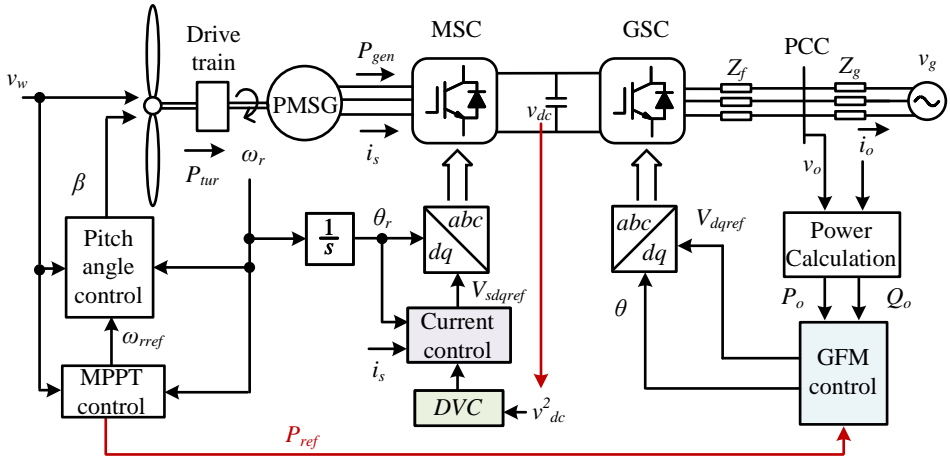


Figure 3.1: Structural depiction of the GFM-MWT

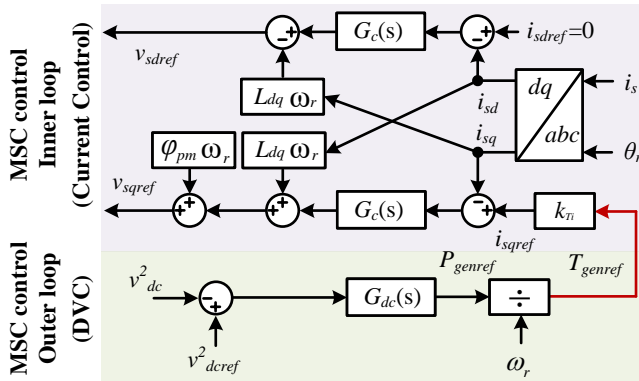


Figure 3.2: The control structure of MSC within the GFM-MWT

The GFM-MWT discussed in this chapter is depicted in Fig. 3.1, where the type IV wind turbine is connected to the PCC via an MSC and a GSC.

3.2. System Description

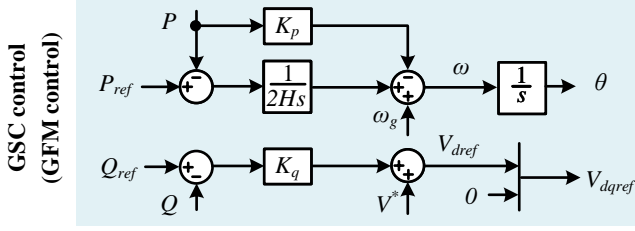


Figure 3.3: The control structure of GSC within the GFM-MWT

Fig. 3.2 outlines the control setup of the MSC, designed to regulate the dc-link voltage (v_{dc}) efficiently. The dynamic behavior of the dc-link voltage is given by:

$$C_{dc} \frac{d(v_{dc}^2)}{dt} = 2(P_{gen} - P_o) \quad (3.1)$$

where C_{dc} represents the dc-link capacitor, and P_{gen} and P_o are the generated and output powers, respectively.

The DVC feature of the MSC within the GFM-MWTs is governed by the following relation:

$$T_{genref} = \frac{G_{dc}(s)(v_{dc}^2 - v_{dc}^2)}{\omega_r} \quad (3.2)$$

with T_{genref} denoting the reference torque, and ω_r the rotor speed. The DVC ensures that the generated power aligns with the power requirements of the grid, maintaining dc-link voltage.

The input for the current control loop, i_{sqref} , is derived as $i_{sqref} = k_{Ti} T_{genref}$, where k_{Ti} is defined by:

$$k_{Ti} = \frac{1}{1.5\psi_{pm}} \quad (3.3)$$

This setup facilitates the generation of modulation signals to manage power flow efficiently. The inner loop control of the MSC is the same as presented in Chapter 2.

As illustrated in Fig. Figure 3.3 presents the APC strategy employed within the GSC of the GFM-MWTs:

$$\theta = \frac{1}{s} [\omega_g - K_p P_o + \frac{1}{2Hs} (P_{ref} - P_o)] \quad (3.4)$$

where θ is the control angle, ω_g the grid frequency, K_p the power-frequency droop coefficient, and H the inertia coefficient. This formula showcases the APC's role in synchronizing the wind turbine with the grid's frequency dynamics, enhancing system responsiveness and stability.

Similar to the approach in Chapter. 2.10, the regulation of reactive power involves adjusting the voltage magnitude at the PCC, ensuring optimal power delivery and grid compatibility.

3.3 Small-signal modeling of electromechanical dynamics of GFM-MWTs

This section develops the small-signal model of GFM-MWT systems including MSC, GSC, the corresponding control loops, the drive train, and aerodynamics.

3.3.1 Small-signal modeling of the MSC

The MSC inner-loop control and the theoretical PMSG model, whose electrical characteristics are given by (2.1), are presented in Fig. 3.4. In the figure, k_{iT} is the reciprocal of k_{Ti} , and $G_{rls}(s) = \frac{1}{R_s + sL_{dq}}$, signifying the generator's resistance and inductance.

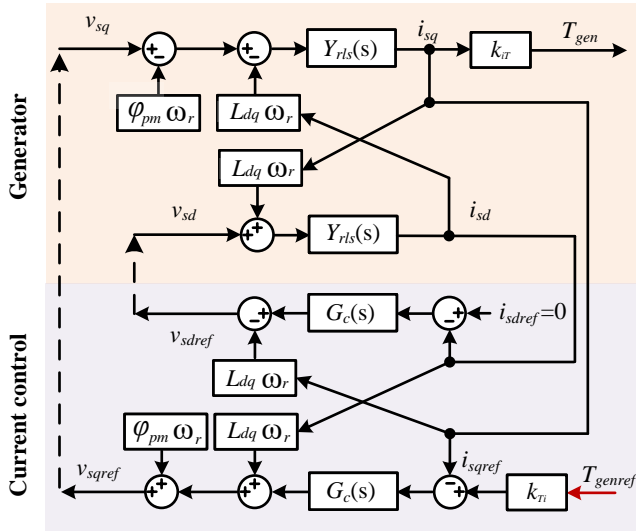


Figure 3.4: Block diagram of the MSC inner control loop and generator model in the dq frame.

Considering that the control delay ranges from tens to hundreds of microseconds, $v_{sd} \approx v_{sdrref}$ and $v_{sq} \approx v_{sqref}$, the system model is simplified for torsional dynamics analysis within the GFM-MWT framework [22]. This simplification leads to a manageable representation of the combined dynamics of the inner loop and the ideal PMSG [65].

3.3. Small-signal modeling of electromechanical dynamics of GFM-MWTs

The resulting dynamics, particularly relevant to the generated torque, are depicted as:

$$\frac{T_{gen}}{T_{genref}} = \frac{i_{sq}}{i_{sqref}} = \frac{G_c(s)G_{rls}(s)}{1 + G_c(s)G_{rls}(s)} = \frac{1}{\frac{1}{\omega_c}s +} \quad (3.5)$$

where ω_c , chosen between 500 and 2000 rad/s, results in that $T_{gen} \approx T_{genref}$ for the operational range.

Thus, the reduced-order model of the MSC is given by

$$T_{gen} = G_{dc}(s)(v_{dc}^2 - v_{dc}^2) \quad (3.6)$$

Further, the small-signal representations of \hat{P}_{gen} , \hat{T}_{gen} and \hat{v}_{dc}^2 are expressed as

$$\begin{aligned} \hat{P}_{gen} &= T_{gen0}\hat{\omega}_r + \omega_{r0}\hat{T}_{gen} \\ \hat{T}_{gen} &= \frac{-P_{gen0}}{\omega_{r0}^2}\hat{\omega}_r + \frac{\hat{P}_{gen}}{\omega_{r0}} \\ \hat{v}_{dc}^2 &= \frac{2(\hat{P}_{gen} - \hat{P}_o)}{sC_{dc}} \end{aligned} \quad (3.7)$$

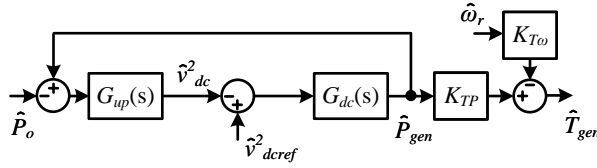


Figure 3.5: Reduced-order small-signal model of MSC.

The small-signal representation of T_{gen} is elucidated by

$$\hat{T}_{gen} = K_{TP} \frac{G_{dc}(s)G_{up}(s)}{1 + G_{dc}(s)G_{up}(s)} \hat{P}_o - K_{T\omega}\hat{\omega}_r \quad (3.8)$$

where

$$\begin{aligned} K_{T\omega} &= \frac{P_{gen0}}{\omega_{r0}^2} \\ K_{TP} &= \frac{1}{\omega_{r0}} \\ G_{up}(s) &= \frac{2}{sC_{dc}} \end{aligned} \quad (3.9)$$

Based on (3.8), the reduced-order small-signal model of the MSC can be illustrated by Fig. 3.5.

3.3.2 Small-signal modeling of the GSC

In this work, the dynamic impact of grid phase changes on the torsional oscillation mode of WT is studied. Thus, a linearized small-signal model of the GSC that captures the dynamics of phase adjustments in response to grid perturbations and control actions is given as detailed below

$$\hat{\theta} = \frac{1}{s} [\hat{\omega}_g - K_p \hat{P}_o + \frac{1}{2Hs} (\hat{P}_{ref} - \hat{P}_o)] \quad (3.10)$$

where $\hat{\theta}$ represents the small-signal variation in the control angle, $\hat{\omega}_g$ is the change in grid phase.

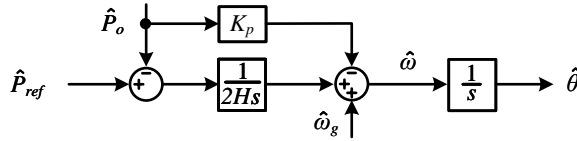


Figure 3.6: Small-signal model of the GSC

Fig. 3.6 visualizes this small-signal model, providing a schematic representation of the GSC. This model is important in understanding the grid-side dynamics and their interaction with the GFM-MWT system, particularly in the context of torsional vibrations.

3.3.3 Small-signal modeling of wind turbine mechanics

In analyzing the mechanical dynamics of WTs, we consider a configuration featuring three-pitch blades mounted on the rotor and a two-mass drivetrain system. This choice of a two-mass drive train model is primarily driven by its balance between simplicity and accuracy in capturing the torsional dynamics of the drive train and integrating it with the electronic system [66]. The wind turbine is operated based on the MPPT and pitch angle control systems, which optimize the energy capture efficiency and adjust the blade orientation in response to wind conditions.

The wind turbine is configured with three-pitch blades affixed to the rotor accompanied by a two-mass drive train, which is widely utilized in the analysis of torsional vibrations [22]. The control mechanisms of the turbine include the MPPT [3] and the pitch angle control.

The mechanical power output of the wind turbine (P_{tur}) and the generated torque (T_{tur}) are critical parameters that can be calculated through the

3.3. Small-signal modeling of electromechanical dynamics of GFM-MWTs

aerodynamic relationships,

$$T_{tur} = \frac{1}{2}\rho\pi R^3 C_t(\lambda, \beta) v_w^2 \quad (3.11)$$

$$P_{tur} = \frac{1}{2}\rho\pi R^2 C_p v_w^3 \quad (3.12)$$

where ρ represents the air density, R is the turbine blade radius, v_w denotes the wind speed, and C_t and C_p are the torque and power coefficients, respectively. These coefficients depend on the tip speed ratio (λ) and the pitch angle (β), essential for capturing the turbine operational dynamics. The expressions for $C_t(\lambda, \beta)$ and $C_p(\lambda, \beta)$ is given by

$$\begin{aligned} C_t(\lambda, \beta) &= \frac{C_p(\lambda, \beta)}{\lambda} \\ C_p(\lambda, \beta) &= a_1 \left(\frac{a_2}{\lambda} - a_3 \beta - a_4 \beta^5 - a_6 \right) e^{-\frac{a_7}{\lambda}} \end{aligned} \quad (3.13)$$

where $\lambda = \frac{\omega_t R}{v_w}$, with ω_t denoting the turbine rotational speed.

For the purposes of small-signal analysis, (3.11) are linearized

$$\hat{T}_{tur} = K_{tur} \hat{\omega}_t \quad (3.14)$$

where K_{tur} represents the sensitivity of the turbine torque to changes in the turbine rotational speed at a specific operational point (op), dictated by the wind speed v_{w0} , given by

$$K_{tur} = \frac{dT_{tur}}{d\omega_t}_{op} = \frac{1}{2}\rho\pi R^3 v_{w0}^2 \frac{dC_t(\lambda, \beta)}{d\lambda}_{op} \quad (3.15)$$

We assume a constant wind speed within the MPPT domain in this work. This assumption allows us to align the extracted active power with the optimal power curve, calculated as,

$$P_{ref} = \frac{1}{2}\rho\pi R^2 C_{opt} \frac{\omega_r^3 R^3}{\lambda_{opt}^3} \quad (3.16)$$

where C_{opt} denotes the optimal power coefficient, and λ_{opt} signifies the optimal tip speed ratio. Linearizing this expression yields

$$\hat{P}_{ref} = K_m \hat{\omega}_r \quad (3.17)$$

where

$$K_m = \frac{dP_{ref}}{d\omega_r}_{op} = \frac{3}{2}\rho\pi R^2 C_{opt} \frac{\omega_{r0}^2 R^3}{\lambda_{opt}^3} \quad (3.18)$$

The mechanical system, featuring a two-mass drivetrain model, helps with a closer examination of torsional vibrations. The motion equations of the drivetrain are described as:

$$\begin{aligned}
 T_{tur} - T_{shaft} &= 2H_{wt}s\omega_t \\
 T_{shaft} - T_{gen} &= 2H_g s\omega_r \\
 T_{shaft} &= (d_s + \frac{k_s}{s})(\omega_t - \omega_r)
 \end{aligned} \tag{3.19}$$

with H_{wt} and H_g denoting the inertia constants of the turbine and generator, respectively. The damping and stiffness coefficients of the shaft are represented by k_s and d_s , respectively [67].

Linearizing the drivetrain equations offers a clearer view of the system response to small perturbations

$$\begin{aligned}
 \hat{T}_{tur} - \hat{T}_{shaft} &= 2H_{wt}s\hat{\omega}_t \\
 \hat{T}_{shaft} - \hat{T}_{gen} &= 2H_g s\hat{\omega}_r \\
 \hat{T}_{shaft} &= (d_s + \frac{k_s}{s})(\hat{\omega}_t - \hat{\omega}_r) \\
 \hat{T}_{tur} &= K_{tur}\hat{\omega}_t
 \end{aligned} \tag{3.20}$$

(3.20) can be further simplified by introducing

$$\begin{aligned}
 A_m &= \frac{1}{2H_{wt}s} \\
 A_g &= \frac{1}{2H_g s} \\
 A_s &= d_s + \frac{k_s}{s} \\
 M_{gr}(s) &= A_s \left(\frac{A_m A_s}{1 + A_m A_s - A_m k_{tur}} - 1 \right)
 \end{aligned} \tag{3.21}$$

The transfer function from \hat{T}_{gen} to $\hat{\omega}_r$ is thus represented as

$$\hat{\omega}_r = \frac{A_g}{A_g M_{gr}(s) - 1} \hat{T}_{gen} \tag{3.22}$$

According to 3.22, the small-signal representation of the turbine is illustrated in Fig. 3.7.

3.3.4 Small-signal modeling of GFM-MWT system

Based on the quasi-static equation, the behavior of \hat{P}_o can be linked with the small-signal variation in the phase angle of the grid, expressed as

$$\hat{P}_o = K_{\theta P}(\hat{\theta} - \hat{\theta}_g) \tag{3.23}$$

3.3. Small-signal modeling of electromechanical dynamics of GFM-MWTs

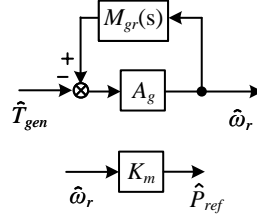


Figure 3.7: Electromechanical small-signal model of the turbine

where $K_{\theta P} = \frac{V_{g0}V_{o0}}{X}$, with V_{g0} and V_{o0} denoting the grid voltage and the output voltage. X represents the line reactance between the GSC and the grid.

Combining the detailed expressions of the MSC, GSC, with WT mechanics, we obtain the small-signal model for the GFM-MWT system. This complete model is visually represented in Fig. 3.8, showing the interplay between mechanical and electrical dynamics within the system. The closed-loop transfer function between small-signal variations in the grid phase angle ($\hat{\theta}_g$) and the rotor speed ($\hat{\omega}_r$) is described as

$$\hat{\omega}_r = H_{P\omega} \frac{K_{\theta P}}{K_{\theta P} H_{\theta P} - 1} \hat{\theta}_g \quad (3.24)$$

where

$$H_{P\omega} = K_{TP} \frac{A_g}{A_g(M_{gr}(s) + K_{T\omega}) - 1} \frac{G_{dc}(s)G_{up}(s)}{1 + G_{dc}(s)G_{up}(s)} \quad (3.25)$$

$$H_{\theta P} = \frac{1}{s} \left(\frac{1}{2HS} (K_m H_{P\omega} - 1) - K_p \right)$$

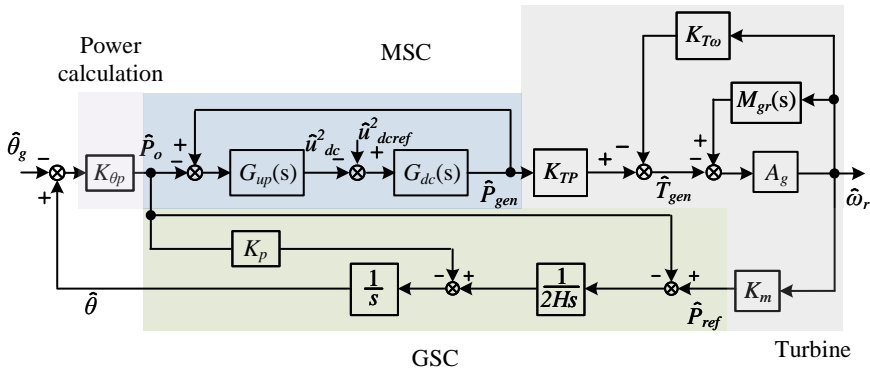


Figure 3.8: Electromechanical small-signal model of the GFM-WT system

Based on the developed small-signal model of the GFM-MWT, the eigenvalue analysis will be implemented in Chapter. 3.5 to reveal the torsional

dynamics of the GFM-MWT under the grid phase angle change events.

3.4 Torsional Modal Analysis

This section focuses on the torsional modal analysis of the GFM-MWT. We begin by examining the drivetrain model to derive the general expressions for the natural frequency (ω_n), damping ratio (ζ), and damped frequency (ω_d). Subsequently, applying the complex torque coefficient method to the developed small-signal models, we can calculate ω_n , ζ , and ω_d for the GFM-MWT setup to analyze the impact of GFM control on torsional modes.

3.4.1 The 2-mass drive train

The exploration starts with analyzing the 2-mass drivetrain system to obtain the natural frequency and damping ratio of the first-degree vibration. Under the assumption of no external torques, meaning $T_{tur} = T_{gen} = 0$, and transforming the motion equation to incorporate angular velocity as $\omega = s\theta$, we reformulate the small-signal motion equation as

$$\begin{aligned} 2H_{wt} \frac{d^2 \hat{\theta}_t}{dt^2} + d_s \left(\frac{d \hat{\theta}_t}{dt} - \frac{d \hat{\theta}_r}{dt} \right) + k_s (\hat{\theta}_t - \hat{\theta}_r) &= \hat{T}_{tur} = 0 \\ 2H_g \frac{d^2 \hat{\theta}_r}{dt^2} - d_s \left(\frac{d \hat{\theta}_t}{dt} - \frac{d \hat{\theta}_r}{dt} \right) - k_s (\hat{\theta}_t - \hat{\theta}_r) &= -\hat{T}_{gen} = 0 \end{aligned} \quad (3.26)$$

This system is a Single-Degree-of-Freedom (SDOF) model, characterized by its natural frequency, damping ratio, and damped frequency, given by

$$\begin{aligned} \omega_n &= \pm \sqrt{\frac{k_s(H_{wt} + H_g)}{2H_{wt}H_g}} \\ \zeta &= \frac{d_s(H_{wt} + H_g)}{4H_{wt}H_g\omega_n} \\ \omega_d &= \omega_n \sqrt{1 - \zeta^2} \end{aligned} \quad (3.27)$$

Utilizing the parameters outlined in Table. 3.1, the calculated values for ω_n , ζ , and ω_d within the context of the 2-mass drivetrain system are determined to be 2.5060 Hz, 0.0282, and 2.5050 Hz, respectively.

3.4.2 The wind turbine

Integrating the linearized turbine torque equation into the motion equation, we can obtain the new motion equation including the mechanical dynamics of

the wind turbine as

$$\begin{aligned}
 2H_{wt} \frac{d^2 \hat{\theta}_t}{dt^2} + d_s \left(\frac{d\hat{\theta}_t}{dt} - \frac{d\hat{\theta}_r}{dt} \right) + k_s (\hat{\theta}_t - \hat{\theta}_r) &= k_{tur} \frac{d\hat{\theta}_t}{dt} \\
 2H_g \frac{d^2 \hat{\theta}_r}{dt^2} - d_s \left(\frac{d\hat{\theta}_t}{dt} - \frac{d\hat{\theta}_r}{dt} \right) - k_s (\hat{\theta}_t - \hat{\theta}_r) &= -\hat{T}_{gen} = 0
 \end{aligned} \tag{3.28}$$

Through the careful resolution of the above equation, under the approximation that $|k_{tur}| \ll 1$ [22], we derive simplified expressions for the system's natural frequency, damping ratio, and damped frequency as

$$\begin{aligned}
 \omega_{nt} &= \pm \sqrt{\frac{k_s(H_{wt} + H_g)}{2H_{wt}H_g}} \\
 \zeta_t &= \frac{d_s(H_{wt} + H_g) - k_{tur}H_g}{4H_{wt}H_g\omega_n} \\
 \omega_{dt} &= \omega_{nt} \sqrt{1 - \zeta_t^2}
 \end{aligned} \tag{3.29}$$

Based on (3.29), the damping ratio ζ_t can be observed to be marginally higher than ζ , attributable to the inclusion of k_{tur} . The value of k_{tur} is negative within the MPPT zone. Therefore, this increment in damping reveals that the control of the wind turbine enhances stability characteristics under optimal power generation conditions. Consequently, the damped frequency ω_{dt} remains practically unchanged since the natural frequency ω_{nt} is equal to ω_n .

Given the parameters in Table. 3.1, ω_{nt} , ζ_t and ω_{dt} are computed to be 2.5060 Hz, 0.0290, and 2.5050 Hz, respectively.

Utilizing the parameters outlined in Table. 3.1, we calculate the values for ω_{nt} , ζ_t , and ω_{dt} to be 2.5060 Hz, 0.0290, and 2.5050 Hz, respectively. This calculation corroborates the theoretical insights into the influence of k_{tur} on the torsional modes.

3.4.3 Complex torque coefficients method-based torsional modal analysis of GFM-MWT

This subsection explores the torsional modal analysis of the GFM-MWT using the complex torque coefficients method [68]. This approach involves decomposing the generator torque, \hat{T}_{gen} , into components that reflect how torque variations align with rotor angle and speed perturbations

$$\hat{T}_{gen} = W_s(s)\hat{\theta}_r + W_d(s)\hat{\omega}_r \tag{3.30}$$

where $W_s(s)$ denotes the synchronizing coefficient, influencing natural vibration frequencies, and $W_d(s)$ is the damping coefficient, influencing the damping of torsional vibration.

Incorporating the decomposition, as shown in (3.30), into the previously established motion equation, as shown in (3.28), and converting it to the Laplace domain, yields an equation for calculating the torsional modes of the GFM-MWT

$$W_M(s)\hat{\theta}_r = -(W_s(s) + sW_d(s))\hat{\theta}_r \quad (3.31)$$

where

$$W_M(s) = 2H_g s^2 + d_s s + k_s - (d_s s + k_s) \frac{(d_s - k_{tur})s + k_s}{2H_{wt} s^2 + (d_s - k_{tur})s + k_s} \quad (3.32)$$

We can obtain the natural frequency of the GFM-MWT, ω_{nm} , by substituting $s = j\omega$ and equating the real part of $W_M(j\omega)$ with $W_s(\omega)$ as expressed below

$$-W_{MR}(\omega) = W_s(\omega) \quad (3.33)$$

where $W_{MR}(\omega)$ is the real part of $W_M(j\omega)$

$$W_{MR}(\omega) = -2H_g \omega^2 + k_s - \frac{k_s^2}{-2H_{wt} \omega^2 + k_s} \quad (3.34)$$

The damping and synchronizing coefficients are then computed to deduce the damping ratio (ξ_m) and damped frequency (ω_{dm}), with their expressions simplified for clarity [64] given by

$$\xi_m = \frac{d_s(H_{wt} + H_g) - k_{tur}H_g + W_d(\omega_{nm})H_{wt}}{4H_{wt}H_g\omega_n} \quad (3.35)$$

$$\omega_{dm} = \omega_{nm} \sqrt{1 - \xi_m^2}$$

As indicated in Fig. 3.8, a feedback loop exists from $\hat{\omega}_r$ to \hat{T}_{gen} for the GFM-MWT, including the grid impedance, the MSC, the GSC, and the generator, which can be defined as

$$\frac{\hat{T}_{gen}}{\hat{\omega}_r} = G_{pt}^a \left(\frac{K_{\theta p} K_m}{K_{\theta p} + 2K_{\theta p} K_p H s + 2H s^2} - K_{P\omega} \right) \quad (3.36)$$

$$G_{pt}^a = \frac{G_{dc}(s)G_{up}(s)}{1 + G_{dc}(s)G_{up}(s)K_{PT}}$$

According to (3.36) and 3.34, Fig. 3.9 illustrates the obtained $W_s(\omega)$, $W_d(\omega)$, and $-W_{MR}(\omega)$, revealing a critical insight: the GFM-MWT control system introduces negative damping to the system's torsional dynamics since $W_d(\omega_{nm})$ is predominantly governed by $-K_T\omega$. Additionally, $\omega_{nm} \approx \omega_{ng}$.

The torsional mode's damped frequency and damping ratio for the GFM-MWT are visually presented in Fig. 3.10 by utilizing the parameters detailed in Table 3.1. It is observed that the damped frequency remains around 2.5 Hz and the wind turbine exhibits the highest damping ratio, followed by the 2-mass drive train, with the GFM-MWT setup showing the lowest.

3.5. Eigenvalue and complex torque coefficients method-based torsional modal analysis

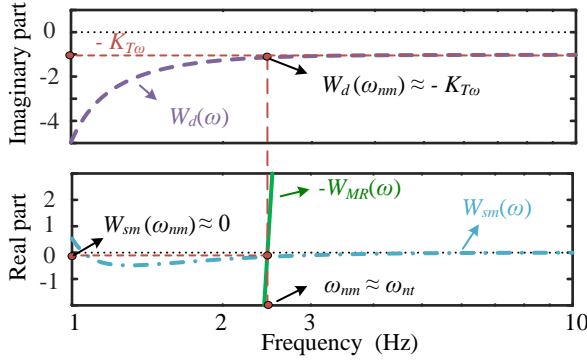


Figure 3.9: W_s and W_d of the GFM-MWT and $-W_{MR}$.

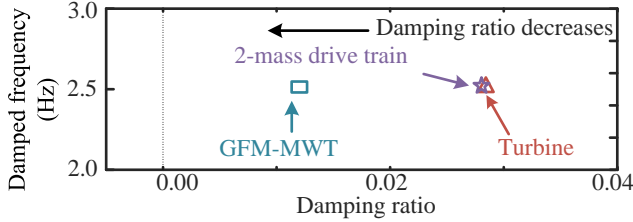


Figure 3.10: Damped frequency and damping ratio for the 2-mass drive train, turbine, and the GFM-MWT

3.5 Eigenvalue and complex torque coefficients method-based torsional modal analysis

As illustrated in Fig. 3.8, perturbation in the grid-side phase angle, $\hat{\theta}_g$, causes direct fluctuations in the output power, \hat{P}_o . These changes prompt adjustments in the generator power, \hat{P}_{gen} , through the DVC of the MSC. The resultant modifications in \hat{P}_{gen} incite torsional vibrations within the two-mass drivetrain, which subsequently affect the power reference, \hat{P}_{ref} . Since the GSC is synchronized via active power control, these mechanical vibrations eventually become power oscillations on the grid side. Moreover, the torsional dynamics of the GFM-MWT are influenced by both control settings and system parameters.

Using the developed small-signal model and derived torsional modes (see (3.24) and (3.35)), torsional dynamics can be thoroughly analyzed through both eigenvalue and torsional modal analysis methods. To compare these methods and validate the torsional model analysis, the damping ratio, ζ_m , and the damped frequency, ω_{dm} , are calculated based on the real and imaginary

parts of the system poles

$$\omega_{nm} = \sqrt{\alpha^2 + \beta^2} \quad (3.37)$$

$$\tilde{\zeta}_m = \frac{\alpha}{\omega_n} \quad (3.38)$$

$$\omega_{dm} = \beta \quad (3.39)$$

where

$$\alpha = -\text{real}(\text{pole}) \quad (3.40)$$

$$\beta = \text{imag}(\text{pole}) \quad (3.41)$$

Using parameters from Table 3.1, the values of $\tilde{\zeta}_m$ and ω_{dm} from both the eigenvalue analysis and the complex torque coefficients method are depicted in Figs. 3.11 - 3.14, under various system and control parameter settings. It is evident that the torsional modes from both analyses align, indicating consistent findings across methodologies. Additionally, by examining Figs. 3.11 - 3.14 and comparing them to Fig. 3.10, it is clear that the overall control strategy of the GFM-MWT reduces the damping ratio for the torsional mode of the wind turbine, which aligns with our observation based on (3.36).

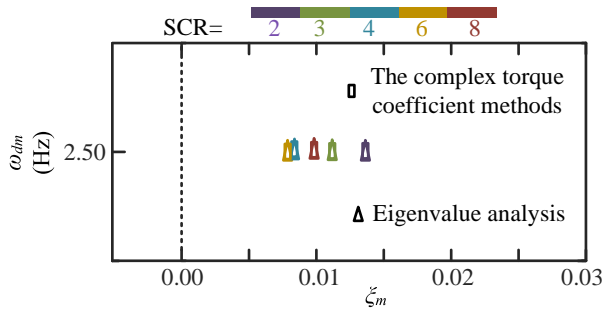


Figure 3.11: Damped frequency and damping ratio of the GFM-MWT under varying SCR

As shown in Fig. 3.11, the damping ratio of the torsional modes exhibits an initial decrease followed by an increase as SCR escalates, reaching the lowest damping ratio at SCRs of 6 and 10 for the GFM-MWT setup.

Regarding dc system parameters, Fig. 3.12 explicitly shows that an increase in the capacity of the dc-link capacitor enhances the damping ratio, acting as an energy buffer that supplies additional instantaneous power when needed.

Moreover, Fig. 3.13 illustrates that a rise in the GFM control parameter H correlates with an increase in the damping ratio, while a negative damping ratio is observed when $H = 2$.

3.5. Eigenvalue and complex torque coefficients method-based torsional modal analysis

Table 3.1: Parameters of the GFM-MWT system [3]

Rated active power P_{ref}	5 MW
Grid voltage V_g	690 V
Filter inductance L_f	0.15 p.u.
Filter resistance R_f	0.005 p.u.
Grid inductance L_g	0.25 p.u.
Grid resistance R_g	0.02 p.u.
Active power control parameters K_p, H	0.0104, 3
Reactive power control parameter K_q	0.001
dc-link voltage control parameters K_{pdc}, K_{idc}	0.78, 0.85
dc-link voltage v_{dc}	1500 V
Grid frequency f_g	50 Hz
Rated turbine rotational speed ω_t	1.27 rad/s
Rated wind speed	11.487 m/s
Operational wind speed v_{w0}	10 m/s
Rotor Radius R	63 m
Optimal power coefficient C_{opt}	0.44
Optimal tip speed ratio λ_{opt}	7
Stiffness of the shaft k_s	280.00 p.u.
Damping coefficient of the shaft d_s	1.00 p.u.
Inertia constants of the turbine H_{wt}	1.93 s
Inertia constants of the generator H_g	0.8 s
Stator inductor L_{dq}	4 mH
Parasitic resistance of stator inductor R_s	2.45 m Ω
Magnetic flux ψ_m	5.84 Wb.
Switching frequency	5000 Hz
DC capacitor	0.3 F
Short Circuit Ratio (SCR)	4

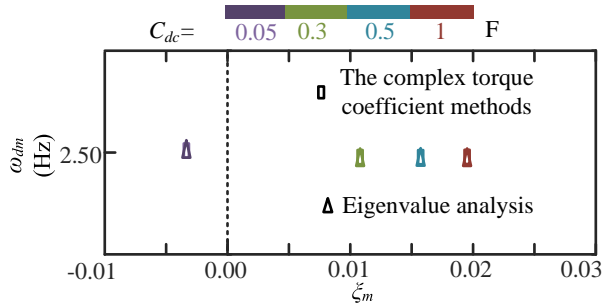


Figure 3.12: Damped frequency and damping ratio of the GFM-MWT under varying C_{dc} when SCR=3

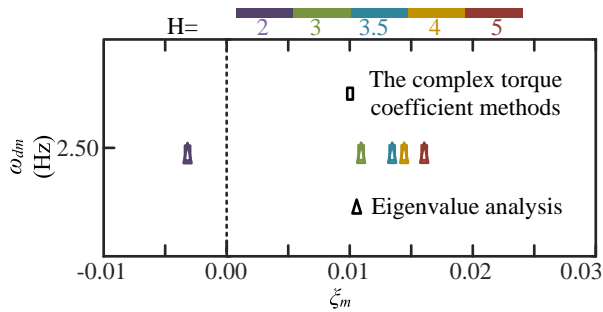


Figure 3.13: Damped frequency and damping ratio of the GFM-MWT under varying H when SCR=3

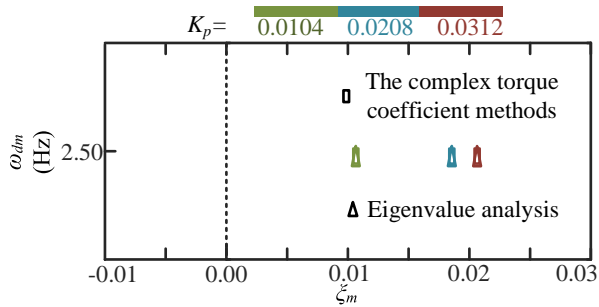


Figure 3.14: Damped frequency and damping ratio of the GFM-MWT under varying K_p when SCR=3

In terms of other GFM control parameters such as K_p , depicted in Fig. 3.14, it is evident that an increase in K_p also improves the damping ratio for the torsional mode within GFM-MWT configurations.

3.6 Simulation results

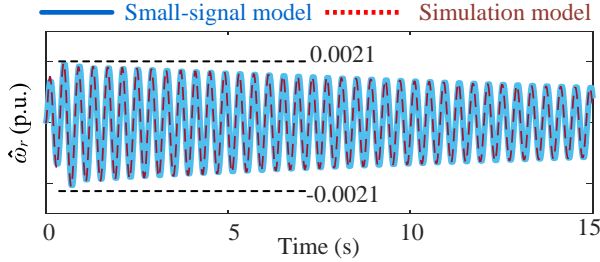


Figure 3.15: Comparison of simulation results and small-signal models for disturbance response of ω_r with 2° step disturbance adding to θ_g under steady state.

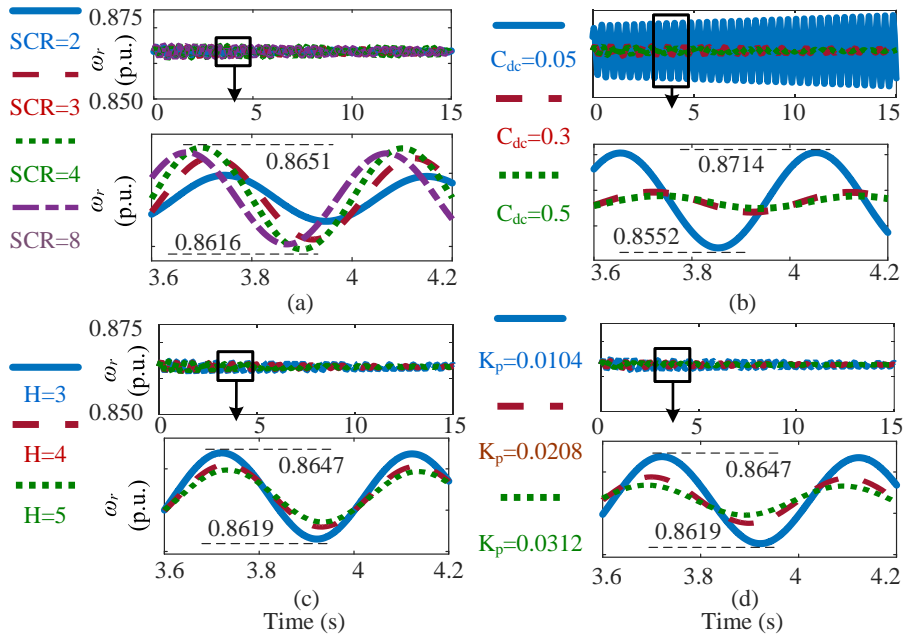


Figure 3.16: Disturbance response of ω_r for the GFM-MWT with 2° step disturbance adding to θ_g under varied control and system parameters. (a) Changing SCR. (b) Changing C_{dc} . (c) Changing control parameter H . (d) Changing control parameter K_p .

To substantiate the accuracy of the small-signal model for the GFM-MWT in analyzing torsional vibrations induced by changes in θ_g , nonlinear time-domain simulations are conducted using MATLAB/Simulink and the PLECS blockset. These simulations employ the detailed system model depicted in

Fig. 2.1, with parameters sourced from Table 3.1.

The validation process involves comparing the simulated response of ω_r to a 2° step disturbance applied to θ_g under steady-state conditions, against predictions made by the small-signal model. The results, showcased in Fig. 3.15, demonstrate a maximum error of approximately $1.05e^{-4}$ p.u., confirming the model accuracy.

Additional simulations assess the response of ω_r to the same 2° step disturbance across various control and system parameter settings, as illustrated in Fig. 3.16. These results further validate the insights previously discussed and graphically represented in Fig. 3.11 - 3.14.

As detailed in Fig. 3.16 (a), an increase in SCR initially reduces and then increases the amplitudes of torsional vibrations of ω_r , which indicates that the damping ratio of torsional vibrations is enhanced and then diminished, corroborating the trends observed in Fig. 3.11. Regarding the dc-link capacitor (C_{dc}), Fig. 3.16(b) confirms that a higher C_{dc} value enhances the damping ratio for the GFM-MWT, effectively damping torsional vibrations by providing additional instantaneous power to the load as required.

Concerning control parameters, enhancements in the GFM control parameter H are expected to increase the damping of torsional vibrations following disturbances, as predicted and supported by the results in Fig. 3.16(c).

Lastly, Fig. 3.16(d) illustrates that a rise in the proportional gain, K_p , typically leads to a reduction in the amplitudes of torsional vibrations.

In conclusion, the grid-side dynamics can indeed trigger torsional dynamics within the GFM-MWT system. These oscillations not only potentially reduce the lifespan of the converters but might also pose stability challenges, as evidenced by the solid blue line in Fig. 3.16(b).

3.7 Summary

This chapter delves into the electromechanical dynamics of the GFM-MWT, with a special emphasis on torsional vibrations induced by grid-phase changes. A comprehensive analysis of the small-signal model of the GFM-MWT has been conducted to explore these dynamics.

1. **Development of Reduced-Order Small-Signal Model:** A reduced-order small-signal model of the GFM-MWT is constructed, incorporating key turbine components such as the drivetrain and turbine control systems. This model elucidates the direct link between mechanical dynamics and grid phase changes, demonstrating how changes in grid phase can trigger oscillatory modes within the drivetrain that result in power oscillations on the grid side.

3.7. Summary

2. **Analytical Insights via Complex Torque Coefficients Method:** Moving beyond the reliance on numerical simulations found in previous studies, this chapter employs the complex torque coefficients method to derive mathematical expressions for the torsional modes of the GFM-MWT. By examining the torsional modes, this analysis offers fundamental insights and concludes that the GFM-MWT control introduces a negative damping effect on torsional dynamics.
3. **Evaluation through Eigenvalue and Modal Analyses:** To validate the effectiveness of the proposed modeling approach, eigenvalue analysis and complex torque coefficients method-based analysis are implemented and their results are compared. These analyses highlight the sensitivity of damping ratios to various system and control parameters, such as SCR, dc-link capacitor capacity (C_{dc}), inertia constant (H), and proportional gain (K_p). The accuracy of these findings is further corroborated through nonlinear time-domain simulations, confirming the accuracy of theoretical models.

Overall, this chapter advances the understanding of the impact of grid-phase changes on the torsional dynamics of GFM-MWTs, providing valuable insights into system behavior and aiding in the design of control parameters to enhance system stability and performance.

Chapter 4

Impacts of different control strategies on electromechanical dynamics of GFM-WTs

4.1 Background

The chapter 3 characterizes torsional modes of the GFM-MWT by utilizing the complex torque coefficients method in combination with the reduced-order small-signal model of GFM-MWTs. However, the analysis is limited to a specific control method for the GFM-MWT, leaving the impact of diverse converter control strategies on torsional dynamics unexplored [69].

This chapter aims to comprehensively examine how different converter controls affect the torsional modes of GFM-WTs. Specifically, the comparison between GFM-GWT and GFM-MWT in terms of their impacts on torsional dynamics is performed first. Using the complex torque coefficients method, we derive precise mathematical expressions for damping ratios and damped frequencies for both GFM-GWT and GFM-MWT. It is indicated that placing the DVC within the MSC introduces a negative damping effect on the torsional dynamics of the WT [52]. To delve deeper into the influence of the DVC, the impacts of three different DVC schemes within the MSC on the damping ratios of the torsional dynamics of GFM-MWT are further compared.

Additionally, the chapter investigates how all relevant control and system parameters would affect the damping ratio and damped frequency of torsional modes. This is achieved through the utilization of FNN-based PDA.

The findings are summarized below:

- The GFM-MWT tends to reduce the damping ratio of torsional modes of WT, potentially impairing the system stability. In contrast, the GFM-GWT appears to enhance the damping ratio, dampening torsional oscillations.
- The analysis based on the FNN-based PDA indicates that the damped frequency of torsional modes for both configurations is primarily determined by mechanical design factors, rather than by variations in control parameters.
- Concerning the specific impacts of DVC within the MSC for GFM-MWT, it is found that the type *a* DVC, which doesn't have a feedback loop from the GSC and the turbine, minimizes negative damping effects, maintaining stability across various system parameters.

To confirm the theoretical analysis, non-linear simulation results are presented. These findings advance our understanding of how torsional dynamics interact with GFM-WT integration into the grid.

4.2 Comparative analysis of the GFM-GWT and GFM-MWT on torsional dynamics

As introduced in Chapter. 1, GFM-WTs can be implemented with two distinct configurations related to DVC:

- **GFM-GWT:** In this configuration, the GSC regulates the dc-link voltage. The control setup for this configuration is illustrated in Fig. 4.1.
- **GFM-MWT:** Conversely, in the GFM-MWT setup, the MSC is responsible for controlling the dc-link voltage. This configuration is detailed in Fig. 2.1.

The control structures for the MSC and GSC in the GFM-MWT have been previously discussed in Chapter 3. The control structures for the MSC and GSC in the GFM-GWT configuration will be detailed in subsequent sections. This section aims to explore the impacts of these two configurations on torsional dynamics.

System description of GFM-GWT

The control architecture for the MSC in the GFM-GWT is illustrated in Fig. 4.2, adopted from [14]. This setup includes an active power control as the primary outer loop and a current control loop as the inner mechanism. The

4.2. Comparative analysis of the GFM-GWT and GFM-MWT on torsional dynamics

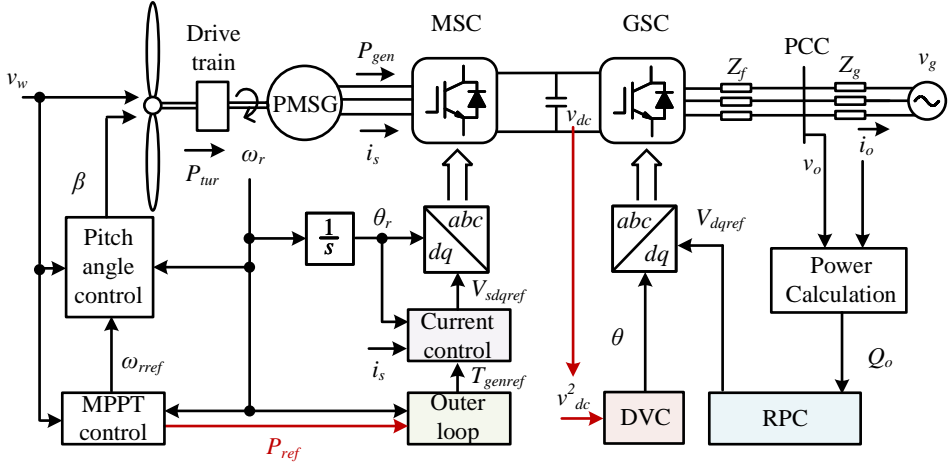


Figure 4.1: The GFM-GWT configuration.

outer loop of the MSC in GFM-GWT primarily targets MPPT, and it dictates the reference torque of PMSG, T_{genref} , by the equation

$$T_{genref} = \frac{P_{ref}}{\omega_r} \quad (4.1)$$

where the power reference, P_{ref} , is derived from the wind speed, v_w , and the rotor speed, ω_r , based on the optimal power curve [3].

The current control loop of the MSC in GFM-GWT is the same as that in the GFM-MWT setup. The GSC control strategy for the GFM-GWT, shown in Fig. 4.3, incorporates a DVC and an RPC, similar to those employed in the GFM-MWT [10]. According to [70], the DVC utilizes v_{dc}^2 as the control variable. The dynamic response of the dc-link voltage to transient power fluctuations is utilized to modulate the ac output angle, which is formulated as

$$\theta = \frac{1}{s} [\omega_g + G_{dc}(s)(v_{dc}^2 - v_{dc}^2_{ref})] \quad (4.2)$$

This control scheme is designed to effectively manage the dc-link voltage and contribute to the stability and efficiency of power conversion [71].

4.2.1 Reduced-order small-signal model of the GFM-GWT

Building on the foundation set in Chapter 3, it is rational to approximate that $T_{gen} \approx T_{genref}$ for a simplified examination of the electromechanical dynamics of GFM-WTs.

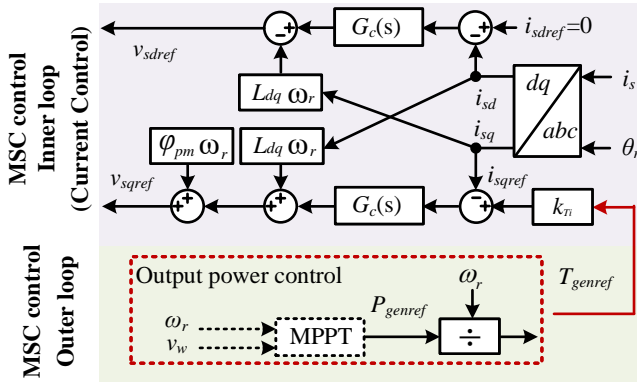


Figure 4.2: Control block diagram of MSC for the GFM-GWT.

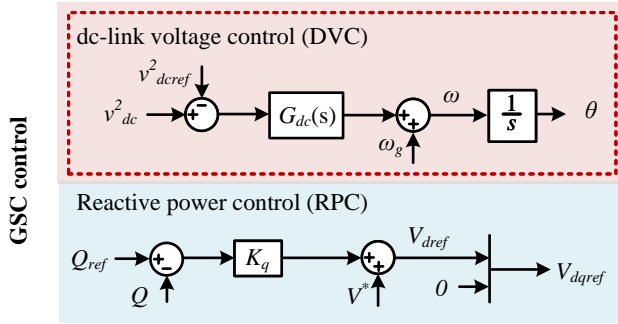


Figure 4.3: Control block diagram of GSC for the GFM-GWT.

From the linearization of (4.1), we derive

$$\hat{T}_{genref} = -K_{T\omega}\hat{\omega}_r + K_{TP}\hat{P}_{ref} \quad (4.3)$$

The small-signal expression for \hat{T}_{genref} is then

$$\begin{aligned} \hat{T}_{genref} &= (-K_{T\omega} + K_{TP}K_m)\hat{\omega}_r \\ &= \rho\pi R^2 C_{opt} \frac{\omega_{r0} R^3}{\lambda_{opt}^3} \hat{\omega}_r \end{aligned} \quad (4.4)$$

Assuming a constant voltage magnitude for simplicity, as cited in [41], the linearized small-signal model of the GSC, derived from (4.5), is

$$\hat{\theta} = \frac{1}{s} [\hat{\omega}_g + G_{dc}(s)(\hat{\nu}_{dc}^2 - \hat{\nu}_{dc}^2_{dcref})] \quad (4.5)$$

Integrating the small-signal models of the MSC, GSC, and turbine, the complete small-signal model of the GFM-GWT are depicted in Fig. 4.4 (a). For

4.2. Comparative analysis of the GFM-GWT and GFM-MWT on torsional dynamics

comparative analysis, the small-signal model of the GFM-MWT is illustrated in Fig. 4.4 (b), where the 'Drive train' block represents the drive train dynamics.

Fig. 4.4 (a) demonstrates that in the GFM-GWT, the turbine and MSC function collectively as a power supply unit, and abrupt grid changes do not trigger torsional vibrations within the drivetrain. However, there exists a feedback loop from $\hat{\omega}_r$ to \hat{T}_{gen} in the GFM-GWT, encompassing the generator control, which might influence the torsional modes of the wind turbine [18]. The corresponding transfer function for this feedback loop is detailed in (4.4).

Conversely, the GFM-MWT configuration, as shown in Fig. 4.4 (b), clearly illustrates the presence of a feedback loop from $\hat{\omega}_r$ to \hat{T}_{gen} that includes the grid impedance, MSC, GSC, generator, and generator control, indicating a more complex interaction affecting torsional dynamics.

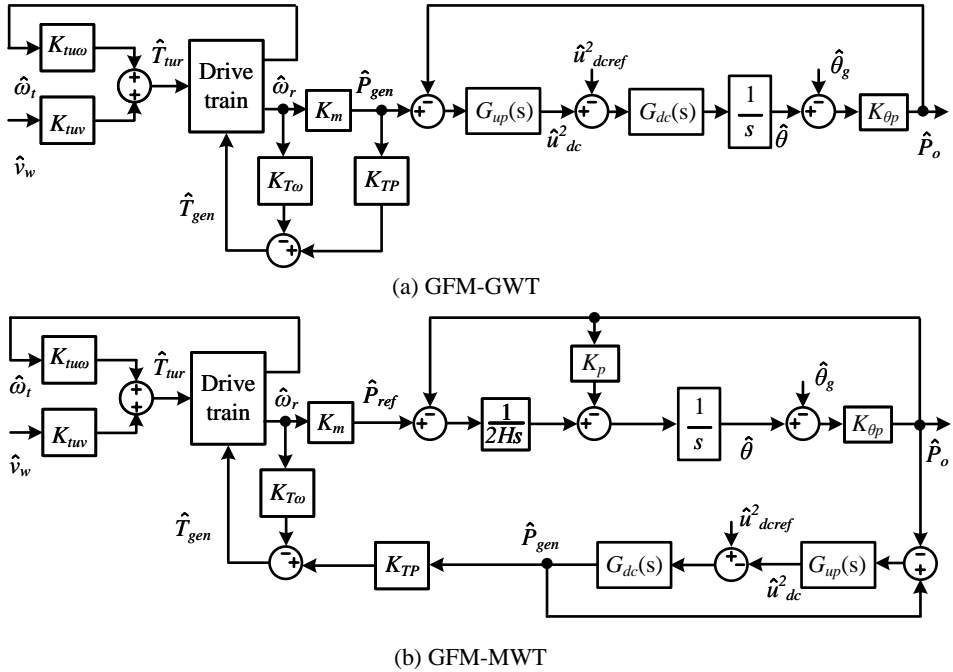


Figure 4.4: Small-signal models of (a) The GFM-GWT. (b) The GFM-MWT.

4.2.2 Torsional modal analysis of GFM-GWT

Building upon the analysis method presented in Chapter 3, the torsional modes of the GFM-GWT are examined using the complex torque coefficients method. By incorporating (4.4) into the equation for complex torque coefficients (3.30), we derive expressions for the synchronizing and damping torque

coefficients of the GFM-GWT, designated as W_{sg} and W_{dg} respectively

$$\begin{aligned} W_{sg} &= 0 \\ W_{dg} &= K_m K_{TP} - K_T \omega \end{aligned} \quad (4.6)$$

where the value W_{dg} is positive constant, according to (4.20).

With $W_{sg}(s) = 0$, the natural frequency of the GFM-GWT's torsional mode, denoted as ω_{ng} , matches that of the GFM-MWT, ω_{nt} . The damping ratio for the GFM-GWT, ζ_g , is calculated as follows

$$\zeta_g = \frac{d_s(H_{wt} + H_g) - k_{tur}H_g + W_{dg}H_{wt}}{4H_{wt}H_g\omega_n} \quad (4.7)$$

indicating that the presence of a positive W_d enhances the damping ratio ζ_g compared to ζ_t , primarily due to the implementation of MPPT control.

This increase in the damping ratio subsequently results in a slight decrease in the damped frequency, denoted ω_{dg} , given by

$$\omega_{dg} = \omega_{ng} \sqrt{1 - \zeta_g^2} \quad (4.8)$$

Since ω_{ng} equals ω_{nt} and ζ_g is predominantly influenced by MPPT control, it becomes evident that the GSC control does not significantly impact the torsional modes of the GFM-GWT. This finding underscores the critical role of converter control strategies in shaping the electromechanical dynamic response and stability of GFM-WT systems.

4.2.3 Validation through Nonlinear Time-Domain Simulations

To verify the torsional modal analysis of the GFM-WT systems, including GFM-GWT and GFM-MWT, under the changes in θ_g and v_w , nonlinear time-domain simulations are conducted using MATLAB/Simulink and the PLECS blockset, based on the detailed system models provided in Fig. 2.1 and Fig. 4.1.

These simulations show the response of rotor speed ω_r to changes in grid-side phase angle and wind speed. The results are compared with predictions from the small-signal models, as depicted in Fig. 4.5 and Fig. 4.6.

Fig. 4.5 demonstrates the nonlinear time-domain simulation results for the disturbance response of ω_r under a 2° step disturbance in θ_g at steady state for both GFM-GWT and GFM-MWT, with maximum errors relative to the small-signal model approximating $1.24e^{-4}$ p.u. for GFM-GWT and $2.75e^{-4}$ p.u. for GFM-MWT.

Similarly, Fig. 4.6 shows the response of ω_r under a 0.4 m/s step increase in wind speed v_w , noting maximum errors of about $1.12e^{-4}$ p.u. for GFM-GWT

4.3. Sensitivity analysis

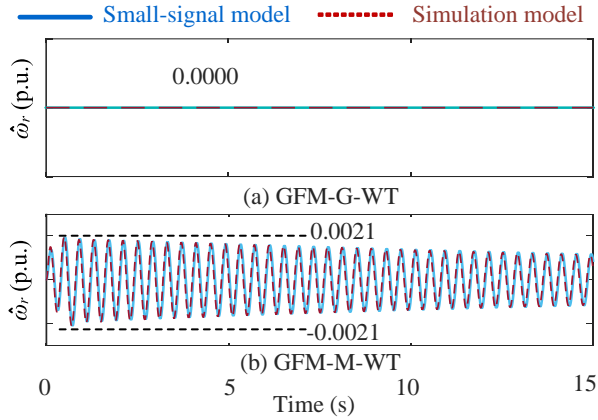


Figure 4.5: Comparison of simulation results and small-signal models for disturbance response of ω_r following a 2° step disturbance to θ_g under steady conditions. (a) GFM-GWT. (b) GFM-MWT.

and $2.50e^{-4}$ p.u. for GFM-MWT. It is noted that GFM-MWT exhibits higher oscillation amplitudes than that of GFM-GWT under the same conditions.

These results confirm that grid-side dynamics can induce torsional dynamics within GFM-MWT but not significantly within GFM-GWT. Conversely, wind speed disturbances cause torsional vibrations in both configurations. However, the control strategy employed by GFM-MWT demonstrates less damping on torsional vibrations than that of GFM-GWT, suggesting different electromechanical dynamic behaviors between the two configurations.

4.3 Sensitivity analysis

The impact of various control and system parameters on the torsional modes of GFM-MWTs and GFM-GWTs, particularly concerning the damped frequency, is not straightforward due to the complex interrelationships contained in the transfer functions, as demonstrated in (4.4) and (3.36). This section is dedicated to performing a detailed nonlinear sensitivity analysis using a FNN-based PDA model. This approach is designed to provide a deeper insight into how specific system and control parameters affect the torsional dynamics of both GFM-GWT and GFM-MWT configurations.

Initially, the FNN model is employed to approximate the computation of damping ratio and damped frequency for both GFM-WT configurations, as depicted in Fig. 4.7. Subsequently, the PDA is applied to this FNN to systematically analyze the sensitivity of the torsional dynamics in the GFM-GWT and GFM-MWT to variations in system and control parameters.

This sensitivity analysis not only aids in understanding on the impacts of individual parameters but also allows for the exploration of their interactive

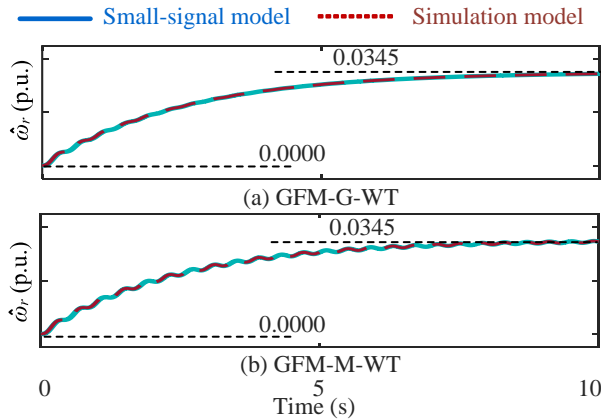


Figure 4.6: Comparison of simulation results and small-signal models for disturbance response of ω_r following a 0.4 m/s step disturbance to v_w under steady conditions. (a) GFM-GWT. (b) GFM-MWT.

effects, providing a comprehensive overview of the torsional dynamic behavior under different controls.

4.3.1 Feedforward Neural Networks for torsional dynamics analysis

As determined in Chapter 3, the damping ratio (ξ_m/ξ_g) and damped frequency (ω_{dm}/ω_{dg}) of the GFM-MWT and GFM-GWT are influenced by a range of control and system parameters. To model these effects, an FNN is employed. The network inputs include 11 selected parameters impacting the torsional dynamics, with damping ratio and damped frequency serving as the outputs y_1 and y_2 , respectively, as detailed in Table 4.1.

Table 4.1: Inputs and outputs of FNN

Inputs	x_1	x_2	x_3	x_4	x_5	x_6	x_7	x_8	x_9	x_{10}	x_{11}
	SCR	H	K_p	k_s	H_g	H_{wt}	C_{dc}	v_w	d_s	k_{pdc}	k_{idc}
Outputs	y_1					y_2					
	ξ_m/ξ_g					ω_{dm}/ω_{dg}					

The FNN architecture, depicted in Fig. 4.7, consists of five hidden layers, each containing 512 neurons. The chosen activation function is the Rectified Linear Unit (ReLU), defined as $f(x) = \max(0, x)$. This function helps to introduce non-linearity into the network without affecting the gradients significantly, which is crucial for learning complex patterns in the data.

4.3. Sensitivity analysis

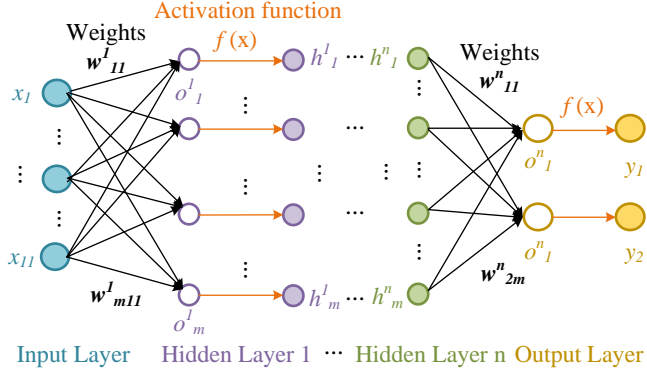


Figure 4.7: Feedforward Neural Network (FNN)

The data flow within the FNN is as follows

$$\begin{aligned}
 h_k^1 &= f(o_k^1), o_k^1 = \sum_{i=1}^{11} w_{k,i}^1 x_i \\
 h_k^n &= f(o_k^n), o_k^n = \sum_{i=1}^m w_{k,i}^n h_i^{n-1} \\
 &\vdots \\
 y_k &= \sum_{i=1}^m w_{k,i}^6 h_i^5
 \end{aligned} \tag{4.9}$$

where x_i and y_i represent the i th input and output variable, respectively. h_k^n denotes the k th neuron in the n th hidden layer. The weights w^{nk}, i link neurons from the $(n - 1)$ th layer to the n th layer, and o_k^n are the weighted sums at the n th layer's k th neuron.

To evaluate the predictive accuracy of the FNN, the Mean Absolute Percentage Error (MAPE) is employed, calculated as

$$MAPE = \frac{100}{N} \sum_{i=1}^N \frac{|a_i - f_i|}{|f_i|} \tag{4.10}$$

where a_i is the actual value derived from the small-signal model and f_i is the FNN prediction.

After training with data derived from the expressions of torsional modes, the FNN achieves a MAPE of 0.01% for the GFM-GWT configuration, and 0.16% for the GFM-MWT configuration, demonstrating high accuracy in capturing the dynamics of torsional modes under different control strategies.

4.3.2 Partial derivative algorithm

The PDA is an established method for conducting sensitivity analysis within neural network frameworks [72]. Once the FNN is well-trained and demonstrates high accuracy, the PDA is applied to examine how small variations in each input parameter affect the outputs. This involves computing the Jacobian matrix, which consists of the partial derivatives of outputs relative to inputs [51], expressed as

$$S_{ki} = \frac{\partial y_k}{\partial x_i} \quad (4.11)$$

To capture a broader perspective, the average sensitivity across the dataset is often calculated to determine the overall impact of each input [51],

$$\bar{S}_{ki} = \frac{1}{N} \sum_{n=1}^N \left| \frac{\partial y_k}{\partial x_i} \right|_N \quad (4.12)$$

where \bar{S}_{ki} denotes the average sensitivity of input x_i on the output y_k , with N representing the total number of data points.

The sensitivity percentage P_{ki} for each input is then derived to rank the influence of each factor on the output y_k ,

$$P_{ki} = \frac{\bar{S}_{ki}}{\sum_{i=1}^{11} \bar{S}_{ki}} \quad (4.13)$$

This metric helps identify the most influential parameters, with the highest P_{ki} values indicating key inputs.

The results of this sensitivity analysis for both the GFM-GWT and GFM-MWT configurations are displayed in Figs. 4.8 and 4.9.

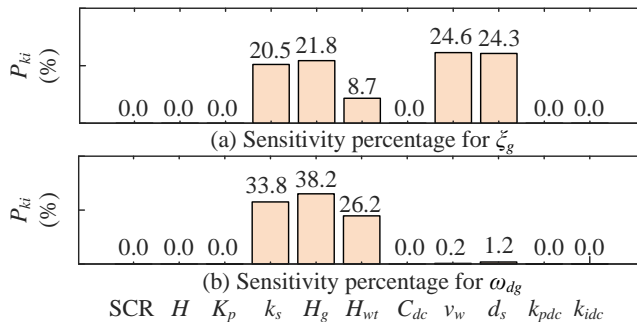


Figure 4.8: Sensitivity analysis of the inputs of the GFM-GWT on (a) damping ratio (b) damped frequency.

4.4. The impact of dc-link voltage control on torsional vibrations within GFM-MWT

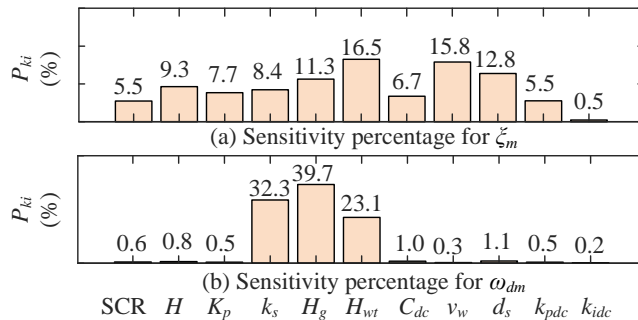


Figure 4.9: Sensitivity analysis of the inputs of the GFM-MWT on (a) damping ratio (b) damped frequency.

For the GFM-GWT, Fig. 4.8 (a) reveals significant sensitivity of the ζ_g to system parameters such as wind speed v_w , shaft damping d_s , generator inertia H_g , shaft stiffness k_s , and turbine inertia H_{wt} , while control parameters exert minimal influence on ζ_g . Meanwhile, Fig. 4.8 (b) shows that the ω_{dg} is predominantly affected by H_g , k_s , and H_{wt} , highlighting the dominance of mechanical component parameters in the torsional modes of GFM-GWT.

Conversely, Fig. 4.9 (a) for the GFM-MWT indicates that ζ_m is highly sensitive to mechanical parameters as well as to several control settings, such as H and K_p , and dc-link capacitor size C_{dc} . The damped frequency ω_{dm} , as shown in Fig. 4.9 (b), continues to be mainly influenced by mechanical parameters. These findings reveal the significant impact of both mechanical and electrical parameters on the damping ratio in GFM-MWTs, while mechanical parameters primarily govern the damped frequency.

4.4 The impact of dc-link voltage control on torsional vibrations within GFM-MWT

4.4.1 System description

As indicated in Section. 4.3, the GFM-MWT control structure introduces a negative damping effect on the torsional dynamics of the WT by placing the DVC within the MSC. To delve deeper into the influence of the DVC, this section evaluates the impacts of 3 commonly used DVC schemes in the MSC on the damping ratios of the torsional dynamics of GFM-MWT. These schemes are differentiated by the output of the PI controller in their respective configurations, as highlighted in the green section of Fig. 4.10

- Generator torque reference, T_{genref} (Type *a*) [39], [37].

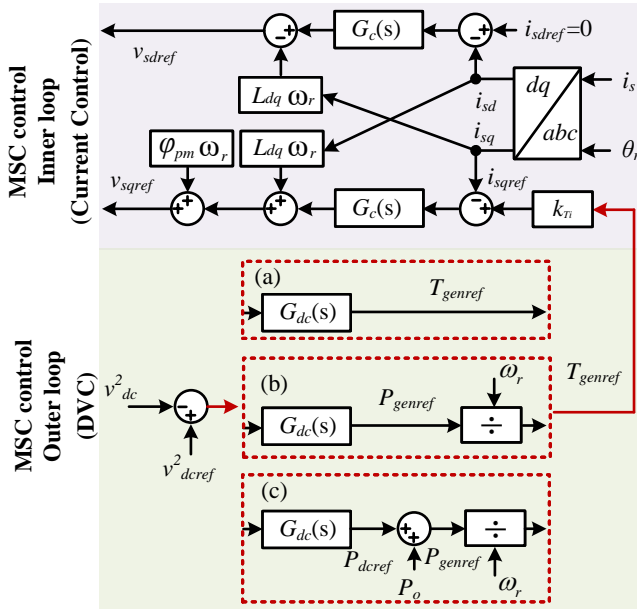


Figure 4.10: Three different MSC control structures for the GFM-MWT

- Generator power reference, P_{genref} (Type *b*) [45], [40], [41].
- DC-link power reference, P_{dcref} (Type *c*) [3], [46].

The corresponding DVC schemes for each type are defined as follows

- Type *a* DVC

$$T_{genref} = G_{dc}(s)(v_{dcref}^2 - v_{dc}^2) \quad (4.14)$$

- Type *b* DVC

$$T_{genref} = \frac{G_{dc}(s)(v_{dcref}^2 - v_{dc}^2)}{\omega_r} \quad (4.15)$$

- Type *c* DVC

$$T_{genref} = \frac{G_{dc}(s)(v_{dcref}^2 - v_{dc}^2) + P_o}{\omega_r} \quad (4.16)$$

Each DVC type is associated with distinct control characteristics within the inner loop of the MSC, detailed in (2.7). The impact of these DVC strategies on GFM-MWTs, classified into three types based on the DVC configuration, will be further explored

4.4. The impact of dc-link voltage control on torsional vibrations within GFM-MWT

- The GFM-MWT using Type *a* DVC, referred to as Type *a* GFM-MWT.
- The GFM-MWT using Type *b* DVC, referred to as Type *b* GFM-MWT.
- The GFM-MWT using Type *c* DVC, referred to as Type *c* GFM-MWT.

4.4.2 Reduced-order small-signal modeling of the MSC under different DVCs

Based on insights from Chapter. 3, it is established that the inner loop of the MSC and generator's electrical dynamics are negligible for analyzing electromechanical interactions [48]. Thus, the reduced-order small-signal representations of T_{gen} for three distinct MSC control types are outlined as follows:

- Type *a* MSC.

$$\hat{T}_{gen} = \frac{G_{dc}(s)G_{up}(s)\hat{P}_o - K_{P\omega}G_{dc}(s)G_{up}(s)\hat{\omega}_r}{1 + G_{dc}(s)G_{up}(s)K_{PT}} \quad (4.17)$$

- Type *b* MSC.

$$\hat{T}_{gen} = K_{TP} \frac{G_{dc}(s)G_{up}(s)}{1 + G_{dc}(s)G_{up}(s)} \hat{P}_o - K_{T\omega} \hat{\omega}_r \quad (4.18)$$

- Type *c* MSC.

$$\hat{T}_{gen} = K_{TP} \hat{P}_o - K_{T\omega} \hat{\omega}_r \quad (4.19)$$

where

$$\begin{aligned} K_{P\omega} &= T_{gen0} \\ K_{PT} &= \omega_{r0} \\ K_{T\omega} &= \frac{P_{gen0}}{\omega_{r0}^2} \\ K_{TP} &= \frac{1}{\omega_{r0}} \\ G_{up}(s) &= \frac{2}{sC_{dc}} \end{aligned} \quad (4.20)$$

Fig. 4.11 visually represents (4.17) - (4.19).

Integrating Fig. 4.11, Fig. 3.6, (3.17), and (3.23), the feedback loops from $\hat{\omega}_r$ to \hat{T}_{gen} for GFM-MWTs under different DVC configurations are illustrated in Fig. 4.12. These models contain the grid impedance, MSC, GSC, and generator dynamics under various control scenarios:

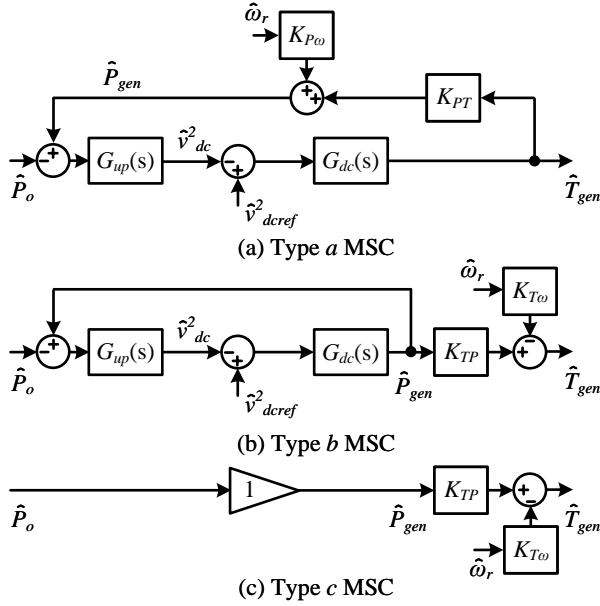


Figure 4.11: Reduced-order small-signal model of (a) Type *a* MSC. (b) Type *b* MSC. (c) Type *c* MSC.

- Type *a* GFM-MWT

$$\frac{\hat{T}_{gen}}{\hat{\omega}_r} = G_{pt}^a \left(\frac{K_{\theta P} K_m}{K_{\theta P} + 2K_{\theta P} K_p Hs + 2Hs^2} - K_{P\omega} \right) \quad (4.21)$$

$$G_{pt}^a = \frac{G_{dc}(s) G_{up}(s)}{1 + G_{dc}(s) G_{up}(s) K_{PT}}$$

- Type *b* GFM-MWT

$$\frac{\hat{T}_{gen}}{\hat{\omega}_r} = G_{pt}^b \left(\frac{K_{\theta P} K_m}{K_{\theta P} + 2K_{\theta P} K_p Hs + 2Hs^2} \right) - K_{T\omega} \quad (4.22)$$

$$G_{pt}^b = \frac{K_{TP} G_{dc}(s) G_{up}(s)}{1 + G_{dc}(s) G_{up}(s)}$$

- Type *c* GFM-MWT

$$\frac{\hat{T}_{gen}}{\hat{\omega}_r} = K_{TP} \left(\frac{K_{\theta P} K_m}{K_{\theta P} + 2K_{\theta P} K_p Hs + 2Hs^2} \right) - K_{T\omega} \quad (4.23)$$

4.4. The impact of dc-link voltage control on torsional vibrations within GFM-MWT

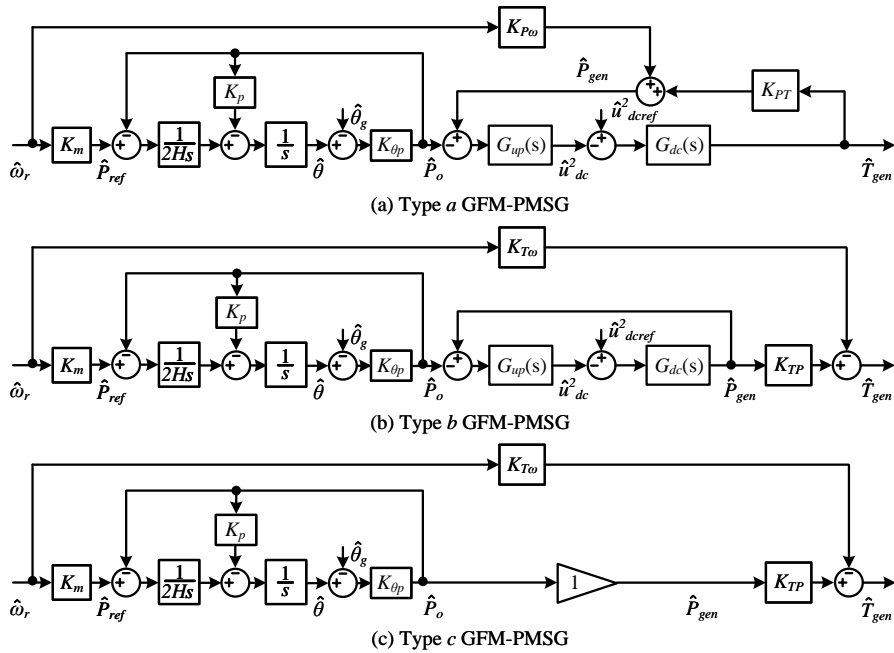


Figure 4.12: Feedback loop from $\hat{\omega}_r$ to \hat{T}_{gen} for the GFM-MWT under different DVCs. (a) Type *a* GFM-MWT. (b) Type *b* GFM-MWT. (c) Type *c* GFM-MWT.

4.4.3 Torsional modal analysis of the GFM-MWTs with different DVCs

This subsection examines how different DVC schemes affect the torsional modes of GFM-MWTs using the complex torque coefficients method. This approach simplifies the derivations of natural frequencies, damping ratios, and damped frequencies for these modes.

The torsional coefficients $W_s(s)$ and $W_d(s)$ for GFM-MWTs under three distinct DVC configurations are derived based on equations (4.21) - (4.23), and are illustrated in Fig. 4.13.

The analysis indicates that $|W_s(s)|$ is significantly smaller than $|k_s|$ within the frequency range critical to torsional dynamics (1-10 Hz) [64], suggesting that the natural frequency ω_{nm} of GFM-MWTs under different controls remains close to the natural frequency ω_{nt} of the turbine [73].

Once ω_{nm} is determined, $W_d(s)$ is used to compute the damping ratio ξ_m and the damped frequency ω_{dm} through (3.35). Fig. 4.13 shows that $W_d(s)$ is negative at ω_{nm} for all DVC types, indicating a negative damping impact on torsional dynamics. The primary contributors to this effect are $-K_{P\omega}$ for Type *a* and $-K_{T\omega}$ for Types *b* and *c*, as detailed in their respective control equations.

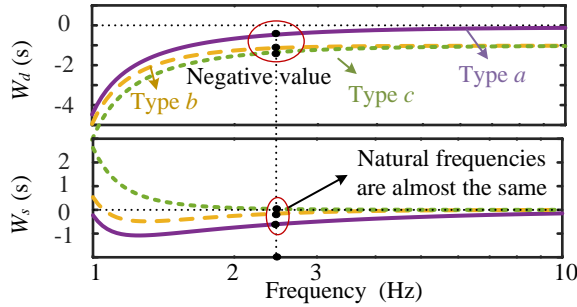


Figure 4.13: Torsional coefficients $W_s(s)$ and $W_d(s)$ for Type a , b , and c GFM-MWT configurations.

As outlined in (4.20), $K_{p\omega} < K_{T\omega}$ in the MPPT zone, leading to a less negative damping ratio ξ_m for Type a compared to Types b and c . Considering ω_{nm} is similar to ω_n and ξ_m is smaller than ξ , the damped frequency ω_{dm} remains relatively unchanged.

Using parameters from Table 3.1, the calculated values of ξ_m and ω_{dm} for Types a , b , and c are illustrated in Fig. 4.14. It is shown that ω_{dm} hovers around 2.5 Hz, and the order of damping ratios from highest to lowest is: Turbine, 2-mass drive train, Type a GFM-MWT, Type b GFM-MWT, and Type c GFM-MWT.

Further analysis on how both control and system parameters impact ξ_m and ω_{dm} of GFM-MWTs under different controls is detailed in Chapter. 4.4.4, aiming to provide comprehensive guidance for selecting the appropriate DVC strategy for the GFM-MWT under various conditions.

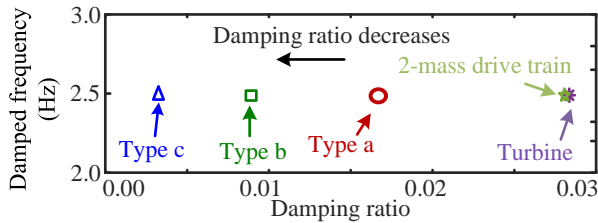


Figure 4.14: Damped frequency and damping ratio for the 2-mass drive train, turbine, and type a , b , and c GFM-MWTs

4.4.4 Analysis of influence factors

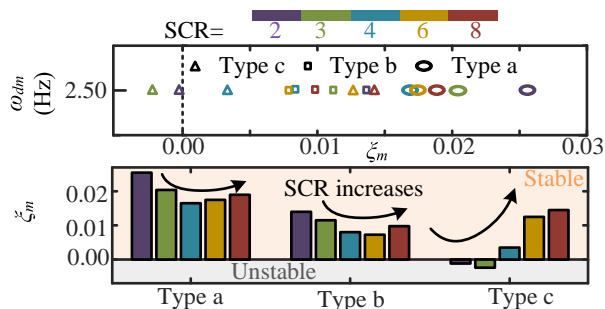


Figure 4.15: Damped frequency and damping ratio of type *a*, *b* and *c* GFM-MWTs under varying SCR

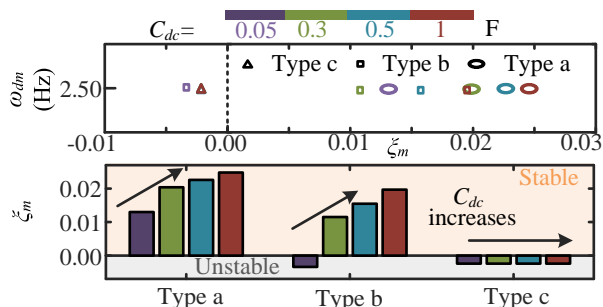


Figure 4.16: Damped frequency and damping ratio of type *a*, *b* and *c* GFM-MWTs under varying C_{dc} when SCR=3

Figure 4.15 illustrates the impact of varying SCR values on the damping ratio ζ_m across all DVC types for GFM-MWTs. As SCR increases, ζ_m initially decreases before increasing, indicating complex interactions between the grid impedance and control dynamics of GFM-MWT. Notably, for SCR values of 2 and 3, ζ_m for Type *c* GFM-MWT is negative, suggesting system instability under these conditions. Conversely, Type *a* consistently exhibits the highest damping ratios, suggesting robust stability.

Figure 4.16 shows that increasing the dc-link capacitor capacity, C_{dc} , enhances ζ_m for Types *a* and *b*, where the capacitor acts as an energy buffer enhancing system damping. In contrast, Type *c* experiences no significant change in ζ_m due to the additional feed-forward term P_o in its DVC scheme, which compensates for fluctuations.

Increasing the GFM control parameter H enhances ζ_m across all types, as shown in Fig. 4.17. Negative damping ratios are observed for Type *c* GFM-WT

at H values of 2 and 3, and for Type b at $H = 2$, indicating potential instability under these conditions. Type a remains positively damped, reinforcing its stability advantage.

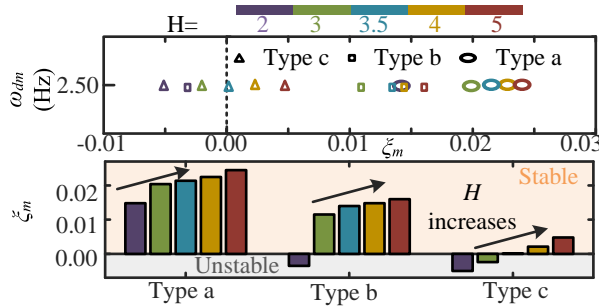


Figure 4.17: Damped frequency and damping ratio of type a , b and c GFM-MWTs under varying H when SCR=3

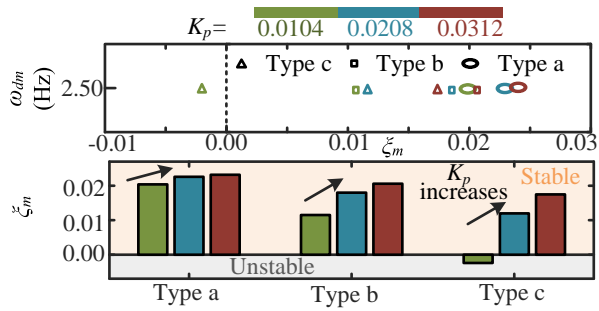


Figure 4.18: Damped frequency and damping ratio under varying K_p when SCR=3

An increase in the proportional gain K_p uniformly enhances ζ_m for all types, as depicted in Fig. 4.18. This enhancement suggests that higher proportional control contributes positively to system damping.

Operating at higher wind speeds (v_w) generally reduces ζ_m , as shown in Fig. 4.19. However, Type a GFM-MWT maintains the highest damping ratios across all wind speed settings, underscoring its superior performance in stabilizing torsional vibrations.

In summary, Type a consistently demonstrates the highest damping ratios under all evaluated conditions, indicating its efficacy in mitigating torsional vibrations compared to Types b and c .

4.4.5 Validation through Nonlinear Time-Domain Simulations

To validate the torsional vibration analysis of the GFM-MWT using different DVCs under the changes in θ_g , nonlinear time-domain simulations are con-

4.4. The impact of dc-link voltage control on torsional vibrations within GFM-MWT

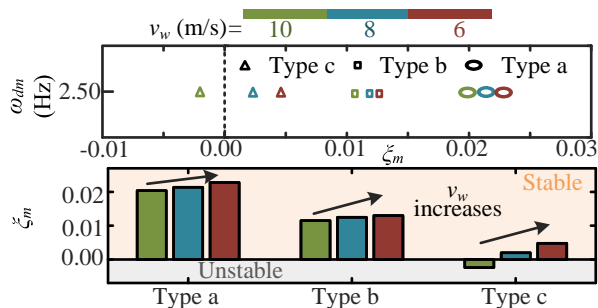


Figure 4.19: Damped frequency and damping ratio of type *a*, *b* and *c* GFM-MWTs under varying operating point v_w when SCR=3

ducted using MATLAB/Simulink and PLECS with the MSC models depicted in Fig. 4.10. Parameters from Table 3.1 are utilized.

Simulations measure the response of ω_r to a 2° step disturbance in θ_g . The results, illustrated in Fig. 4.20, compare the nonlinear time-domain response against the small-signal model predictions for three types of GFM-MWTs, with a maximum error of about $2.75e^{-4}$ p.u.

Figs. 4.15 - 4.19 further validates our theories, showing how different system and control parameters affect the torsional vibrations. This aligns with the sensitivity analysis presented in Section. 4.4.4.

Fig. 4.15 illustrates the variation of the damping ratio of torsional vibrations of ω_r with the change of SCR. As SCR increases, the damping ratio initially rises, then decreases, reaching a minimum at SCR = 4 for type *a* GFM-MWT before increasing again. This behavior is corroborated by the simulation results shown in Fig. 4.21 (a). For type *c* GFM-MWT, negative damping ratios are observed at SCR of 2 and 3, with the most unstable condition occurring at SCR = 3, as indicated by the blue solid line and red dashed line in Fig. 4.21 (c). The system stabilizes as SCR increases further, as seen in the green dotted and purple dash-dotted lines in Fig. 4.21 (b). Type *b* GFM-MWT displays the highest amplitude of torsional vibrations at SCR = 4, as shown by the green dotted line in Fig. 4.21 (c), confirming the observed trends in Fig. 4.15.

Regarding C_{dc} , increased values enhance damping for types *a* and *b* GFM-MWTs, reducing torsional vibration amplitudes, as shown in Fig. 4.21 (d) and (e). Type *c*, however, shows minimal impact due to its DVC design, which includes a feed-forward term from P_o , as depicted across the blue, red, yellow, and purple lines in Fig. 4.21 (f).

Fig. 4.17 shows that increasing the GFM control parameter H is expected to enhance the damping of torsional vibrations following grid phase disturbances. This expectation is confirmed by simulation results depicted in Fig. 4.21 (g) - (i). Notably, Type *c* GFM-MWT becomes unstable when H reaches 3, as shown by the blue solid line in Fig. 4.21 (i), which corroborates the insights discussed

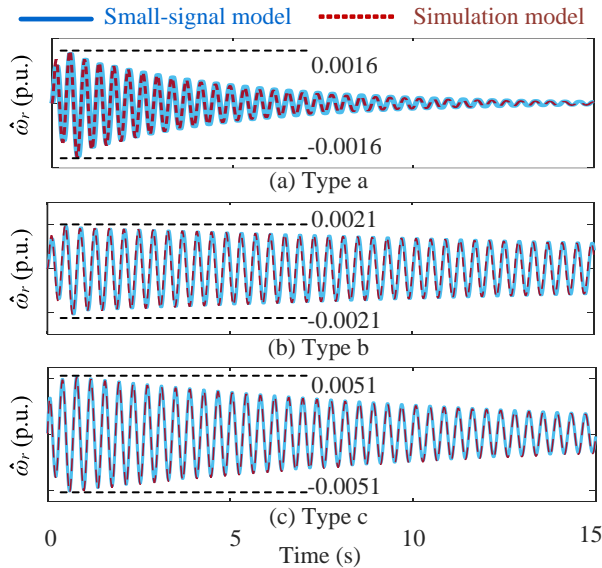


Figure 4.20: Comparison of nonlinear time-domain simulation results and small-signal models for disturbance response of ω_r with 2° step disturbance adding to θ_g under steady state. (a) Type *a* GFM-MWT. (b) Type *b* GFM-MWT. (c) Type *c* GFM-MWT.

in Section. 4.4.4.

Fig. 4.21 (j) - (l) indicate that an increase in the proportional gain K_p generally leads to reduced amplitudes of torsional vibrations across all types of systems.

As for the influence of v_w , higher wind speeds typically reduce damping, particularly for type *c*, which becomes unstable at $v_w = 10\text{m/s}$, shown in Fig. 4.21 (o). However, type *a* maintains the highest damping ratio under all operating conditions, reinforcing its stability benefits.

This validation confirms that DVC schemes critically affect the torsional dynamics of GFM-MWTs, especially under grid disturbances, with type *a* proving the most effective at mitigating negative damping effects. Additionally, excluding the DVC from the analysis could lead to different outcomes, especially under scenarios characterized by high wind speeds, low values of the inertia control parameter H , and low SCR.

4.5 Summary

This chapter explores the effects of different converter controls on the torsional dynamics of GFM-WTs, with a focus on the differential impacts of GFM-GWT and GFM-MWT configurations and the influence of DVC strategies within the

4.5. Summary

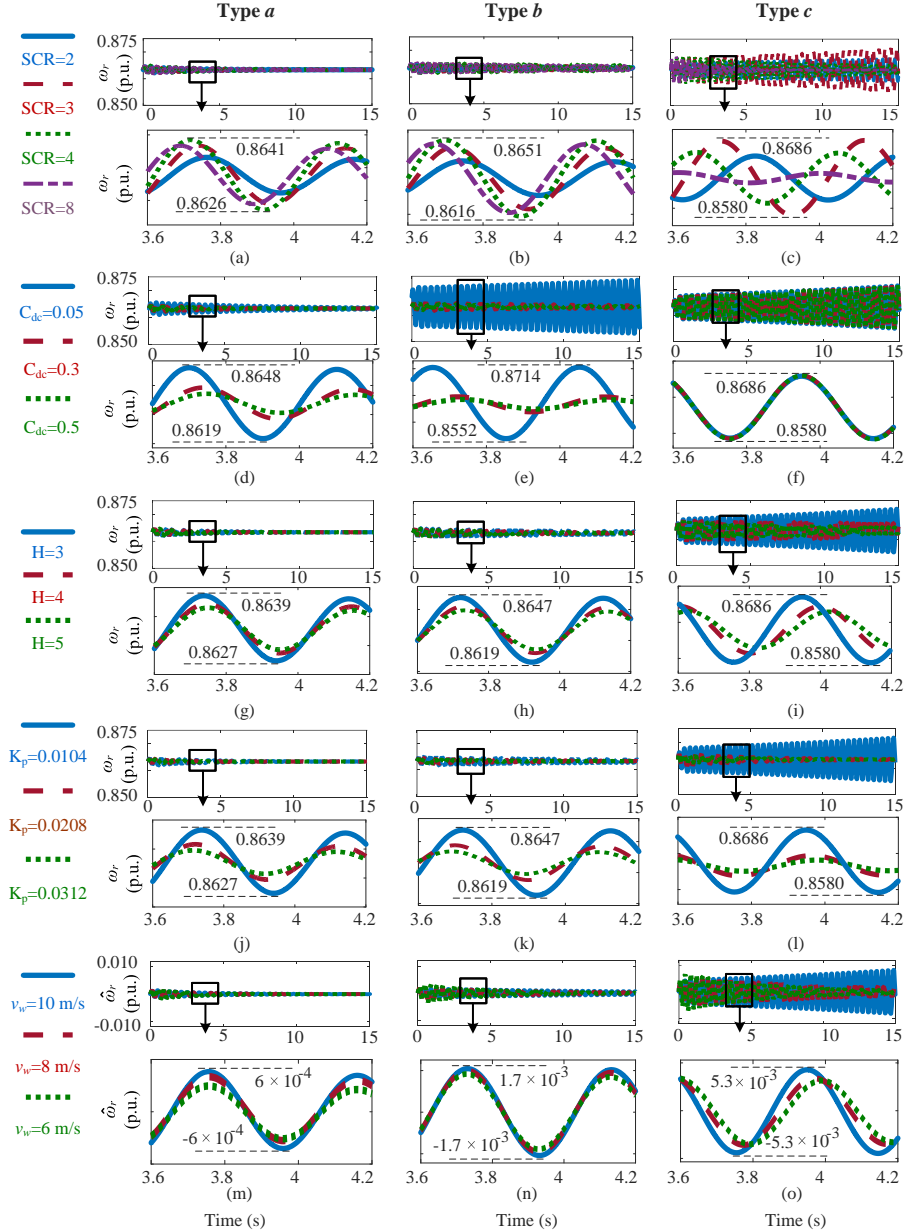


Figure 4.21: Disturbance response of ω_r for the type *a*, *b* and *c* GFM-WT with 2° step disturbance adding to θ_g under varied control and system parameters. (a)-(c) Changing SCR. (d)-(f) Changing C_{dc} . (g)-(i) Changing control parameter H . (j)-(l) Changing control parameter K_p . (m)-(o) Changing operating wind speed v_w .

MSC for the GFM-MWT. The key contributions are summarized as follows:

1. A detailed comparative analysis between GFM-GWT and GFM-MWT is conducted to illustrate their respective influences on torsional dynamics. This analysis utilizes reduced-order small-signal models alongside the complex torque coefficients method to elucidate the dynamic responses. It is found that the GFM-MWT control has an adverse impact on the damping ratio of the torsional mode of the GFM-WT, which is a consequence primarily driven by the DVC of MSC. In contrast, the GFM-GWT control enhances the damping ratio of the torsional mode.
2. A novel approach to sensitivity analysis is introduced through the use of a FNN-based PDA. This method provides a comprehensive assessment of how multiple, interdependent system parameters simultaneously affect torsional modes for both GFM-GWT and GFM-MWT configurations. More specifically, it is pointed out that the damped frequency of torsional modes for GFM-WT is dominated by mechanical design regardless of varying control parameters.
3. The chapter delves into a thorough comparative analysis of three commonly used DVC strategies implemented within the MSC of GFM-MWTs. It develops small-signal models for each control strategy, derives their respective torsional modes, and assesses their specific impacts. This analysis aims to inform targeted design recommendations that enhance torsional stability from a system-wide perspective. Importantly, it is established that type *a* DVC, which has no feedback loop from the GSC and the turbine, minimizes the adverse damping effect introduced by the GFM-MWT control, regardless of varying system parameters or operational states.

These insights extend the understanding of how converter control strategies influence the integration and performance of GFM-WTs in power systems in terms of electromechanical dynamics.

Chapter 5

Conclusion and future work

5.1 Conclusions

This Ph.D. thesis has systematically explored the small-signal stability analysis and control of GFM-WTs with an emphasis on understanding and improving their electromagnetic and electromechanical dynamics. Through a series of detailed investigations, such as analytical modeling and dynamic analysis, the research presented here contributes significantly to the field of integrating grid-forming control into Type IV wind turbines. The main findings and contributions of this thesis are summarized below:

- **Impedance modeling and electromagnetic dynamics analysis:** The thesis begins with an approach for impedance modeling of GFM-MPMSGs to study its electromagnetic dynamics. By developing the dc impedance models of MSC and PMSG, the work finds out that the impact of the MSC and PMSG on the ac electromagnetic dynamics of the GFM-MPMSG is limited, thereby simplifying the small-signal modeling and stability analysis of the GFM-MPMSG system.
- **Torsional Vibration Analysis:** A significant portion of the research focused on analyzing the torsional dynamics of GFM-MWTs. The reduced-order small-signal model of the GFM-MWT is developed to reveal the direct link between converter control strategies and mechanical dynamics within wind turbines. Furthermore, the introduction of the complex torque coefficients method enhances the analytical depth into torsional vibrations, deriving the expressions for damping ratio, natural frequency, and damped frequency for the torsional modes of the GFM-MWT. Through analyzing the expressions, this analysis highlighted the critical nature of GFM-MWT configuration in introducing adverse impacts on the damping ratio.

- **Impacts of Control Strategies:** Comparative analyses of the GFM-MWT and GFM-GWT configurations are implemented through the complex torque coefficients method-based torsional modal analysis. It is shown that the GFM-GWT control increases the damping ratio of the torsional mode while the GFM-MWT control introduces a negative impact on it, which is driven by the DVC scheme within the MSC of the GFM-MWT. Thereafter, the study expanded into a detailed examination of different DVC strategies within the MSC for the GFM-MWT, illustrating their unique effects on torsional modes, especially for the damping ratio. It is clear that type *a* DVC, which has no feedback loop from the GSC and the turbine, minimizes this adverse damping effect regardless of varying system parameters or operational states.
- **Nonlinear Sensitivity Analysis:** Employing the FNN-based PDA, the thesis offers a holistic evaluation of the influence of all control and system parameters on damping ratio and damped frequency of torsional modes for the GFM-MWT and GFM-GWT. More specifically, it is pointed out that the damped frequency of torsional modes for GFM-WT is dominated by mechanical design regardless of varying control parameters regardless of the specific configuration.

In conclusion, this thesis addressed the small-signal stability of GFM-WTs by introducing the complex torque coefficients method and the FNN-based PDA, providing a deeper understanding of the interactions between electrical and mechanical dynamics under different converter control strategies. The insights gained from this research are expected to guide the future development of GFM-WTs, particularly in enhancing their integration into the modern power grid.

5.2 Future Work

To expand upon the findings and insights gained from this Ph.D. project, several routes for future research have been identified to deepen our understanding of the dynamics of the grid-forming wind turbines and their integration into power systems. Future investigations could include:

- The modeling of mechanical components in this thesis primarily utilizes a 2-mass drive train model to represent the dynamics of the turbine. Future work could explore additional torsional modes introduced by more complex models, including the blade and tower dynamics, which might influence the overall system stability and performance.
- While this study focused on small-signal stability, the response of GFM-WTs to large disturbances such as grid faults remains critical. Inves-

tigating the behavior of current-limiting controls and dc-link voltage protections during such events will be crucial. Additionally, studying the recovery processes post low-voltage faults could provide insights into enhancing system resilience.

- This thesis has considered only symmetrical three-phase grid scenarios. Future research should extend the analysis to asymmetrical grid conditions, such as single-phase faults. This involves studying both positive and negative sequence components to fully understand the impact on GFM-WTs under unbalanced grid conditions.
- Analyzing the stability of multiple wind turbines operating in parallel, such as in a large wind farm, is another vital area of study. Understanding the collective dynamics of over 100 turbines simultaneously could lead to better management and optimization of wind resources at the farm scale.

References

- [1] "Entso-e transparency platform," Tech. Rep., 2024, accessed: Date Accessed.
- [2] E. Commission, "A clean planet for all," Tech. Rep., 2018.
- [3] A. Avazov, "Ac connection of wind farms to transmission system: from grid-following to grid-forming," Ph.D. dissertation, Centrale Lille Institut; Katholieke universiteit te Leuven, 2022.
- [4] Vestas, "Wind & grid-forming – challenges & opportunities," in *22nd Wind Integration Workshop*, 2023.
- [5] L. Huang, "Modeling, stability analysis, and control of wind generation system connected to weak grid," Ph.D. dissertation, Aalborg Universitetsforlag, 2023.
- [6] Y. Liao, "Impedance modeling and stability analysis of grid-interactive converters," Ph.D. dissertation, Aalborg Universitetsforlag, 2020.
- [7] D. Aragon, E. Unamuno, S. Ceballos, and J. Barrena, "Comparative small-signal evaluation of advanced grid-forming control techniques," *Electric Power Systems Research*, vol. 211, p. 108154, 2022.
- [8] X. Xiong, C. Wu, B. Hu, D. Pan, and F. Blaabjerg, "Transient damping method for improving the synchronization stability of virtual synchronous generators," *IEEE Transactions on Power Electronics*, vol. 36, no. 7, pp. 7820–7831, 2021.
- [9] S. Liu, H. Wu, X. Wang, T. Bosma, J. van der Burgt, G. Sauba, and R. Singh, "Active damping of power control for grid-forming inverters in lc resonant grids," in *2022 IEEE Energy Conversion Congress and Exposition (ECCE)*, 2022, pp. 1–6.
- [10] H. Wu and X. Wang, "Small-signal modeling and controller parameters tuning of grid-forming vscs with adaptive virtual impedance-based current limitation," *IEEE Transactions on Power Electronics*, vol. 37, no. 6, pp. 7185–7199, 2022.

References

- [11] J. Matevosyan, B. Badrzadeh, T. Prevost, E. Quitmann, D. Ramasubramanian, H. Urdal, S. Achilles, J. MacDowell, S. H. Huang, V. Vital, J. O'Sullivan, and R. Quint, "Grid-forming inverters: Are they the key for high renewable penetration?" *IEEE Power and Energy Magazine*, vol. 17, no. 6, pp. 89–98, 2019.
- [12] A. Avazov, F. Colas, J. Beerten, and X. Guillaud, "Damping of torsional vibrations in a type-iv wind turbine interfaced to a grid-forming converter," in *2021 IEEE Madrid PowerTech*, 2021, pp. 1–6.
- [13] ENTSO-E, "Research, development & innovation roadmap 2020–2030," Tech. Rep.
- [14] L. Huang, C. Wu, D. Zhou, L. Chen, D. Pagnani, and F. Blaabjerg, "Challenges and potential solutions of grid-forming converters applied to wind power generation system—an overview," *Frontiers in Energy Research*, vol. 11, p. 1040781, 2023.
- [15] T.-T. Nguyen, T. Vu, S. Paudyal, F. Blaabjerg, and T. L. Vu, "Grid-forming inverter-based wind turbine generators: Comprehensive review, comparative analysis, and recommendations," *arXiv preprint arXiv:2203.02105*, 2022.
- [16] Y. Li, Z. Xu, and K. P. Wong, "Advanced control strategies of pmsg-based wind turbines for system inertia support," *IEEE Transactions on Power Systems*, vol. 32, no. 4, pp. 3027–3037, 2017.
- [17] S. Sang, C. Zhang, X. Cai, M. Molinas, J. Zhang, and F. Rao, "Control of a type-iv wind turbine with the capability of robust grid-synchronization and inertial response for weak grid stable operation," *IEEE Access*, vol. 7, pp. 58 553–58 569, 2019.
- [18] H. Geng, D. Xu, B. Wu, and G. Yang, "Comparison of oscillation damping capability in three power control strategies for pmsg-based wecs," *Wind Energy*, vol. 14, no. 3, pp. 389–406, 2011. [Online]. Available: <https://onlinelibrary.wiley.com/doi/abs/10.1002/we.428>
- [19] D. Duckwitz, M. Shan, and B. Fischer, "Synchronous inertia control for wind turbines," in *13th wind integration workshop*, 2014.
- [20] J. Kim, S. H. Lee, and J.-W. Park, "Inertia-free stand-alone microgrid—part ii: Inertia control for stabilizing dc-link capacitor voltage of pmsg wind turbine system," *IEEE Transactions on Industry Applications*, vol. 54, no. 5, pp. 4060–4068, 2018.
- [21] L. P. Kunjumammed, B. C. Pal, R. Gupta, and K. J. Dyke, "Stability analysis of a pmsg-based large offshore wind farm connected to a vsc-hvdc," *IEEE Transactions on Energy Conversion*, vol. 32, no. 3, pp. 1166–1176, 2017.
- [22] J. Liu, F. Zhou, C. Zhao, and Z. Wang, "Mechanism analysis and suppression strategy research on permanent magnet synchronous generator wind turbine torsional vibration," *ISA Transactions*, vol. 92, pp. 118–133, 2019.
- [23] W. Liu, X. Xie, H. Liu, and J. He, "Mechanism and characteristic analyses of subsynchronous oscillations caused by the interactions between direct-drive wind turbines and weak ac power systems," *The Journal of Engineering*, vol. 2017, no. 13, pp. 1651–1656, 2017.
- [24] S. I. Nanou and S. A. Papathanassiou, "Grid code compatibility of vsc-hvdc connected offshore wind turbines employing power synchronization control," *IEEE Transactions on Power Systems*, vol. 31, no. 6, pp. 5042–5050, 2016.

References

- [25] N. Hatziaargyriou, J. Milanovic, C. Rahmann, V. Ajjarapu, C. Canizares, I. Erlich, D. Hill, I. Hiskens, I. Kamwa, B. Pal, P. Pourbeik, J. Sanchez-Gasca, A. Stankovic, T. Van Cutsem, V. Vittal, and C. Vournas, "Definition and classification of power system stability – revisited extended," *IEEE Transactions on Power Systems*, vol. 36, no. 4, pp. 3271–3281, 2021.
- [26] K. Ma, D. Zhou, and F. Blaabjerg, "Evaluation and design tools for the reliability of wind power converter system," *Journal of power electronics*, vol. 15, no. 5, pp. 1149–1157, 2015.
- [27] H. Huang, C. Mao, J. Lu, and D. Wang, "Small-signal modelling and analysis of wind turbine with direct drive permanent magnet synchronous generator connected to power grid," *IET Renewable Power Generation*, vol. 6, no. 1, pp. 48–58, 2012.
- [28] H. Liu, X. Xie, J. He, T. Xu, Z. Yu, C. Wang, and C. Zhang, "Subsynchronous interaction between direct-drive pmsg based wind farms and weak ac networks," *IEEE Transactions on Power Systems*, vol. 32, no. 6, pp. 4708–4720, 2017.
- [29] K. M. Alawasa, Y. A.-R. I. Mohamed, and W. Xu, "Modeling, analysis, and suppression of the impact of full-scale wind-power converters on subsynchronous damping," *IEEE Systems Journal*, vol. 7, no. 4, pp. 700–712, 2013.
- [30] J. Sun, "Impedance-based stability criterion for grid-connected inverters," *IEEE Transactions on Power Electronics*, vol. 26, no. 11, pp. 3075–3078, 2011.
- [31] H. Liu and X. Xie, "Comparative studies on the impedance models of vsc-based renewable generators for ssi stability analysis," *IEEE Transactions on Energy Conversion*, vol. 34, no. 3, pp. 1442–1453, 2019.
- [32] E. Ebrahimzadeh, F. Blaabjerg, X. Wang, and C. L. Bak, "Harmonic stability and resonance analysis in large pmsg-based wind power plants," *IEEE Transactions on Sustainable Energy*, vol. 9, no. 1, pp. 12–23, 2018.
- [33] H. Liu and J. Sun, "Voltage stability and control of offshore wind farms with ac collection and hvdc transmission," *IEEE Journal of Emerging and Selected Topics in Power Electronics*, vol. 2, no. 4, pp. 1181–1189, 2014.
- [34] C. Zhang, X. Cai, M. Molinas, and A. Rygg, "On the impedance modeling and equivalence of ac/dc-side stability analysis of a grid-tied type-iv wind turbine system," *IEEE Transactions on Energy Conversion*, vol. 34, no. 2, pp. 1000–1009, 2019.
- [35] L. Huang, C. Wu, D. Zhou, and F. Blaabjerg, "Comparison of dc-link voltage control schemes on grid-side and machine-side for type-4 wind generation system under weak grid," in *IECON 2021 – 47th Annual Conference of the IEEE Industrial Electronics Society*, 2021, pp. 1–6.
- [36] Y. Xu, H. Nian, and L. Chen, "Small-signal modeling and analysis of dc-link dynamics in type-iv wind turbine system," *IEEE Transactions on Industrial Electronics*, vol. 68, no. 2, pp. 1423–1433, 2021.
- [37] W. Yan, L. Cheng, S. Yan, W. Gao, and D. W. Gao, "Enabling and evaluation of inertial control for pmsg-wtg using synchronverter with multiple virtual rotating masses in microgrid," *IEEE Transactions on Sustainable Energy*, vol. 11, no. 2, pp. 1078–1088, 2020.

References

- [38] A. Hansen and G. Michalke, "Modelling and control of variable-speed multi-pole permanent magnet synchronous generator wind turbine," *Wind Energy*, vol. 11, no. 5, pp. 537–554, 2008.
- [39] L. Chen, X. Du, B. Hu, and F. Blaabjerg, "Drivetrain oscillation analysis of grid forming type-iv wind turbine," *IEEE Transactions on Energy Conversion*, vol. 37, no. 4, pp. 2321–2337, 2022.
- [40] J. Kim, S. H. Lee, and J.-W. Park, "Inertia-free stand-alone microgrid—part ii: Inertia control for stabilizing dc-link capacitor voltage of pmsg wind turbine system," *IEEE Transactions on Industry Applications*, vol. 54, no. 5, pp. 4060–4068, 2018.
- [41] S. S. Heidary Yazdi, J. Milimonfared, S. H. Fathi, K. Rouzbehi, and E. Rakhshani, "Analytical modeling and inertia estimation of vsg-controlled type 4 wtgs: Power system frequency response investigation," *International Journal of Electrical Power Energy Systems*, vol. 107, pp. 446–461, 2019.
- [42] Z. Zhou, X. Wang, and Y. Sun, "Aggregation of wind turbine grid-side inverters by voltage angle and cable resonance compensation," in *2021 IEEE Energy Conversion Congress and Exposition (ECCE)*, 2021, pp. 403–410.
- [43] S. Liu, H. Wu, L. Zhao, X. Wang, T. Bosma, J. Van Der Burgt, and G. Sauba, "Impact of machine-side converter dynamics on ac impedance of grid-forming pmsg wind turbines," in *2023 IEEE Applied Power Electronics Conference and Exposition (APEC)*, 2023, pp. 1339–1344.
- [44] D. Duckwitz, "Power system inertia: Derivation of requirements and comparison of inertia emulation methods for converter-based power plants," Ph.D. dissertation, Universitätsbibliothek Kassel, 2019.
- [45] S. S. H. Yazdi, Y. Shokri-Kalandaragh, and M. Bagheri, "Power system stability improvement considering drive train oscillations of virtual synchronous generator-regulated type-4 wind turbines," *IET Renewable Power Generation*, vol. 17, no. 3, pp. 579–603, 2023.
- [46] A. Avazov, F. Colas, J. Beerten, and X. Guillaud, "Application of input shaping method to vibrations damping in a type-iv wind turbine interfaced with a grid-forming converter," *Electric Power Systems Research*, vol. 210, p. 108083, 2022.
- [47] Z. Zhang, X. Zhao, L. Fu, and M. Edrah, "Stability and dynamic analysis of the pmsg-based wecs with torsional oscillation and power oscillation damping capabilities," *IEEE Transactions on Sustainable Energy*, vol. 13, no. 4, pp. 2196–2210, 2022.
- [48] S. Liu, H. Wu, X. Wang, and T. Bosma, "Impact of dc-link voltage control on torsional vibrations in grid-forming pmsg wind turbines," 2023.
- [49] S. D'Arco, J. A. Suul, and O. B. Fosso, "Small-signal modelling and parametric sensitivity of a virtual synchronous machine," in *2014 Power Systems Computation Conference*, 2014, pp. 1–9.
- [50] S. Liu, H. Wu, X. Wang, A. Avazov, X. Guillaud, T. Bosma, and G. Sauba, "Torsional vibration analysis of grid-forming pmsg wind turbine," 2023.

References

- [51] M. Cao, N. F. Alkayem, L. Pan, D. Novák, and J. Rosa, "Advanced methods in neural networks-based sensitivity analysis with their applications in civil engineering," *Artificial neural networks: models and applications, Rijeka, Croatia, IntechOpen*, pp. 335–353, 2016.
- [52] S. Liu, R. G. Cirstea, H. Wu, X. Wang, and T. Bosma, "Comparative analysis of the influence of converters control strategies on torsional dynamics in grid-forming wind turbines," 2023.
- [53] S. I. Nanou and S. A. Papathanassiou, "Grid code compatibility of vsc-hvdc connected offshore wind turbines employing power synchronization control," *IEEE Transactions on Power Systems*, vol. 31, no. 6, pp. 5042–5050, 2016.
- [54] P. Brogan, T. Knueppel, D. Elliott, and N. Goldenbaum, "Experience of grid forming power converter control," in *17th Wind Integration Workshop, Stockholm, Sweden*, 2018.
- [55] A. K. Singh, R. Krishnam, and Y. Sood, "Modeling and control of grid connected variable speed pmsg based wind energy system," in *Proceedings of the Conference on Advances in Communication and Control Systems (CAC2S 2013)*. Atlantis Press, 2013/04, pp. 134–139.
- [56] J. Morren, J. Pierik, and S. W. de Haan, "Inertial response of variable speed wind turbines," *Electric Power Systems Research*, vol. 76, no. 11, pp. 980–987, 2006. [Online]. Available: <https://www.sciencedirect.com/science/article/pii/S0378779605002713>
- [57] L. Zhang, L. Harnefors, and H.-P. Nee, "Power-synchronization control of grid-connected voltage-source converters," *IEEE Transactions on Power Systems*, vol. 25, no. 2, pp. 809–820, 2010.
- [58] T. Suntio, T. Messo, and J. Puukko, *Power electronic converters: dynamics and control in conventional and renewable energy applications*. John Wiley & Sons, 2017.
- [59] D. Pan, X. Wang, F. Liu, and R. Shi, "Transient stability of voltage-source converters with grid-forming control: A design-oriented study," *IEEE Journal of Emerging and Selected Topics in Power Electronics*, vol. 8, no. 2, pp. 1019–1033, 2020.
- [60] L. Zhang, "Modeling and control of vsc-hvdc links connected to weak ac systems," Ph.D. dissertation, KTH, 2010.
- [61] S. Liu, H. Wu, X. Wang, and T. Bosma, "Stability analysis and active damping design for grid-forming converters in lc resonant grids," 2023.
- [62] F. Zhou, "Drive-train torsional vibration suppression of large scale pmsg-based wecs," *Protection and Control of Modern Power Systems*, vol. 7, no. 1, pp. 1–13, 2022.
- [63] F. K. Moghadam and T. K. Vrana, "Wind power plant grid-forming control and influences on the power train and power system oscillations," in *11th International Conference on Renewable Power Generation-Meeting net zero carbon (RPG 2022)*, vol. 2022. IET, 2022, pp. 146–154.
- [64] W. K. Wilson, *Practical Solution of Torsional Vibration Problems*. Chapman amp; Hall, London., 1942, vol. 1, no. 731.
- [65] F. Zhou, J. Liu *et al.*, "Pitch controller design of wind turbine based on nonlinear pi/pd control," *Shock and Vibration*, vol. 2018, 2018.

References

- [66] C. B. Mayer, "Torsional vibration problems and analyses of cement industry drives," *IEEE Transactions on Industry Applications*, vol. IA-17, no. 1, pp. 81–89, 1981.
- [67] Z. Zhang, B. Chen, and S. R. Nielsen, "Coupled-mode flutter of wind turbines and its suppression using torsional viscous damper," *Procedia Engineering*, vol. 199, pp. 3254–3259, 2017, x International Conference on Structural Dynamics, EUROODYN 2017.
- [68] P. Kundur, *Power System Stability and Control*. McGraw-Hill, 1994.
- [69] T. Qu, Y. Li, X. Yuan, and Z. Du, "Damping torque coefficient analysis of pmsg-based wt with vsg control considering wind turbine dynamics," *IET Generation, Transmission & Distribution*, vol. 17, no. 2, pp. 367–379, 2023.
- [70] R. Pena, R. Cardenas, R. Blasco, G. Asher, and J. Clare, "A cage induction generator using back to back pwm converters for variable speed grid connected wind energy system," in *IECON'01. 27th Annual Conference of the IEEE Industrial Electronics Society (Cat. No.37243)*, vol. 2, 2001, pp. 1376–1381 vol.2.
- [71] L. Zhao, Z. Jin, and X. Wang, "Analysis and damping of low-frequency oscillation for dc-link voltage-synchronized vsocs," *IEEE Transactions on Power Electronics*, vol. 38, no. 7, pp. 8177–8189, 2023.
- [72] Y. Dimopoulos, P. Bourret, and S. Lek, "Use of some sensitivity criteria for choosing networks with good generalization ability," *Neural Processing Letters*, vol. 2, pp. 1–4, 1995.
- [73] A. Tabesh and R. Iravani, "On the application of the complex torque coefficients method to the analysis of torsional dynamics," *IEEE Transactions on Energy Conversion*, vol. 20, no. 2, pp. 268–275, 2005.

